FIRST-PRINCIPLES STUDY OF

PIEZOELECTRIC (Ba,Ca)TiO$_3$-Ba(Ti,Zr)O$_3$ SOLID SOLUTIONS

Thesis presented to obtain the academic grade of

Doctor in Sciences
Université de Liège

Doctor in Physics-Chemistry of Condensed Matter
Université de Bordeaux

by

Danila AMOROSO

Jury committee:

Prof. Philippe GHOSEZ (Supervisor)	Université de Liège
Dr. Antoine VILLESUZANNE (Supervisor)	Université de Bordeaux
Prof. Javier JUNQUERA (President)	Universidad de Cantabria
Dr. Eric BOUSQUET (Secretary)	Université de Liège
Dr. Andrés CANO	Institut NEEL
Dr. Mario MAGLIONE	Université de Bordeaux
Prof. Jens KREISEL	University of Luxembourg
Dr. Gregory GENESTE	Commiss. énergie atomique et énergies alternatives

26th September 2018

First-principles study of
piezoelectric (Ba,Ca)TiO₃-Ba(Ti,Zr)O₃ solid solutions

Abstract. High-performance piezoelectrics are key components of various smart devices and, recently, it has been discovered that $(Ba,Ca)(Ti,Zr)O_3$ (BCTZ) solid solutions show appealing electromechanical properties. Nevertheless, the microscopic mechanisms leading to such features are still unclear and theoretical investigations of BCTZ remain very limited. Accordingly, this thesis analyzes the properties of various compositions of $(Ba,Ca)TiO_3$-$Ba(Ti,Zr)O_3$ solid solutions by means of first-principles calculations, with a focus on the lattice dynamics and the competition between different ferroelectric phases. We first analyze the four parent compounds $BaTiO_3$, $CaTiO_3$, $BaZrO_3$ and $CaZrO_3$ in order to compare their properties and their different tendency towards ferroelectricity. Then, the core of our study is a systematic characterization of the binary systems $(Ba,Ca)TiO_3$ and $Ba(Ti,Zr)O_3$ within both the virtual crystal approximation (VCA) and direct supercell calculations. When going from $BaTiO_3$ to $CaTiO_3$ in $(Ba,Ca)TiO_3$, the main feature is a gradual transformation from B-type to A-type ferroelectricity due to steric effects that largely determine the behavior of the system. In particular, for low Ca-concentration we found out an overall weakened B-driven ferroelectricity that produces the vanishing of the energy barrier between different polar states and results in a quasi-isotropic polarization. A sizable enhancement of the piezoelectric response results from these features. When going from $BaTiO_3$ to $BaZrO_3$ in $Ba(Ti,Zr)O_3$, in contrast, the behavior is dominated by cooperative Zr-Ti motions and the local electrostatics. In particular, low Zr-concentration produces the further stabilization of the $R3m$-phase. Then, the system shows the tendency to globally reduce the polar distortion with increasing Zr-concentration. Nevertheless, ferroelectricity can be locally preserved in Ti-rich regions. We also found out an unexpected polar activation of Zr as a function of specific atomic ordering explained via a basic electrostatic model based on $BaZrO_3/mBaTiO_3$ superlattice. A microscopic factor behind the enhanced piezoelectric response in BCTZ, at low concentration of Ca and Zr, can thus be the interplay between weakened Ti-driven and emerging Ca-driven ferroelectricity, which produces minimal anisotropy for the polarization. In addition, our comparative study reveals that the specific microscopic physics of these solid solutions sets severe limits to the applicability of the virtual crystal approximation (VCA) for these systems.

Keywords: lead-free compounds, piezoelectricity, ferroelectricity, lattice dynamics, ab-initio calculations

Étude ab-initio de
solutions solides piézoélectriques (Ba,Ca)TiO$_3$-Ba(Ti,Zr)O$_3$

Résumé. Les piézoélectriques à haute performance sont des composants clés pour les dispositifs agiles. Il a été démontré récemment que les solutions solides (Ba,Ca)(Ti,Zr)O$_3$ (BCTZ) présentent des propriétés électromécaniques prometteuses. Cependant, les mécanismes microscopiques conduisant à de telles caractéristiques restent à éclaircir, et les investigations théoriques de BCTZ demeurent trés limitées à ce jour. En conséquence, cette thése propose d'étudier les propriétés de différentes compositions de solutions solides (Ba,Ca)TiO$_3$-Ba(Ti,Zr)O$_3$ au moyen de calculs de premiers principes, en mettant l'accent sur la dynamique du réseau et sur la compétition entre différentes phases ferroélectriques . Nous nous intéressons d'abord aux quatre composés parents BaTiO$_3$, CaTiO$_3$, BaZrO$_3$ et CaZrO$_3$, afin de comparer leurs propriétés et leurs différentes tendances à la ferroélectricité. Ensuite, le cœur de notre étude est une caractérisation systématique des systèmes binaires (Ba,Ca)TiO$_3$ et Ba(Ti,Zr)O$_3$ en utilisant à la fois l'approximation du cristal virtuel (VCA) et des calculs directs sur supercellules. Lorsqu'on passe continument de BaTiO$_3$ à CaTiO$_3$ dans (Ba,Ca)TiO$_3$, la caractéristique principale est une transformation progressive de la ferroélectricité de type B en type A en raison d'effets stériques, lesquels déterminent en grande partie le comportement du système. En particulier, pour les petites concentrations en calcium, nous avons mis en évidence que la ferroélectricité guidée par le site B est globalement affaiblie, conduisant à la disparition de la barrière d'énergie entre différents états polaires et à une polarisation quasi-isotrope. Une amélioration considérable de la réponse piézoélectrique résulte de ces caractéristiques. En passant de BaTiO$_3$ à BaZrO$_3$ dans Ba(Ti,Zr)O$_3$, en revanche, le comportement est dominé par les mouvements coopératifs Zr-Ti et l'électrostatique locale. En particulier, la phase $R3m$ est stabilisée significativement pour les faibles concentrations en zirconium. Sous l'effet d'une augmentation de la concentration en zirconium, le syst̀me montre une tendance à la réduction de la distorsion polaire; néanmoins, la ferroélectricité peut être préservée localement dans les régions riches en titane. Grâce à un modèle électrostatique basé sur un super-réseau BaZrO$_3$/mBaTiO$_3$, nous avons également découvert un'activation polaire inattendue pour Zr, en fonction d'un ordre atomique spécifique. Un facteur microscopique expliquant la réponse piézoélectrique exaltée dans BCTZ, pour de faibles concentrations en Ca et Zr, peut donc résider dans l'interaction entre la ferroélectricité affaiblie induite par Ti et la ferroélectricité émergente induite par Ca, interaction produisant une anisotropie minimale pour la polarisation. En outre, notre étude comparative révèle que la physique microscopique spécifique de ces solutions solides limite sévèrement l'applicabilité de l'approximation du cristal virtuel (VCA) à ces systèmes.

Mots-clés: composés sans plomb, piézoélectricité, ferroélectricité, dynamique du réseau, calcul ab-initio

Acknowledgements

"Dum loquimur fugerit invida
aetas: carpe diem, quam minimum credula postero."
(Horatius, *Odi*, I, 11, 7-8)

Thinking about this period of my life, called "PhD", that famous poetic verse by the Roman poet Horatius suddenly has jumped to my mind, thus giving me causes of reflection. These three years, in fact, have passed so fast, that it still seems yesterday I was leaving, for the first time, my beloved family and region, Abruzzo, towards a totally new and unknown experience. The only, vague awareness I had was strictly related to the study-work field with the certainity that I was leaving to learn and try to lay the foundations for a career. Actually, it was totally unexpected to me that, beyond the professional growth, the greatest realization has been the personal growth, accompanied by a "disillusioned confidence" in the future.

In line with Horatius' words, I have started, step-by-step, to realize the time fugacity, and so to appreciate and enjoy the more various moments of life. Nevertheless, differently from what he then says, I have also started to be confident in the future because all of today's achievements were exactly the unknown future of yesterday.

However, all this would not have happened, if I had not met on this path or if they had not been there to support me, some reference persons. Therefore, I just want to truly say "*thank you* Sophia, Véronique, Zeila, Matthieu, Angela, Chiara, Domenico, Giulia, Simone, Silvia".

Then, I want to thank very much Philippe, for his continuous support and trust in me, allowing me to never give up. And I also thank Andres for reminding any time the importance of not underestimating even small details, eventually leading me to new interesting insights and discussions. Besides, I want to warmly thank all my colleagues "of the corridor", in particular, Eric, Sébastien, Alain, Alex, Marcus, and Fabio, not only for the technical and logistic help, but, above all, for having endured me despite my continuous critical speaking.

Then, I would like to say an extended thanks to the people of the "ferroelectric community" I have met in various conferences and schools, and with whom, beyond interesting scientific discussions, I have also spent nice and funny time. A special thanks to Mael and Constance for their availability to answer any question of mine at any time, and to Hania for her kindness.

Finally, I would like to share the satisfaction of this specific PhD achievement with the other "EJD-FunMat" PhD students, Francesco, Bruno, Catarina, Cong, Prya, Philip, Kenny, Sara, Yannick, Raphaël, Guillaume, Getnet and Mirasbek, as we have all faced tough and peculiar challenges.

Contents

Introduction

Piezoelectric devices have successfully relied on lead zirconate titanate (PZT) materials for several decades. Since 2003, the European Union has restricted the use of certain hazardous substances [40], such as Pb, which has driven the search for alternative lead-free piezoelectric compounds. In this respect, $BaTiO_3$-based solid solutions appear as interesting candidates, whose potential for piezoelectric applications has been known since the sixties [26, 31, 160]. Among possible combinations, the partial homovalent substitution of Ba by Ca and Ti by Zr at the A- and B- sites of $BaTiO_3$ ($Ba_{1-x}Ca_xTi_{1-y}Zr_yO_3$ hereafter BCTZ) is of special interest. In their seminal paper, Liu and Ren [44] reported a high piezoelectric coefficient of 620 pC/N for the ceramic system $(Ba_{0.7}Ca_{0.3})TiO_3$-$Ba(Ti_{0.8}Zr_{0.2})O_3$. This has been ascribed to the presence of a special point in the phase diagram in which the tetragonal and rhombohedral ferroelectric phases meet the paraelectric cubic one. Subsequently, Keeble *et al.* [51] revisited this phase diagram and observed an intermediate ferroelectric orthorhombic phase that also meets the three previous ones.

As in the case of Pb-based systems, the achievement of high piezoelectric response in BCTZ is believed to be linked to the existence of a so-called phase convergence region, in which the lack of energy barriers between different ferroelectric states makes the landscape isotropic and the polarization free to rotate [52]. However, no theoretical confirmation of this picture has been provided yet for this system. In fact, although a large number of experimental studies have been reported [44, 51, 106, 161], the number of theoretical investigations of BCTZ compounds remain comparatively very limited and, to the best of our knowledge, no comprehensive study based on direct Density Functional Theory (DFT) has been carried out so far.

In order to fill in this gap, here we report a systematic first-principles DFT study of $(Ba,Ca)(Ti,Zr)O_3$-type compounds with the intent to clarify the evolution with composition of their ferroelectric, piezoelectric and related properties. We proceed step-by-step. Thus, we first address carefully the four parent compounds. Then, starting from $BaTiO_3$, we investigate separately the evolution of the properties in $(Ba,Ca)TiO_3$ and $Ba(Ti,Zr)O_3$ solid solutions in order to disentangle the role of individual atomic substitutions at the A- and B-sites. We use both the Virtual Crystal Approximation (VCA) and explicit ordered supercells of different compositions. In each case, starting from the reference high-symmetry paraelectric phase, we identify and characterize the existing phonon instabilities. Then, comparing the energy of various possible distorted phases obtained from the condensation of unstable modes, we search and characterize the structural ground state. All along this work, a special emphasis is put on the analysis of the real-space interatomic force constants in order to rationalize the evolution of the properties with composition. Through such quantitative analysis and comparisons of properties between the parent compounds and their related solid solutions, our work reveals the distinct underlying microscopic mechanisms activated by A- and B-sites atomic substitutions. At the same time, it points out and explains strong limitations of the VCA approach for the

(Ba,Ca)TiO$_3$ and Ba(Ti,Zr)O$_3$ systems.

The thesis is organized as follows. In Chap. 1, we introduce the concept of piezoelectricity and related functionalities. In Chap. 2, we present an overview on the fundamental properties of ABO$_3$ perovskites, being the class of compounds of interest all along our study, and in the following Chap. 3 we present the basic of the Density Functional Theory, being the method used for our theoretical investigation. In Chap. 4, then, specific technical details of our DFT calculations are presented. The description of the obtained results thus follows. In detail, in Chap. 5, we carefully analyze the four parent compounds. Next, in Chap. 6 and Chap. 7, we address separately (Ba,Ca)TiO$_3$ and Ba(Ti,Zr)O$_3$ solid solutions of different compositions. Finally, Chap. 8 is devoted to a global discussion and conclusions.

Contents of Chap. 4, Chap. 5, part of Chap. 6, and Chap. 7 are published in D. Amoroso, A. Cano, and Ph. Ghosez, *Phys. Rev. B*, **97**, 174108 (2018).

Part I

Scientific Background

Chapter 1

Piezoelectricity

In one sentence, a piezoelectric device can be thought as a "translator" between mechanical and electrical energy [1]. Piezoelectricity, in fact, is the manifestation of a linear coupling between electrical and mechanical fields [2], namely production of electric charges on the surface as a consequence of exerted mechanical stress. The induced charges are proportional to the mechanical stress. Such property has been thus named according to its phenomenon; in fact, the word *piezoelectricity* is composed by the Greek verb $\pi\iota\acute{\varepsilon}\zeta\varepsilon\iota\nu$ (*piezein*), that means to press, and the word electricity, that is related to the Greek word $\acute{\eta}\lambda\varepsilon\kappa\tau\rho o\nu$ (*electron*), which means amber. In fact, ancient Greeks where the first to notice the manifestation of electricity in the attraction of small objects by rubbed amber.

The discovery of piezoelectricity dates back to 1880 by the French brothers Pierre and Jacques Curie. Specifically, they found this property in quartz crystal observing the development of an electric polarization after the compression of such material. This is what is called "direct piezoelectric effect". Later in 1881 Gabriel Lippmann hypothesized the "inverse piezoelectric effect", then demonstrated by the Curie brothers. In this case the opposite phenomenon is observed, that is the occurrence of expansion or contraction of the material, i.e. geometric strain, proportional to an applied electric field [3, 4]. Therefore, piezoelectric materials exhibit both the direct and inverse phenomena: the polarity associated to the generated surface charges depends on the direction of the exerted stress, that is compressive or tensile; conversely, depending on the direction of the applied electric field, the material either contracts or expands [2].

The linear relationships between the induced electric polarization P^{ind} along the direction i and the exerted stress σ, and, conversely, the strain ξ to the applied electric field $\mathcal{E}$ are

$$P_i^{ind} = d_{ij}\sigma_j$$
$$\xi_j = d_{ij}\mathcal{E}_i \tag{1.1}$$

where the stress σ_j and piezoelectric d_{ij} coefficients are expressed in Voigt notation, with $i = 1, 2, 3$ and $j = 1, 2, 3, 4, 5, 6$, being a second-rank and third-rank tensor respectively. Actually,

the link between the electrical and mechanical properties in piezoelectric materials can be represented via various parameters, including the piezoelectric charge or strain coefficient (d_{ij}), piezoelectric voltage or strain coefficients (g_{ij}), electromechanical coupling coefficient (k_{ij}) and mechanical qualify factor (Q_m). All of them are represented in Voigt notation, being the piezoelectric response represented by a third rank tensor as it relates the second rank mechanical and first rank electrical variables. Depending on the type of applications of interest, one can focus on the behavior of one parameter than the others. These key material parameters are referred as figures of merit for piezoelectric devices. Nevertheless, the primary parameter considered by experimentalists is the piezoelectric coefficient d_{ij}, which gives access directly to the intrinsic piezoelectric response of the material ($[d_{ij}] = [pC/N] = [pm/V]$ for the direct and inverse effect respectively). Detailed descriptions of all such interlocked parameters are provided in Refs. [3, 1], while an explicit formulation of the linear response between the stress and induced polarization will be given in Sec. 2.4.2.

From the symmetry point of view, a material can exhibit piezoelectricity only if its structure is non-centrosymmetric, that is it does not have an inversion center. This is directly linked to the fact that piezoelectricity represents the linear coupling between stress and electric polarization as well between as electric field and strain 1.1. In a centrosymmetric structure, in fact, d_{ij} has to be equal to $-d_{ij}$. Therefore, the only solution is that the piezoelectric coefficient is zero. This does not apply to structure lacking inversion symmetry. Therefore, of the 32 crystal classes, 21 are non-centrosymmetric, but 20 of these exhibit piezoelectricity. The non-centrosymmetric point group $O(432)$ makes an exception due combinations of associated symmetry operations. Among these, 10 are polar crystal classes, which show a spontaneous dipole moment and exhibit pyroelectricity, i.e. change in the polarization proportional to change in temperature. Switchability of such spontaneous polarization via an external electric field makes the material also ferroelectric. Therefore, ferroelectrics form a subgroup of the pyroelectric materials [5, 6].

1.1 Applications

The capability offered by the piezoelectric materials to couple mechanical and electrical properties, such as mechanical output in response to a voltage input, and alternatively, a voltage output in response to a mechanical input, is widely exploited in various so-called piezo-devices. They can be grouped in three main kinds of application: actuators, sensors and energy harvesting. The first being mostly related to the "inverse piezoelectric effect", while the latter ones to the "direct piezoelectric effect". Nevertheless, devices which rely concurrently on both the effects have been also widely developed. Out of these, there are also piezo- lighters and injectors. It is worth noting that together with the geometric deformation of the material related to the indirect effect, an other exploited effect is the associated generation of vibrations propagating as mechanical waves with specific frequencies. Therefore, certain piezoelectric crystals or ceramics can be used as source of sonic and ultrasonic waves. As a result, in a reverse way,

piezoelectrics can also behave as detector of external mechanical vibrations.

A huge number of works about piezoelectric materials and their transferring into applications exist. In the following a few examples of the well-established and impending applications have been extracted and listed. Reviews of reference among others are [3, 1, 5, 16, 17, 18, 19].

Daily life uses

Maybe we do not think about this, but we experience piezoelectricity everyday in our daily life at home, in the office and even in the path to the working place, and as well as in our free time when attending for instance a concert, a public manifestation or simply listening music etc. In fact, piezoelectricity is the working functionality in

- **quartz clock**: a quartz crystal (SiO_2) is used as resonator, producing oscillations of very precise frequency after being distorted by the applied voltage through an electrode, which in turn detects the produced electric signal;

- **lighters**: a spark is created by pressing a piezoelectric crystal, which generates an electric arc, igniting a flammable fluid or gas;

- **fuel injectors**: in direct injection engine, the fuel is injected into the combustion chamber via piezoelectric valves, which allows for fine electronic control over the fuel injection time and quantity;

- **inkjet printing**: a piezoelectric material behind each nozzle in a ink-filled chamber causes the stream of liquid into droplets at regular time intervals by means of the induced mechanical vibration. Such printing method is called "drop-on-demand";

- **microphones**: basically they convert sound into an electric signal in order to be recorded and/or reproduced; therefore, a piezoelectric material is used in the piezo-microphone, relying on its detection of acoustic waves, i.e. sound vibration, which in turn produce the voltage output. This functionality is the opposite of **loudspeakers**, which convert an electrical signal into sound. Therefore, piezoelectric materials, now working in the inverse regime, can be still used.

Laboratory apparatus

Piezoelectricity is also at the basis of the operation of some instrumental techniques thanks to the possibility to move and drive object with high accuracy via the strain effect induced by applied voltage.

- **AFM** (Atomic Force Microscopy): it is used for force measurement, imaging, and manipulation of different specimens thanks to the direct forces interacting between sample and tip. The precise movements of sample and tip are driven in x, y and z directions

by the so-called piezo-scanner, exploiting the reverse piezoelectric effect. The cantilever, which sustains the tip, can also be composed by a small piezoelectric element in order to oscillate around its resonance frequency, in the tapping-mode regime. It is worth to note that a variant functionality of the AFM is the **PFM** (Piezoresponse Force Microscopy) which allows imaging and manipulation of piezoelectric materials. Such characterization is achieved by using a conductive probe tip, which thus applies a current to the sample causing strain deformations of it.

- **STM** (Scanning Tunneling Microscopy): it is used for imaging surface at atomistic scale. It is based on the quantum tunneling effect, which occurs between the tip and the sample surface via an applied bias. As in the AFM, the surface scanning by the tip is driven by a piezoelectric;

- **ultrasonic cleaners**: they are used to clean many different type of objects going from samples, medical instruments to mechanical components via propagating ultrasonic waves in an appropriate cleaning solvent. The source of such ultrasound is thus a piezoelectric crystal or ceramic, which vibrates in response to the applied AC voltage.

Biomedical devices

The rising interest in developing noninvasive, biocompatible techniques in medical procedures makes piezoelectric materials good candidates for applications used for the real-time monitoring and adjustments of the health status of patients. Piezoelectrics thus result helpful in various steps of medical diagnosis procedures and treatment. Some examples are:

- **ultrasonography**: this technique includes all medical instruments using ultrasound for diagnostic imaging, generally named ecography. In this case a piezo-transducer, included in a probe, behaves both as source and detector of mechanical vibrations. The basic and general operation is that the waves generated by the piezo in response to the electrical input propagate into the body, being a probe in contact with the patients skin. Then, the echo caused by tissues and other body's parts are received by the same piezo-transducer, which converts it in electrical signals, in turns converted in images. It is noteworthy that the ultrasound themselves with varying frequencies can be used as medical treatment especially in orthopedics and traumatology;

- **biosensors**: they typically rely on the change of the initial vibration frequency of the piezoelectric material with the changing of the surrounding physiological parameters, in particular via the binding of any mass to the piezo-element. Therefore, sensitivity in micrograms is necessary to appreciate measurable change in oscillations. In the specific case of biodetectors, proteins, enzymes, cells or other organic structures chosen to act as bio-recognition components are attached to the piezo-transducer in order to interact/bind

with the specific chemical constituent (analyte) of interest to be detected. This interaction is so measured by the transducer, affecting the vibration of the piezo-element. The piezo-platform used for the biosensor construction is thus the so-called **microbalance**, which can be also used to detect microgram quantities in other fields than biomedical;

- **drug delivery**: via combined piezo-micropumps and microneedles drugs can enter the body via transdermal way at therapeutically useful rates.

Other applications

Basically, the piezo-based devices and instrumentations, like the ones previously presented, rely on the capability of the piezoelectric materials to behave like transducers, and so to be used as detectors and sensors. Therefore, a quite widespread range of other possible applications exist, going from piezo-motors, vibration reductors to sensors monitoring and assessing civil infrastructures etc.

Energy Harvesting

Mechanical vibrations source of mechanical energy that could be converted into electricity are everywhere around us: voluntary and involuntary human body motion/activity, vehicles in motion, working machines and instruments in mechanical industries, natural phenomena like wind, ocean/sea waves, earthquakes and so on. Actually, the scavenging of such wasted energy is quite challenging. Nevertheless, feasible solutions relying on the use of piezoelectric materials have begun to arise from different fields.

The biggest challenge in recent years is exploiting the human motion to power both portable devices and those which involve integration with the human body itself such as drug delivery, artificial/electronic tissues for robotics, health monitors etc. With respect to the latter, for instance, researches aimed to develop biocompatible nanogenerators for *in-vivo* self-powered devices avoiding surgical procedures to replace depleted batteries are running. Examples of various working small applications, are shoes based on piezo-soles, e-textiles based on piezo-yarns, nanogenerators and so on.

Large-scale applications of piezoelectricity for energy harvesting is then even more challenging. Nevertheless, since last decade, different interesting projects have been successfully led from collaborations between Universities and companies to develop "smart" floors and roads [20, 21, 22]. In the first case, the mechanical energy produced by substantial number of human steps in crowed places is reused to produce electricity, and so to illuminate the surrounding area itself. Such technology of energy floors has been adopted, for instance, in a dance club in Rotterdam and the subways in London and Tokyo as well as in occasion of the Olympic Games 2012. In the second case, instead, the idea is to make a piezo-asphalt in order to harvest energy from the motion of vehicles.

1.2 Materials

We have previously seen that the human body activity can be source of reusable energy by the help of piezo-transducers. Amazingly, the body reaction to human emotion can be a direct source of unexpected piezoelectric materials. People, in fact, usually manifest the reaction both to happiness and sadness by crying, and tears have been found to be piezoelectric. Such a feature, actually, has to be ascribed to a specific antibacterial enzyme, the lysozyme, contained in tears as well as in other organic secretions, milk and egg white, that exhibit piezoelectricity [7]. The discovery of lysozyme due to its bacteriolytic properties traces back to early 1900s (so even well before the discovery of $BaTiO_3$ as we will see later) by A. Flaming [8], the discoverer of penicillin. Then, only recently, its piezoelectric properties have been demonstrated [9, 10]. Actually, the lysozyme is not the only case of piezoelectric of biological origin, but also other proteins as elastin or collagen, the latter forming bones and tendons, or amino acids, forming proteins, exhibit piezoelectricity [11, 12, 13, 14]. In particular, for instance, piezoelectricity in bones was already known since the 1950s [15]. Nevertheless, the piezoelectric response exhibited by these biological materials is generally low, and so limiting their use in technological applications. Such a behavior is then opposite in a wide variety of inorganic materials among which the most used quartz (SiO_2), barium titanate (BTO), lead zirconate titanate (PZT) and polyvinylidene fluoride (PVDF).

1.2.1 A brief overview on inorganic piezoeletric materials

As mentioned at the beginning, piezoelectricity was discovered in quartz single crystal in 1880, but only the need of ultrasonic sonar and technologies for military purposes during the World Wars boosted the search for other materials with enhanced dielectric, piezoelectric and ferroelectric properties. Various titanates, including $BaTiO_3$, $CaTiO_3$, $SrTiO_3$, $PbTiO_3$ and $PbZrO_3$ among others, have been thus synthesized between the 1940s and 1950s. In particular, $BaTiO_3$ was discovered independently by US, Japan and Russia during the World War II for its high permittivity. Only after few years, such high dielectric properties have been associated to its ferroelectric nature [23]. Later on, different set of measurements accompanied by the phenomenological theory approach of Devonshire shed light on its piezoelectric and related properties [24, 25, 26]. Nevertheless, in order to increase the Curie temperature of BTO, i.e. the temperature of transition from the cubic to the ferroelectric tetragonal phase, to higher value than 120° C and to lower the transition temperature to the orthorhombic ferroelectric phase, various cations replacements were studied. The aim was thus to enlarge the range of operating temperature. These trials led to the discovery of $Pb(Zr,Ti)O_3$ system by Japanese researcher groups [27, 28]. Then, the determination of its phase diagram [29] and superior piezoelectric properties [30] followed. It is noteworthy to mention that, in the same period, McQuarrie and Behnke were the first to synthesize the quaternary system $(Ba,Ca)(Ti,Zr)O_3$ [31]; however, the poor temperature stability of the associated piezoelectric properties and the breakthrough

of PZT threw shadow on this and related solid solutions until last decades. From the 1960s, then, relying on the high performances provided by PZT, an extensive production and characterization of Pb-based piezoelectric solid solutions followed, like $Pb(Mg_{1/3}Nb_{2/3})O_3$ (PMN), $Pb(Zn_{1/3}Nb_{2/3})O_3$ (PZN), $Pb(Sn_{1/2}Nb_{1/2})O_3$ (PSN) among many others and, later on, more complex associated solid solutions via the combination of $PbTiO_3$ (PT), like PMN-PT, PZN-PT and PSN-PT. An extensive comparative description of such Pb-based systems and associated list of references are provided in Ref. [32].

In 1969, interesting piezoelectric properties were also found in a completely different system, the polymer polyvinylidene fluoride (PVDF). This discovery has to be once again ascribed to Japanese researchers [33, 34]. Later, it was been found to be also pyroelectric and ferroelectric [35]. Over the last decades, therefore, PVDF is facing increasing interest especially for the development of wearable e-textile functionalities [36, 37, 38]. Piezoceramic-polymer composites based on PZT-PVDF have been also developed, obtaining an enhancement of the piezoelectric performances of the PVDF alone [39].

In the 21st century, a new boost in the search for new high-performing piezoelectric materials has been due to "environmental concerns", which have widely restricted the use of Pb and led researchers to the search for alternative lead-free piezoelectrics. In particular, the discussion about the toxicity of lead-containing ceramics is mostly related to the recycling process of the lead-containing components, being metallic Pb and lead oxide PbO known to be toxic, even if at different level (see Ref. [1] and references therein). In this respect, therefore, the European Union (EU) has promoted various regulations to restrict the use of Pb and Pb-containing materials in order to reduce their impact on health and environment. The two main sets of rules by the EU are the directive on the restriction of the use of certain hazardous substances in electrical and electronic equipment [40], abbreviated as RoHS, and the REACH (Registration, Evaluation, Authorisation and Restriction of Chemical Substances) regulation (explanation and regulation can be found in the official website of the European Chemicals Agency (ECHA) [41].)

In this respect, the inspiring precursor work was likely the publication by Takenake *et al.* in 1991 about the Ba-modified bismuth sodium titanate $(Bi_{1/2}Na_{1/2})_{1-x}TiO_3$-$Ba_xTiO_3$ (BNT-BT), in which he referred to the BNT-based solid solutions as a new group of lead-free piezoelectric ceramics. [42]. Therefore, a huge number of works with renewed interest in investigating and improving BNT-based systems followed. Then, another more recent stimulating work by Saito *et al.* in 2004 about the enhanced piezoelectric properties in complex modified systems based on $(K,Na)NbO_3$ (KNN) [43] has boosted the interest in the investigation and development of KNN-based materials. Later on in 2009, the outstanding piezoelectric properties found in Ca- and Zr-modified barium titanate $(Ba,Ca)(Ti,Zr)O_3$ (BCTZ) by Liu and Ren [44] has widely renewed the interest in BTO-based materials. Detailed reviews about various lead-free materials including the aforementioned ones are Refs. [45, 46, 2].

Piezoelectricity and composition-induced phase boundaries

The common factor in all the aforementioned developed piezoelectric materials is the presence of the so-called morphotropic phase boundary (MPB), a compositional region separating two competing ferroelectric phases in the composition-temperature (x-T) phase diagram [47]. The achievement of such composition-induced phase transition thus typically relies on the design of solid solutions, which have compounds with different polar ground-states, typically being rhombohedral (R), orthorhombic (O) or tetragonal (T) with spontaneous polarization $\boldsymbol{P}$ along [111], [011] or [001] directions respectively, located as parent end members. After the first observation of this feature in the phase diagram of PZT and the observed connection with the enhanced piezoelectricity, the search for the improved piezoelectric materials has been thus based on the achievement of the MPB. The understanding of the remarkable piezoelectric properties of PZT is, in fact, the "polarization rotation" between the adjacent rhombohedral R- and T- phases through one (or more) in-

Figure 1.1: PTZ phase diagram from [50]. Authors report in open circles data from B. Jaffe, W.R. Cook, and H. Jaffe, *Piezoelectric Ceramics* (Academic Press, London, 1971) and in solid symbols the $F_T - F_M$ and $P_C - F_T$ transition temperatures [50].

termediate monoclinic phases [48, 49, 50, 51]. More generally then, the composition-induced ferro-ferro transition causes the instability of the polarization state at the MPB region so that the polarization direction can be easily rotated by external stress or electric field, resulting in high piezoelectricity [52, 44]. In other words, such regions of the (x-T) phase diagram provide the condition for minimal anisotropy with respect to directions of the polarization, being the minima of the free energy associated to different polar states, i.e. $\boldsymbol{P}$ oriented along different directions in space, degenerate. Such isotropic energy landscape, corresponding to a rather flat energy barrier between different polar states, gives rise to a rotational instability in the spontaneous polarization, which in turn results in the enhancement of the piezoelectric response. It should be also point out that the elastic softening, i.e. a strong coupling between the internal degrees of freedom and strain in the system, is another key factor to get giant piezoelectric response [52, 46]. Therefore, if the presence of bridging monoclinic phases is a necessary condition for a large piezoelectric response is still matter of debate [53, 46]. Nevertheless, its appearance seems naturally favored by the almost isotropic free energy associated to the original polar ground-states of the parent end-members of the solid solutions [46].

Another important feature, which determines the technological relevance of the various
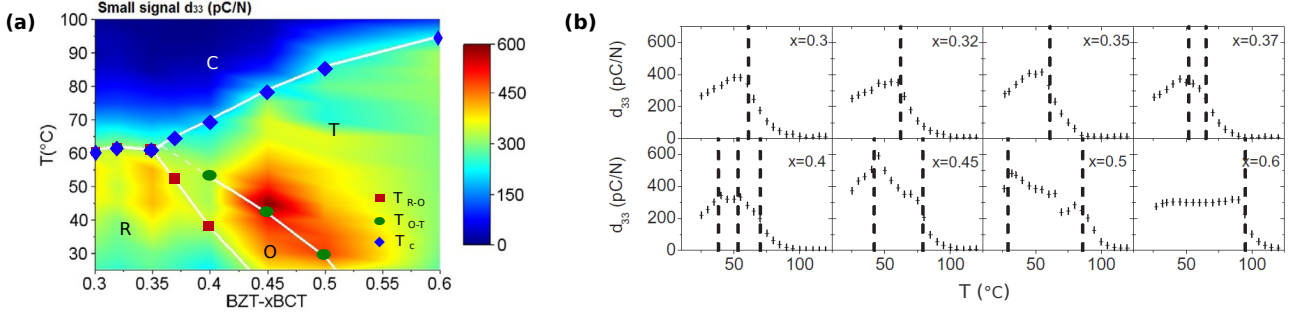
Figure 1.2: (a) Phase diagram overlapped to the contour plot of the piezoelectric coefficient d_{33} and (b) behavior of d_{33} as a function of temperature in BCTZ. In the latter graph, authors mark with dashed lines the peak positions indicating phase transitions. Adapted from Ref. [54].

piezoelectric materials, is the stability of the piezoelectric properties as a function of varying temperature. With respect to the latter, it is the trend of the phase boundary line in the (x-T) diagram to affect this feature, beyond the intrinsic change of the properties of the material with temperature. PZT, for example, exhibits a nearly temperature-independent, i.e. vertical, boundary line, as illustrated in Fig. 1.1 from Ref. [50]. In the ferroelectric community, such nearly vertical transition line is the one properly termed morphotropic phase boundary (MPB), while a phase boundary line showing substantial variation with temperature is termed instead polymorphic phase boundary (PPB). The latter type results more typical of the BT-based solid solution [46]. In particular, this is true for BCTZ, which appears a suitable candidate for applications with usage temperature below 100° C [1, 106]. Phase diagram and trends of the piezoelectric coefficient d_{33} in BCTZ reported in Ref. [54] are shown in Fig. 1.2. Moreover, a particular and interesting characteristic of BCTZ is its biocompatibility, making it one of the most promising piezoelectric materials to be used in the biomedical devices [55, 56, 57, 58].

A detailed review about piezoelectricity-MPB relationships is reported by Cordero [46].

1.3 Aim of the thesis

Among the BTO-based systems, BCTZ has appeared as the most attractive one, so that it has been widely experimentally investigated. Several experimental works concerning synthesis, structure, energetics and dielectric, piezoelectric, and elastic properties have been already carried out and further works aimed at improving its properties are still ongoing. Nevertheless, despite there are evidences of the fact that increasing Ca- and Zr- content deeply affects the ferroelectric features of BTO, producing the (x-T) phase diagram and related properties of interest, the physical mechanisms behind the occurrence of such quasi-isotropic energy landscape remain still unclear. Up to now, in fact, theoretical characterizations of BCTZ are few and mostly limited to reproduce the experimental evidences instead of understanding and discuss the underlying physics. Results and details of the various experimental works on BCTZ are reported in Acosta *et al.* [2] and references therein.

In this respect, in the present thesis, we try to unravel the microscopic mechanisms tuning the ferroelectric and piezoelectric properties of these solid solutions by means of a step-by-step analysis and systematic comparisons, focusing on the distinct effects arising from the end members (Ba,Ca)TiO$_3$ (BCT) and Ba(Ti,Zr)O$_3$ (BTZ) and related pure parent compounds. Accordingly, in the following, in order to guarantee a complete understanding of the work, an introduction to the main physical concepts affecting these systems and to the used method precedes the presentation of the specific results.

Chapter 2

Fundamentals of Perovskite Oxides: a general overview

In the previous chapter the concept of ferroelectricity has been introduced in relationship with piezoelectricity, being a fundamental properties of most of the good piezoelectric materials. In particular, this is true for BCTZ perovskites and its parent end members BCT and BZT, as well as the building block BTO.
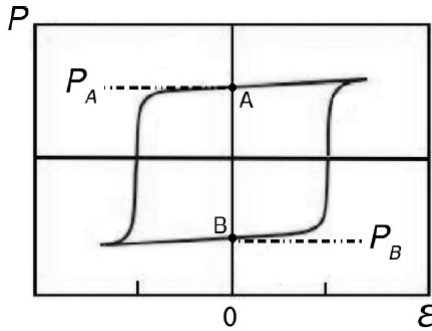
Figure 2.1: Schematic illustration of a typical hysteresis loop. From Ref. [59]. The spontaneous polarization is defined as $P_s = (P_B - P_A)/2$, being a zero-field property [60].

Ferroelectric (FE) materials are insulating systems that exhibit spontaneous macroscopic polarization, switchable by an applied electric field. The concept of electric polarization is therefore the key to understand ferroelectricity. At equilibrium, a FE material is characterized by spontaneous polar atomic distortion. In particular, ferroelectric perovskites exhibit a high-temperature paraelectric reference, which undergoes ferroelectric distortion at decreasing temperature. The symmetry breaking between the paraelectric and ferroelectric phases can be described as a first- or second-order structural phase transition within the Landau theory, where the polar lattice distortion is the primary order parameter. Systems in which the polarization is a second order parameter linearly coupled to nonpolar lattice distortions or to the magnetization are called "improper" ferroelectrics.

The absolute bulk macroscopic polarization $\mathbf{P}$ of materials is not directly accessible, rather most measurements give information about changes of polarization (i.e. its derivatives), such as spontaneous polarization, permittivity, pyroelectric coefficient, piezoelectric tensor and Born charges. Usually, the switching process in a ferroelectric material is associated with a hysteresis curve of the electric polarization $\mathbf{P}$ as a function of the field strength $\mathbf{E}$ between opposite polarities, as illustrated in Fig. 2.1. The critical electric field necessary to reverse the polarization is known as coercive field. Such electric bi-stability, that is the presence of spontaneous, non-

volatile and switchable polarization, can be used for data storage. Furthermore, the transition from the paraelectric to the ferroelectric phase depends on temperature leading to the definition of the Curie temperature T_c. As this temperature is approached, the dielectric constant ϵ, which in most cases obeys the Curie-Weiss law, reaches large values useful for capacitor applications. Other important properties from the technological point of view are pyroelectricity and piezoelectricity earlier introduced. In pyroelectrics, for instance, a temperature dependence of the spontaneous polarization generates an electric current when both ends of the polarized ferroelectric are short-circuited. Below T_c the pyroelectric effect becomes large and this feature is useful in a variety of thermal-image sensors and infrared detectors. In piezoelectrics, electric and mechanical properties are coupled: an applied stress generates polarization, whereas the electric field causes strain in the material. Such piezoelectric responses are employed in actuators, transducers, ultrasonic motors and other electromechanical devices, as widely analyzed in Chap. 1.

In the following we will focus on the ferroelectric and related properties of the most studied family of compounds known as perovskite oxides. In addition to the intent to introduce the context, this will allow to introduce the main concepts investigated in this thesis.

2.1 ABO_3 perovskites: generalities

A widely studied class of oxides is that known as *perovskite* oxides with general ABO_3 formula unit, where A and B represent cation elements. Originally, the name of *perovskite* had been assigned to the mineral of calcium titanate ($CaTiO_3$) discovered in the Ural Mountains in 1839 by Gustave Rose and named in honor of the Russian mineralogist Lev A. von Perovski. Then, this name has been lent to the class of compounds showing the same type of crystal structure. Although $CaTiO_3$ shows as orthorhombic ground state, the name perovskite is often given to the high-symmetry reference containing 5 atoms with space-group $Pm\bar{3}m$ (O_1^h, No. 221). As
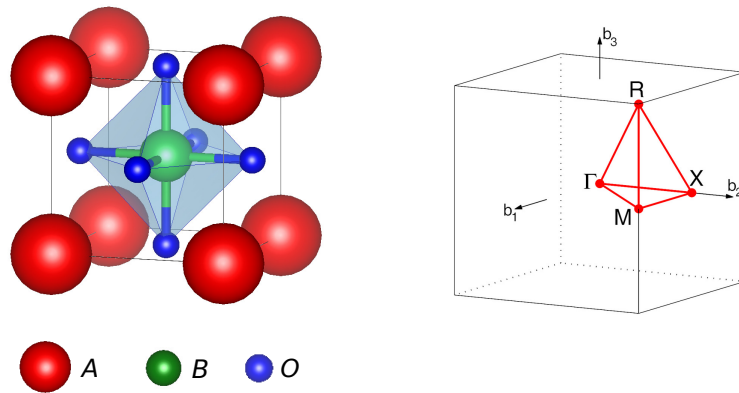
Figure 2.2: (Left) Schematic view of the 5 atoms unit cell of the ABO_3 ideal cubic perovskite structure: the B atom (green) sits at the center of corner-shared oxygen octahedra (blue), while A atoms (red) occupies the enclosing holes. (Right) Schematic view of the simple cubic Brillouin zone [62].

illustrated in Fig. 2.2, a possible description of such a structure is: the A atom sits at the corner of the cube, the B atom sits at the center and each oxygen occupies the center of each face. Therefore, in the perovskite structure, the B atom is surrounded by 6 equidistant first neighbors oxygens, arranged at the corners of a regular octahedron. The octahedra are corner-shared, enclosing holes which are occupied by A atoms. Each A atom has 12 equidistant O atoms. Each O atom has 2 B-type and 4 A-type atoms as first neighbors [61]. An alternative description is that with the B atom at the corner and the A atom at the center of the cube.

Despite their apparent similarities, distinct members of the family can exhibit different physical properties depending on composition and cationic ordering. Starting from the high-temperature cubic reference, the majority of these compounds undergo polar and/or non-polar structural phase transitions when the temperature is lowered. This means that the cubic phase is unstable with respect to energy-lowering distortions. Most of the appearing distortions are related to a structural frustration of the cubic perovskite structure. An empirical criterion for predicting the tendency of the ABO_3 cubic perovskite to be distorted and related type of distortion is the tolerance factor based on the Goldschmidt's rules [63]: the anion-cation distance is obtained as the sum of their ionic radii being a cation surrounded only by as many anions as can touch it [61]. Accordingly, the relationship defining the ideal cubic perovskite structure is

$$r_A + r_O = \sqrt{2}(r_B + r_O) \tag{2.1}$$

and the tolerance factor t provides the deviation from the latter, being defined as

$$t = \frac{r_A + r_O}{\sqrt{2}(r_B + r_O)} \tag{2.2}$$

where r_A, r_B and r_O are the ionic radii of the A-type, B-type and O atoms [1]. When $t > 1$, the B cation is too small for its site so that it will off-center. Such motion eventually produces a polar distortion leading to a so called B-driven ferrolectricity, as in the case of BaTiO$_3$. Conversely, when $t < 1$, the A cation is too small in comparison to the hole between the oxygen octahedra. Therefore, both polar off-centering of the A-cation leading to A-driven ferroelectricity or antipolar motions and/or oxygen rotations can take place, as in the case of CaTiO$_3$ and CaZrO$_3$. The ideal condition $t \simeq 1$ is rarely satisfied except for BaZrO$_3$.

We will present the specific structural properties of the aforementioned ABO_3 systems in the results part.

2.2   Ginzburg-Landau-Devonshire theory

As previously introduced, the main interesting feature of the ABO_3 ferroelectric perovskites is to undergo with temperature different sequences of structural phases transition. Therefore,

---

[1]Alternatively, one can use the bond-valence model to calculate the ideal A-O and B-O bond distances [64].

theoretical predictions should take explicitly into account the temperature effect, omitted in the ground-state theory. In this respect, the most popular approach to describe the temperature behavior of ferroelectrics at the macroscopic level is the phenomenological Ginzburg-Landau-Devonshire theory [25, 65], that is appropriate for bulk systems with spatially uniform polarization.

In general, the thermodynamic state of bulk ferroelectrics, and so the associated thermodynamic potential, the *Gibbs free energy*, can be specified by three independent quantities among the conjugate pairs temperature-entropy (T, S), stress-strain (σ, ξ), and electric field-electric displacement $(\mathcal{E}, D$ or eventually polarization $P)$, such as

$$G = U - TS - \xi\sigma - \mathcal{E}D \tag{2.3}$$

where T is the temperature, S the entropy and U the internal energy. Then, according to the second thermodynamic principle, the equilibrium (stable) state is determined by the values of the corresponding variables which minimize such energy. For a phase transition in temperature with no external pressure $(\sigma = 0)$ and field $(\mathcal{E} = 0)$, the thermodynamic potential reduces to the *Helmholtz free energy*, that is

$$F = U - TS \tag{2.4}$$

The main idea behind the Landau theory is that, in the vicinity of a phase transition, the free energy can be expressed as a power series of the order parameters. The minimization of the Landau free energy then gives the Helmholtz free energy.

Specifically, in the so-called "proper" ferroelectrics, the polarization (or equivalently the polar distortion) is taken as first order parameter of the expansion. In the specific case of perovskite oxides, such expansion concerns the energy of the high-symmetry non-polar phase, under the hypothesis that the expansion remains valid above and below the phase transition temperature. This corresponds to the fact that non-centrosymmetric structure can be obtained from the high-symmetry structure by means of small distortion.

Let us exemplify the approach considering that the strain is zero and the polarization is directed along one of the cartesian direction. Then the Taylor expansion of the energy is

$$F = \frac{1}{2}\alpha P^2 + \frac{1}{4}\beta P^4 + \frac{1}{6}\gamma P^6 \tag{2.5}$$

where α is a temperature dependent parameter defined as $\alpha = a_0(T - T_0)$ with a_0 a positive constant and T_0 the temperature at which α changes sign; γ is also a positive coefficient, while β can take values both positive and negative, determining the nature of the transition and the trend of the polarization.

If $\beta > 0$, then a second-order transition occurs at $T = T_0$, and the free energy and the polarization evolve continuously as a function of decreasing temperature: for $T > T_0$ the quadratic term is positive and the thermodynamic functional is a single well with its minimum
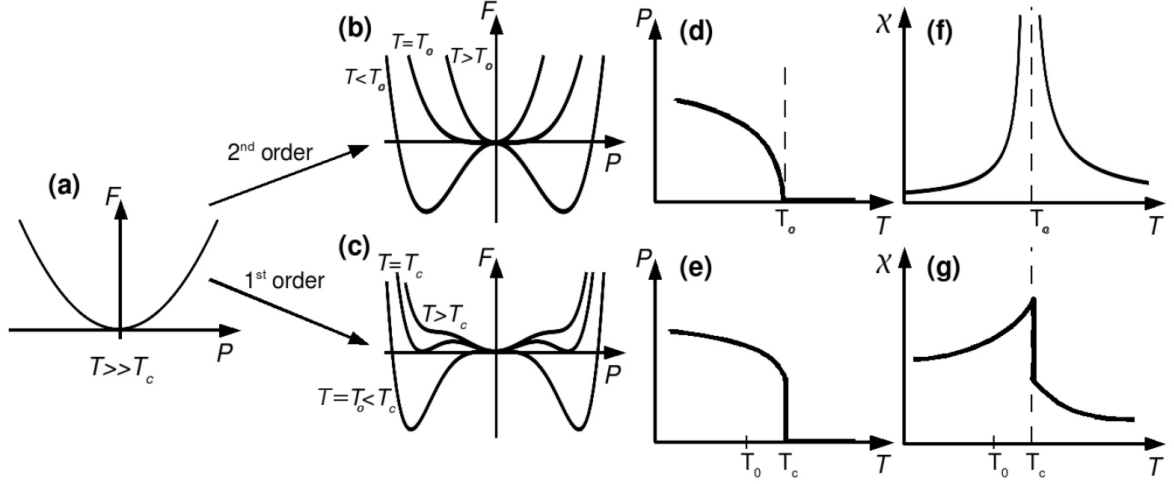
Figure 2.3: (a) Free energy as a function of polarization for the paraelectric phase. (b) Free energy as a function of polarization for a ferroelectric material in a second-order phase transition at $T > T_0$, $T = T_0$ and $T < T_0$. (d) and (f) are respectively the spontaneous polarization P and the dielectric susceptibility χ as a function of temperature for a second-order phase transition. (c) Free energy as a function of polarization for a ferroelectric material in a first-order phase transition at $T > T_c$, $T = T_c$ and $T < T_c$. (e) and (g) are respectively the spontaneous polarization P and the susceptibility χ as a function of temperature for a first-order phase transition. Adapted from Refs. [66, 59].

corresponding to the non-polar $P = 0$ phase; for $T < T_0$ the quadratic term is negative and the curve displays the typical double well shape with two minima at $P = \pm P_0$ [Fig. 2.3(b)]. The spontaneous polarization P_0 is estimated by the minimization procedure of the free energy F, such as $\partial F/\partial P = 0$, while the susceptibility χ from the relations $1/\chi = \partial \mathcal{E}/\partial P = \partial^2 F/\partial P^2$. Being γ positive, the sixth order term in the expansion (2.5) can be neglected. The results are

$$P_0 = \pm\sqrt{\frac{a_0}{\beta}(T_0 - T)} \tag{2.6}$$

$$\chi = \begin{cases} [a_0(T - T_0)]^{-1} & \text{if} \quad T > T_0 \\ [-2a_0(T - T_0)]^{-1} & \text{if} \quad T < T_0 \end{cases} \tag{2.7}$$

If $\beta < 0$, then a first-order transition occurs at $T = T_c$. With the negative quartic coefficient, even when $T > T_0$ the free energy may have two extra local minima at $P \neq 0$. When the temperature decreases, the polar state will drop in energy below that of the non-polar state, becoming the thermodynamically favored configuration. The temperature at which the polar and non-polar states will be energetically degenerate is the Curie temperature T_c, i.e. the transition temperature. T_c exceeds T_0 defined in the case of second-order transitions. At any temperature between T_c and T_0 the non-polar phase exists as a local minimum of the free energy [Fig. 2.3(c)]. The most important feature of this phase transition is that the order parameter jumps discontinuously to zero at T_c [66], so that the first-order transition is also called discontinuous transition. The observable fingerprint of this type of transition is the occurrence

of a temperature hysteresis ΔT, i.e. the difference between the transition temperatures upon cooling and heating of the crystal [67]. Trends for the free energy as a function of polarization and for the polarization and dielectric susceptibility as a function of temperature are schematically shown in Fig. 2.3 both for the second- and first- order transitions.

In the case of phase transitions related to oxygen rotations, the same expansion of the free energy can be made, in which the first order parameter is now ϕ describing the rotations. Interesting systems are those in which the primary order parameter ϕ couples linearly with the parameter P of second order now, driving thus the system to exhibit spontaneous polarization as secondary effect. Such a mechanism is referred as "improper ferroelectricity" [69]. Specifically, systems in which P linearly couples with only one independent primary order parameter, like same type of rotations ϕ, such as $\sim \lambda \phi^3 P$ with λ a coupling coefficient, are properly termed "improper ferroelectrics" [70]; systems in which P couples linearly with two independent primary order parameters, like the "in-phase" ϕ^+ and "out-of-phase" ϕ^- rotations, such as $\sim \lambda \phi^+ \phi^- P$, are termed "hybrid improper ferroelectrics" [71]. Systems in which the coupling is bi-quadratic, such as $\sim \lambda \phi^2 P^2$, are termed "triggered" [72].

In order to properly take into account the contribution to the energy due to modification of the cell shape and size induced by the structural distortions, the strain effect can be also included as a secondary order parameter ξ in the energy expansion [92]. In particular, in the case of ferroelectrics, this allows to properly take into account the polarization-strain coupling, which is eventually responsible for the piezoelectric response. Using a simplified notation and considering uniaxial strain, the elastic interaction introduces the terms

$$C\xi^2 + Q\xi P^2 \tag{2.8}$$

where C is the elastic stiffness of the material and Q is the coupling coefficient between polarization and strain. The second term takes into account the modification of the strain induced by the polar distortion, i.e. by the polarization, and Q is referred as the electrostriction coefficient. Therefore, minimizing the energy with respect to the strain to find the equilibrium condition, such as $\partial F/\partial \xi = 0$, the resulting strain is

$$\xi = -\frac{Q}{C} P^2 \tag{2.9}$$

Being the piezoelectric coefficient d defined as the linear variation of the strain with respect to the electric field (1.1), it thus results that $d \sim Q\chi P$. According to this expression, for ferroelectrics whose paraelectric phase is centrosymmetric, piezoelectricity originates from the electrostrictive effect, spontaneous polarization, and the dielectric response [46, 68].

As mentioned at the beginning of this section, the Ginzburg-Landau-Devonshire theory is suited to reproduce and describe the temperature-dependent behavior of ferroelectric properties at the macroscopic level. Nevertheless, this approach cannot provide description of the underlying physics, relying on the final macroscopic manifestation of such properties. Conversely, such a capability is supplied by the first-principles theory (that will be introduced in Chap. 3), accessing the physics and microscopic mechanisms which determine the appearance of those properties. In particular, this is due to the provided precise description of the lattice dynamics and electronic properties of the materials. However, this is in practice restricted to zero Kelvin. Implemented fist-principles molecular dynamics (MD) simulations are still restricted to small systems and time scale, being computationally demanding. A valuable alternative approach is the effective Hamiltonian approach based on first-principles [73, 74, 75]. Similarly to the Landau theory, such approach relies on the identification of the most important degrees of freedom governing the phase transition and the subsequent expansion of the energy with respect to these degrees of freedom with coefficients initialized from DFT calculations.

2.3 Lattice dynamics

As mentioned in the previous section, the Ginzburg-Landau-Devonshire theory is a macroscopic approach able to describe the behavior of the macroscopic observables around the phase transition. In the specific case of ferroelectrics, this approach consists in expanding the energy in terms of the spontaneous polarization, considered as order parameter. Nevertheless, no access to the microscopic mechanisms, such as atomic distortions giving rise to such polarization, can be provided, and so a direct connection with the crystal lattice dynamics is missing in such phenomenological description. In fact, at microscopic level, the condition for a crystal to be stable against small deformations is that all the vibrational modes should have real frequencies ω. Therefore, imaginary frequencies are associated with atomic displacements with respect to which the reference structure is unstable.

In this respect, Cochran has been the first[2] to analyze the problem of structural phase transitions in the framework of the lattice dynamics [89, 90]. Focusing on ferroelectric phase transitions, he considered one of the lattice mode as the basic variable, introducing the notion of "soft-mode". In particular, he associated the para-ferro transition with the softening of a zone-center transverse optic (TO) phonon, which "freezes-in" below the transition temperature, giving rise to a dipolar moment in each unit cell: in the high-temperature paraelectric phase, there is a lattice (polar) mode for which the frequency goes to zero on decreasing the temperature toward the transition temperature T_c to generate the ferroelectric crystal structure. On the other side of the phase transition, as the phase boundary is approached with increasing temperature in the ferroelectric phase, the lowest-frequency polar phonon become

---

[2]It should be noted that, actually, the concept of "soft-mode" was already introduced by Ginzburg in 1949 [88].

softer decreasing to zero near the transition temperature. The atomic displacements associated with the soft mode are the same as the deformation of the structure in the low-temperature phase [91, 93]. Then, the "soft-mode theory" has been widely accepted as general description of structural phase transitions, which thus arise from the progressive softening of a specific phonon mode with temperature, which condenses into the structure at the phase transition [94, 95, 96]. Such mechanism is the one generally characterizing the so-called displacive phase transition.

In particular, Cochran suggested a temperature dependence of the soft mode of the type $\omega^2 \propto (T - T_c)$. The soft-mode model is illustrated schematically in Fig. 2.4: at $T < T_c$ the structure of the high-symmetry phase is unstable with respect to the distortion to the low-symmetry phase, and the frequency of the soft mode has an imaginary value [91]. At the atomistic level, in fact, it results that the temperature dependence of the soft-mode arises from the anharmonic coupling of the soft mode with other modes, giving rise to a renormalization of the harmonic frequency [97, 59], such as

$$\tilde{\omega}^2 = \omega_0^2 + \frac{k_B T}{2} \sum_i \frac{\alpha_i^4}{\omega_i^2} \qquad (2.10)$$

Figure 2.4: Schematic representation of the behavior of the soft-mode $\tilde{\omega}^2 \propto (T - T_c)$: at low temperature $T < T_c$ the soft-mode in the reference structure is unstable, thus the structure of the high-temperature phase is unstable. On increasing temperature T, the anharmonic interactions add a positive contribution to the negative value of ω_0^2 (Eq. 2.10): first, the frequency reaches zero at T_c; then, the frequency becomes real for higher T. Adapted from Ref. [91].

where ω_0 is the harmonic frequency of the soft mode (which is negative, being the unstable mode), k_B is the Boltzmann constant and α_i is the anharmonic coupling coefficient of the soft mode with the mode i of frequency ω_i. The transition temperature T_c, being that at which the frequency of the soft mode $\tilde{\omega}$ reaches zero, results $T_c = -\frac{2\omega_0^2}{k_B \alpha}$, with $\alpha = \sum_i \frac{\alpha_i^4}{\omega_i^2}$. The temperature dependence of $\tilde{\omega}$ can thus be rewritten as

$$\tilde{\omega}^2 = -\frac{\omega_0^2}{T_c}(T - T_c) = \omega_0^2 - \frac{\omega_0^2}{T_c}T \qquad (2.11)$$

The result of (2.11) is that the square of the phonon frequencies vary approximately linearly with temperature. The frequency at $T = 0$ K corresponds to the harmonic value ω_0, which can be determined by solving of the dynamical equation of the crystal lattice.

The "soft-mode theory" thus results a bridge linking the microscopic lattice dynamics and the macroscopic Ginzburg-Landau-Devonshire theory. In fact, it is possible to recognize an equivalence between the α parameter in the energy expansion (2.5) and the square of the harmonic frequency, both linearly depending on temperature and determining the occurrence of the

phase transition. For displacive phase transitions, therefore, the Ginzburg-Landau-Devonshire theory is strictly related to the soft-mode theory, and although the expansion parameters may be obtained empirically, they can also be related to fundamental quantities accessible, for example, from first-principles calculations [91].

2.3.1 The dynamical equation

As previously mentioned, we are interested here in small atomic displacements $\boldsymbol{\tau}$ from the paraelectric reference around the equilibrium configuration. Supposing such displacements are small with respect to the lattice constant, so that it remains possible to work in the harmonic approximation, and within the *adiabatic* approximation, in which it is considered that the electrons are in their ground-state for any instantaneous ionic configuration, the energy of a periodic crystal can be expanded in Taylor series around the equilibrium position up to the second order as

$$E_{e+i}(\{\boldsymbol{R}_k^a\}) = E_{e+i}^{(0)} + \sum_{ak\alpha} \sum_{bk'\beta} \frac{1}{2} \Big(\frac{\partial^2 E_{e+i}}{\partial \tau_{k\alpha}^a \partial \tau_{k'\beta}^b} \Big) \tau_{k\alpha}^a \tau_{k'\beta}^b \tag{2.12}$$

where labels a and b refer to the unit cell, k and k' to the atoms and α and β to the spatial directions. By substituting Eq. (2.12) in the classical equation of motion for the nuclei, we obtain

$$M_k \frac{\partial^2 \tau_{k\alpha}^a}{\partial t^2} = -\frac{\partial E_{e+i}}{\partial \tau_{k\alpha}^a} = -\sum_{bk'\beta} \Big(\frac{\partial^2 E_{e+i}}{\partial \tau_{k\alpha}^a \partial \tau_{k'\beta}^b} \Big) \tau_{k'\beta}^b \tag{2.13}$$

from which we can identify the force constants terms associated to a classical $3N$ harmonic oscillators system. Specifically, the matrix of the interatomic force constants (IFCs) in real space is defined as

$$C_{k\alpha,k'\beta}(a,b) = \Big(\frac{\partial^2 E_{e+i}}{\partial \tau_{k\alpha}^a \partial \tau_{k'\beta}^b} \Big) \tag{2.14}$$

For each atom in the periodic crystal there are 3 equations of motion of the type (2.13) with general solution of the form:

$$\tau_{k\alpha}^a(t) = \eta_{m\boldsymbol{q}}(k\alpha) e^{i\mathbf{q}\cdot\mathbf{R^a}} e^{i\omega_m t} \tag{2.15}$$

for which the vibrations or normal modes of the ions (*phonons*) are identified by the wave vector $\boldsymbol{q}$ compatible with the Born-von Karman boundary conditions. Replacing (2.15) into Eq. (2.13), we have

$$- M_k \eta_{m\boldsymbol{q}}(k\alpha)\omega_{m\boldsymbol{q}}^2 = -\sum_{bk'\beta} C_{k\alpha,k'\beta}(a,b)\eta_{m\boldsymbol{q}}(k'\beta) e^{-i\mathbf{q}\cdot(\mathbf{R^a}-\mathbf{R^b})} \tag{2.16}$$

where we can recognize the Fourier transform of the force constant matrix element as

$$\tilde{C}_{k\alpha,k'\beta}(\boldsymbol{q}) = \sum_b C_{k\alpha,k'\beta}(a,b) e^{-i\mathbf{q}\cdot(\mathbf{R^a}-\mathbf{R^b})} \tag{2.17}$$

Therefore, the displacement of the ions is described by the following dynamical equation:

$$\sum_{k'\beta} \tilde{C}_{k\alpha,k'\beta}(\boldsymbol{q})\eta_{m\boldsymbol{q}}(k'\beta) = M_k\omega_{m\boldsymbol{q}}^2\eta_{m\boldsymbol{q}}(k\alpha) \tag{2.18}$$

Equivalently, the normal modes are solution of the following eigenvalue problem:

$$\sum_{k'\beta} \tilde{D}_{k\alpha,k'\beta}(\boldsymbol{q})\gamma_{m\boldsymbol{q}}(k'\beta) = \omega_{m\boldsymbol{q}}^2\gamma_{m\boldsymbol{q}}(k\alpha) \tag{2.19}$$

with quantities connected as

$$\tilde{D}_{k\alpha,k'\beta}(\boldsymbol{q}) = \tilde{C}_{k\alpha,k'\beta}(\boldsymbol{q})/\sqrt{(M_k M_{k'})} \tag{2.20}$$

This quantity is called the dynamical matrix.

The square root of the eigenvalues, $\omega_{m\boldsymbol{q}}$, of the equation (2.19) are the phonon frequencies of mode m at wave vector $\boldsymbol{q}$ with associated eigenvector $\gamma_{m\boldsymbol{q}}$. The $\eta_{m\boldsymbol{q}}$ are usually referred to as the phonon eigendisplacements. They are normalized such that $< \eta|M|\eta >= 1$, with mass matrix $M = M\delta_{kk'}$. Accordingly, eigenvectors and eigendisplacements are related as $\gamma = \sqrt{M}\eta$.

Notice that the phonon frequencies ω^2 are the eigenvalues of the dynamical matrix and are therefore directly related to the Hessian of the energetics (2.12). Accordingly, a positive value of ω^2 (real ω) produces a positive curvature of the energy surface meaning that the considered atomic positions correspond to a minimum of energy. In this case, the reference structure of interest is therefore stable. Conversely, if the reference structure is not stable (i.e. it is not the ground-state), there are atomic distortions that allow to decrease the energy and for which the energy curvature at the origin is negative. Such pattern of distortion therefore formally yields a negative value of ω^2 (imaginary ω) and corresponds to crystal instabilities. The atomic displacements pattern associated to such unstable mode is thus the one that is expected to bring the system to a lower energy configuration, as it produces a negative curvature in the energy of the reference structure. However, the determination of the optimal distorted structure is actually dependent on higher-order terms beyond the harmonic approximation. The fourth-order term in the distortion determines the gain of energy in the resulting double-well energy profile. Additionally, the coupling of the polar distortion to the strain must be considered to reproduce the ground-state correctly. For instance, if the strain accompanying the polar distortion is not taken into account in $PbTiO_3$, the resulting lower energy polar structure would be a rhombohedral phase with atomic displacements along the [111] direction instead of the correct tetragonal phase with displacements along the [001] direction [84, 93]. Such important role of polarization-strain coupling is also played in $CaTiO_3$ and $(Ba,Ca)TiO_3$ compounds analyzed in this thesis.

The computation of phonons frequencies in the reference structure of interest, for instance in the high-symmetry cubic phase of the ABO_3 perovskites, is therefore a powerful tool to

easily identify eventual structural instabilities.

2.3.2 Ferroelectric and Antiferrodistortive distortions

Referring to the simple cubic Brillouin zone (BZ) (Fig. 2.2), the most common instabilities occurring in the ABO_3 cubic perovskites are related to polar zone-center and non-polar zone-boundary distortions. The first ones usually result in ferroelectricity (FE) like in $BaTiO_3$, while the latters involve antiferrodistortive (AFD) distortions that preserve inversion symmetry, including in rotations and/or tilting of the oxygen octahedra and/or antiferroelectric (AFE) distortion like in $CaTiO_3$ and $CaZrO_3$. The coupling between different such modes produces additional distortions as allowed by symmetry consideration, like in the typical example of $BiFeO_3$ [76, 77, 78].

More in detail, the polar distortion is related to an unstable mode at the Γ point of the cubic BZ (Fig. 2.2), giving rise to a dipole moment in each unit cell. The corresponding irreducible representation (irrep) is Γ_4^- (notation refers to a system with origin at the B-site). If such distortion is described as a cooperative motion around the center of mass of the system taken as reference, it appears as an uniform displacements of cations against the oxygen octahedra, as illustrated in Fig. 2.5(a). The ferroelectric distortion usually helps to optimize the coordination environment of the B-site cation mostly to improve the B-O bonding, like in the case of $BaTiO_3$ and $KNbO_3$ [82]. However, the FE distortion can also optimize the A-site coordination environment if it involved a significant A-site component [81], like in the prototypical case of $PbTiO_3$ [83, 84] or $CaTiO_3$ and in solid solutions such as $K_{0.50}Li_{0.50}NbO_3$ [85] and $(Ba,Ca)TiO_3$. The latter analyzed in this thesis along with its parent compound $CaTiO_3$.

Differently, the non-polar antiferrodistortive distortions are related to unstable modes at the X, M and R points of the cubic BZ. In particular, distortions associated to oxygens rotations arise from specific instabilities at M and R, giving rise to tilting of the BO_6 octahedra relative to one another as rigid corner-linked units [80], as illustrated in Fig. 2.5(b,c). Such tilting produces greater flexibility in the coordination of the A cation, while leaving the environment of the B cation essentially unchanged [80]. In 1972, Glazer described such octahedral rotations in terms of component tilts around the pseudo-cubic axes: the rotation around one of these axes determines the rotation in the direction perpendicular to this axis, but successive octahedra along this axis can rotate in either the same or opposite sense [80], giving rise to the so-called "in-phase" and "out-of-phase" rotations respectively [Fig. 2.5(b,c)]. The associated irreps are M_3^+ and R_4^+ respectively (notation refers to a system with origin at the B-site). Specifically, "in-phase" rotations correspond to a phonon mode at the M point, while the "out-of-phase" rotations to that at R. The symbolic description of these tilted systems is known as Glazer's notation and it is of the type $a^\# b^\# c^\#$, in which each letter refers in turn to rotations around the [100], [010] and [001] direction of the pseudo-cubic reference. If the amplitude of the distortion is the same around different axes, the same letter is repeated. The superscript $\#$ can take the
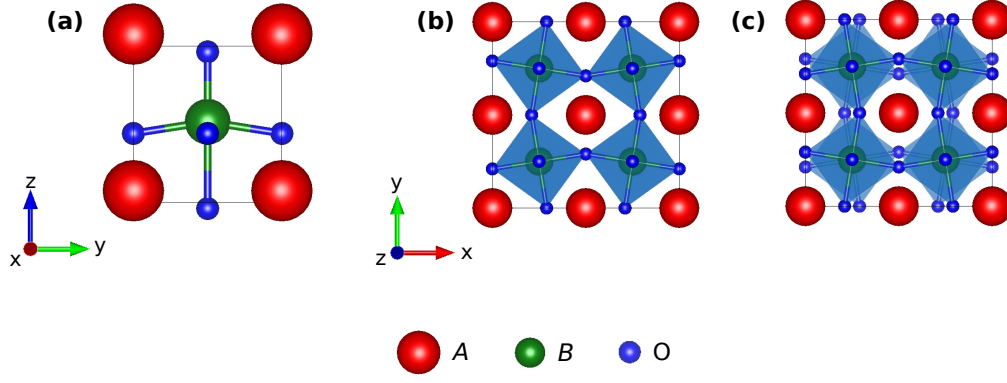
Figure 2.5: Schematic visualization of the two main distortions in the ABO_3 perovskites: (a) polar distortion arising from the Γ point of the cubic BZ consisting in the opposite motion of cations with respect to oxygens. (b) Antiferrodistortive distortion arising from the M point of the cubic BZ consisting in "in-phase" rotation of oxygen octahedra around the z pseudo-cubic axis ($a^0a^0c^+$ in the Glazer's notation [79]). (c) Antiferrodistortive distortion arising from the R point of the cubic BZ consisting in "out-of-phase" rotation of oxygen octahedra around the z pseudo-cubic axis ($a^0a^0c^-$ in the Glazer's notation [79]).
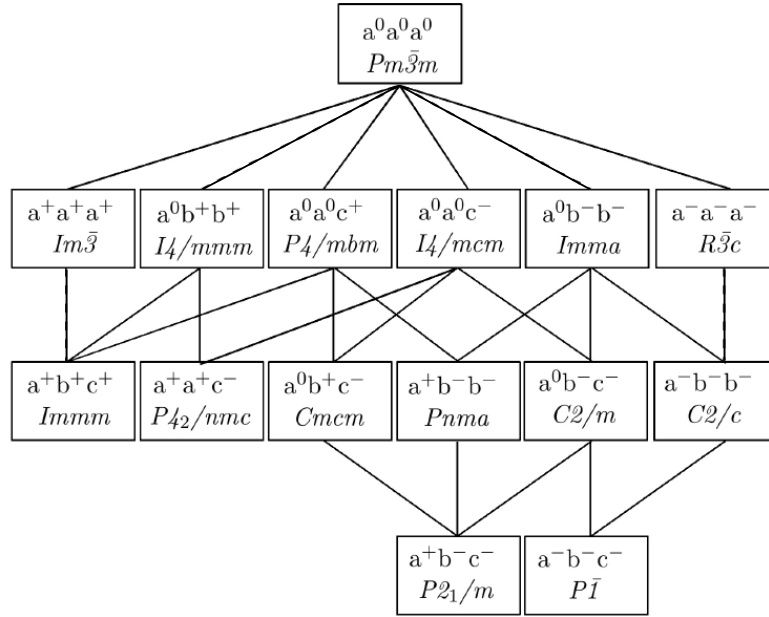
Figure 2.6: Schematic diagram indicating the group-subgroup relationships between 15 tilt systems. Adapted from Ref. [80].

value 0, + or − indicating no rotation or "in-phase" and "out-of-phase" rotations respectively. Accordingly, supposing only one "in-phase" rotation around the [001] direction the applied notation can be $a^0a^0c^+$, while if such rotation is "out-of-phase" the notation changes to $a^0a^0c^-$. According to the group-theoretical analysis presented in Ref. [80], through the linear combination of such rotations taken separately around each axis, 15 possible perovskite structures connected to the $Pm\bar{3}m$-cubic reference can be obtained (including the cubic reference itself). The diagram connecting the allowed subgroups to the $Pm\bar{3}m$-group is shown in Fig. 2.6.

A quite general remark is the seeming incompatibility between ferroelectricity and octahe-

dral rotations. Indeed, most ABO_3 perovskites with $t < 1$ crystallize in non-polar structures with octahedral rotations. The most common non-polar structure occurring is the $Pnma$. Nevertheless, these perovskites are unstable to both ferroelectric and octahedral rotation distortions in their cubic phase at $T = 0\ K$. As found out by Benedek and Fennie in Ref. [81], the suppression of ferroelectricity is generally due to the rotations themselves. However, in certain systems, like $CaTiO_3$ and $CaZrO_3$, the complementary A-site displacement is also necessary Moreover, in the specific case of $Pnma$, together with the M_3^+ and R_4^+ modes related to the two rotation patterns, the X_5^+ involving the A-site cation anti-polar displacement appears allowed by symmetry, although stable in the reference cubic phase . This mode only becomes energetically favorable when both M_3^+ and R_4^+ are present. Such behavior has been classified as "hybrid" improper-type [86, 87].

Hence, A-site displacements play an important role in the ferroelectric mechanisms of ABO_3 materials. Although $BaTiO_3$ is considered a prototypical example of ferroelectric compound as being B-site driven with $t > 1$, there is a very small number of perovskites with $t > 1$. Therefore, most perovskites not involving chemical mechanisms, such as second-order Jahn-Teller distortion or lone pair active cations, would be A-site driven geometric ferroelectrics, if their ferroelectric phases could be stabilized [81].

2.3.3 LO-TO splitting and Born effective charges

Following the initial picture of Cochran, nowadays, it is widely accepted that ferroelectricity in perovskites results from a delicate balance between short-range (SR) repulsions, which favor the cubic phase, and long-range (LR) electrostatic forces, which favor a ferroelectric state: a ferroelectric instability takes place when the Coulomb interaction is sufficiently large to compensate the short-range forces [61]. In fact, in ionic crystals and heteropolar semiconductors the crystal lattice can be described as composed of charged ions interacting both with short-range forces and long-range Coulomb forces. The associated dynamical matrix is obtained by direct summation of short-range terms and long-range Coulomb terms. Specifically, the interatomic force constants associated to the Coulomb interaction exhibit a dependence on the distance of the type $1/d^3$, which is typical of a classical dipole-dipole (DD) interaction [142].

Actually, the dynamical matrix for polar crystal has a "non-analyticity" for $q \to 0$, which is responsible of the transverse-longitudinal splitting of optical phonons. In fact, in ionic crystal, long-wavelength longitudinal (LO) and transverse (TO) optical modes exhibit different frequencies and interaction with the macroscopic electric field involving the creation of electric dipoles: in LO modes, the local field acts to reduce the polarization, producing an additional restoring force which produces a stiffening of the mode. Conversely, in TO modes, the local field acts to support the polarization producing the softening of the mode responsible for the ferroelectric state [61]. Accordingly, the so-called "proper" ferroelectrics, such as $BaTiO_3$, are characterized to exhibit a ferroelectric ground-state due to a polar distortion which lowers the

the energy of the nonpolar reference structure in zero macroscopic electric field, corresponding to the unstable transverse optical (TO) mode. In turn, the longitudinal optical (LO) modes are stable. Nevertheless, it is noteworthy to mention that a new class of ferroelectrics termed "hyperferroelectrics" has been recently discovered. This new class of proper ferroelectrics also exhibits the instability of a LO mode in addition to the TO mode instability, allowing the polarization to persist in the presence of a depolarizing field [98].

A fundamental quantity monitoring the LR Coulomb interaction is the Born dynamical effective charge $Z^*_{k,\alpha\beta}$, which is conventionally defined as the coefficient of proportionality at the linear order between the macroscopic polarization per unit cell created in direction β and the displacement of atoms k in direction α, times the unit cell volume Ω_0 [99]:

$$Z^*_{k,\alpha\beta} = \Omega_0 \frac{\partial P_\beta}{\partial \tau_{k,\alpha}} \tag{2.21}$$

In the cubic structure of the ABO_3 perovskites (Fig. 2.2), the Z^* tensors of the A and B atoms are isotropic, as they sit in centers of cubic symmetry. The O atoms are located at the face centers and the associated tensor thus has two inequivalent directions either parallel or perpendicular to the cubic phase. These two independent elements are then labelled as $O_\parallel$ and $O_\perp$ in reference to the change of polarization induced by an atomic displacement parallel or perpendicular to the B-O bonds [61].

A general feature in perovskite oxides is that the Born effective charges can deviate substantially from the value of the ionic atomic charge, revealing eventual mixed ionic and covalent character of bonds and producing large spontaneous polarization even for small distortions. Specifically, $Z^*(B)$ and $Z^*(O_\parallel)$ are anomalously large, while $Z^*(A)$ and $Z^*(O_\perp)$ are close to their nominal ionic value. Exceptions concern A-cations having an active lone-pair like $PbTiO_3$. Moreover, a strong correlation occurs between $Z^*(B)$ and $Z^*(O_\parallel)$ as well as $Z^*(A)$ and $Z^*(O_\perp)$, due to the fact that a displacement of the oxygen in the direction parallel to the B-O bond modulates the character of the bond itself, while a displacement in the perpendicular direction modulates the A-O bond [100]. Specifically, anomalous $Z^*(B)$ and $Z^*(O_\parallel)$ indicates that a strong dynamic charge transfer takes place along the B-O bond under atomic displacements. This is, in turn, related to the dynamical changes of hybridization between O $2p$ and B d states, which determines the highly covalent character of the B-O bond [99].

The Born effective charge tensor so reflects the Coulomb interaction effect and can quantify the LO-TO splitting. In fact, the interatomic force constant matrix can be separated into two parts: the first is the Fourier transform of the IFC matrix previously introduced, but for the specific case of $q = 0$, from which the interaction with the macroscopic the macroscopic electric field has been excluded; the second contribution is an additional term which treats the interaction with the eventual macroscopic field and can be expressed by means of the $Z^*_{k,\alpha\beta}$. It

is shown in Ref. [61] that the IFC matrix takes finally the form

$$\tilde{C}_{k\alpha,k'\beta}(\boldsymbol{q} \to 0) = \tilde{C}_{k\alpha,k'\beta}^{TO}(\boldsymbol{q} = 0) + \frac{4\pi}{\Omega_0} \frac{\sum_{\beta'}(Z_{k,\beta'\alpha}^{*}q_{\beta'})\sum_{\alpha'}(Z_{k,\alpha'\beta}^{*}q_{\alpha'})}{\sum_{\alpha'\beta'} q_{\alpha'}\epsilon_{\alpha'\beta}^{\infty}q_{\beta'}} \tag{2.22}$$

The difference between the LO and TO frequencies for an ionic crystal arises from the second term in Eq. (2.22) and generally there is no correspondence between individual TO and LO phonon modes.

A relevant quantity revealing the significant role of the soft TO mode in the ferroelectric state is the mode effective charge defined as [142]

$$\bar{Z}_{TO}^{*} = \left| \frac{\sum_{k,\beta} Z_{k,\alpha\beta}^{*}\eta_{k,\beta}^{TO}}{\sqrt{<\eta^{TO}|\eta^{TO}>}} \right| \tag{2.23}$$

The $\bar{Z}^{*}$ for the soft mode is usually the largest one, being originated essentially from the large Born effective charges. This means that the soft mode will couple most strongly with the electric field. This is the case for $BaTiO_3$, $CaTiO_3$ and $CaZrO_3$ reported in Table 5.6 in the results part. However, most compounds have a large $\bar{Z}^{*}$ for more than one modes. Therefore, these modes will be eventually mixed by the Coulomb interaction in determining the optimal ferroelectric state [100].

2.3.4 Interatomic Force Constants

Ferroelectricity is a collective phenomenon. In fact, an isolated atomic displacement in bulk cubic ABO_3 perovskite does not lower the energy of the system and thus does not produce a structural instability. When one atom is displaced, a restoring force is induced and brings it back in its initial position. However, this atomic displacement simultaneously induces forces on the other atoms. It is only the additional displacement of some other atoms in this force field that can lower the total energy of the reference structure and produce therefore the structural instability [61]. This feature can be understood in terms of the interatomic and "on-site" force constants defining the force associated to the atomic displacements. In Sec. 2.3.1, we have seen that the force $F_{k\alpha}^{a}$ along the direction α acting on atom k in cell a due to a displacement $\tau_{k'\beta}^{b}$ of atom k' in cell b is defined trough the IFC matrix $C_{k\alpha,k'\beta}$ in real space as

$$F_{k\alpha}^{a} = -C_{k\alpha,k'\beta}(a,b)\tau_{k'\beta}^{b} \tag{2.24}$$

For a pair of distinct atoms, the IFC can be interpreted as minus the harmonic spring constant between them, so that negative values correspond to stable interactions, while positive values imply destabilizing interatomic interaction. For the case of one single atom displacement, on the contrary, the "on-site" force constants cannot be directly interpreted as the harmonic spring constant. However, positive values correspond to stable interactions, while negative values to

destabilizing ones. In the specific case of most ABO_3 perovskites, the "on-site" force constants are all positive and, therefore, it is only the cooperative motion of different atoms that can decrease the energy of the crystal and generate an instability.

Moreover, the specific role of the dipole-dipole (DD) interaction can be separated from the one of the short-range (SR) forces, pointing out that ferroelectric instabilities are the results of destabilizing DD long-range interactions, sufficiently large to compensate the SR forces as previously discussed [188].

The analysis of the IFCs thus helps to identify the energetically favorable coupling in the displacements and elucidate the origin of the unstable phonon branches [102]. In this way, the access to the IFCs can be considered as an useful tool to identify at atomistic level the key mechanisms responsible for the final manifestation of macroscopic properties, resulting thus complementary to the Landau approach. In this regard, a systematic analysis and comparison of the dynamical properties is reported in the results part for the pure ABO_3 compounds and related solid solutions studied in this thesis.

2.4 Functional properties: the Dielectric and Piezoelectric response

The interest in ferroelectric oxides for technological applications is not only related to their switchable spontaneous polarization, but also to their polarization-related properties, such as large dielectric and piezoelectric responses. Such features can be directly related to the presence of low-frequency polar phonons, which dominate the properties, producing large lattice responses with high sensitivity to mechanical and electrical boundary conditions. In fact, certain responses can diverge near the phase boundary (i.e. around the phase transition temperature) as the corresponding soft-mode frequency goes to zero [92, 93].

2.4.1 Dielectric permittivity

For insulators, the static dielectric permittivity tensor is the coefficient of proportionality between the macroscopic displacement and electric fields in the linear regime [142], such as

$$D_{mac,\alpha} = \sum_{\beta} \epsilon_{\alpha\beta}\mathcal{E}_{mac,\beta} \tag{2.25}$$

In general, $\epsilon_{\alpha\beta}$ includes both electronic $\epsilon_{\alpha\beta}^{\infty}$ and ionic contributions taking the form [142]

$$\epsilon_{\alpha\beta} = \epsilon_{\alpha\beta}^{\infty} + \frac{4\pi}{\Omega_0}\sum_{m}\frac{S_{m,\alpha\beta}}{\omega_m^2} \tag{2.26}$$

where ω_m is the phonon-frequency of the mode m and $S_{m,\alpha\beta}$ is called mode-oscillator strength tensor and defined as [142]

$$S_{m,\alpha\beta} = \sum_{k\alpha'} Z^*_{k,\alpha\alpha'}\eta_{m\boldsymbol{q}=0}(k\alpha') \sum_{k'\beta} Z^*_{k',\beta\beta'}\eta_{m\boldsymbol{q}=0}(k'\beta') \tag{2.27}$$

with Z^* being the atomic Born effective charges and $\eta_{m\boldsymbol{q}=0}$ the eigendisplacement associated to the center-zone mode m. From 2.25 and 2.27, it is clear that compounds with TO modes combining a high polarity, measured via the coupling of the dynamical charges Z^* and TO modes eigendisplacements, i.e. $Z^*_{k,\alpha\alpha'}\eta_{m\boldsymbol{q}=0}$, and low frequency will exhibit a large dielectric response. As previously introduced via the notion of mode effective charge (2.23), in ABO_3 cubic perovskites, in fact, the soft mode is highly polar. In the ferroelectric phase, this gives rise to a highly polar mode of low frequency that can strongly couple with an electric field and be responsible for a huge dielectric coefficients. This is expressed, via the twice appearance of the dynamical charges in the dielectric response formula [92].

2.4.2 Piezoelectricity

As already seen in the introductory chapter, the piezoelectric effect is the manifestation of a linear coupling between electrical and mechanical fields [2]. When a piezoelectric material is subjected to external mechanical stress, electric charges generate at the surface. Nevertheless, despite its manifestation appears as surface effect, piezoelectricity is a bulk property [60]. The polarity associated to the created electric dipole depends on the direction of the applied stress, that is compressive or tensile. Such effect relying on the conversion of mechanical to electrical energy is the *direct piezoelectric effect*. The relationship between the induced electric polarization P^{ind} along the direction α and the applied stress σ is

$$P^{ind}_\alpha = d_{\alpha\beta}\sigma_\beta \tag{2.28}$$

where $d_{\alpha\beta}$ is the third-rank piezoelectric tensor [103], using the Voigt notation. Conversely, when the material is subjected to external electric field, it is strained. Depending on the direction of the electric field, the resulting strain can produce contraction or expansion of the material. This effect is the *indirect* or *converse piezoelectric effect*. The associated mathematical formulation is

$$\xi_\beta = d_{\alpha\beta}\mathcal{E}_\alpha \tag{2.29}$$

where ξ is the strain tensor and the piezoelectric coefficients $d_{\alpha\beta}$ are the same as those in Eq. 2.28 [103].

Two other equations are also used to link polarization to strain (in the direct effect) and

stress to the electric field (in the indirect effect). Specifically, these equations are:

$$P_\alpha^{ind} = e_{\alpha\beta}\xi_\beta \tag{2.30}$$

$$\sigma_\alpha = e_{\alpha\beta}\mathcal{E}_\beta \tag{2.31}$$

where $e_{\alpha\beta}$ are also elements of a third-rank tensor. However, the $e_{\alpha\beta}$ and $d_{\alpha\beta}$ have different units: $e_{\alpha\beta}$ is expressed in C/m^2, while $d_{\alpha\beta}$ in pC/N. These two parameters are related to each other via the elastic compliance [46].

Focusing on the $e_{\alpha\beta}$ piezoelectric coefficients (2.30), it can be decomposed into "clamped-ion" and "internal-strain" contributions as in the following [104]

$$e_{\alpha\beta} = \left.\frac{\partial P_\alpha^{ind}}{\partial \xi_\beta}\right|_\eta + \sum_k \left.\frac{\partial P_\alpha^{ind}}{\partial \eta_{k,\alpha}}\right|_\xi \frac{\partial \eta_{k,\alpha}}{\xi_\beta} \tag{2.32}$$

where the first term corresponds to the piezoelectric response where the ionic coordinates η stay unchanged and the second term to the one from the ionic displacements (the internal strain). The final explicit form highlighting the relationship with the phonon modes is then

$$e_{\alpha,\mu\nu} = e_{\alpha,\mu\nu}^0 - \frac{1}{\Omega_0} \sum_m \frac{\sum_{k,\beta} Z_{k,\alpha\beta}^* \eta_{k\beta}^m \sum_{k,\beta} g_{k\beta}^{\mu\nu} \eta_{k\beta}^m}{\omega_m^2} \tag{2.33}$$

where $g_{k\beta}^{\mu\nu}$ are parameters related to the internal strain coupling [92]. Similarly to the dielectric response, Eq. (2.33) shows that the ionic contribution to the piezoelectric response is large if the mode involved combines high polarity, via the $Z_{k,\alpha\beta}^* \eta_{k\beta}^m$ term, and low frequency, via the $1/\omega_m^2$ contribution. Additionally, it can be larger if that mode in the ferroelectric state exhibits strong coupling with strain, via the $g_{k\beta}^{\mu\nu} \eta_{k\beta}^m$ term.

Piezoelectricity being a property involving polar structures, all ferroelectric materials are also piezoelectrics. In particular, perovskite oxide ferroelectrics, which exhibit high sensitivity to changes in strain state, show highly-performing piezoelectric properties arousing big interest for technological applications. As a main result obtained by Fu and Cohen [52], high piezoelectric response in ferroelectric perovskites can be related to an easy rotation of polarization in presence of applied electric field. In particular, the existence of intermediate polar phases in the phase diagram, which link states with different orientations of the polarization and separated by low energy barrier, appears as an important feature for the material to exhibit an enhanced piezoelectric response.

A winning approach in optimizing and tuning the intrinsic piezoelectricity of the ABO_3 perovskite structure is the mixing of different parent oxides via atomic substitution of the A and/or B sites, leading to the formation of solid solutions of general formula $(A, A')(BB')O_3$. The most extensively studied and performing system at present is, in fact, the $Pb(Ti,Zr)O_3$ solid solution: the first parent compound, $PbTiO_3$, is ferroelectric with tetragonal phase, while the second one, $PbZrO_3$, exhibits an antiferroelectric (AFE) ground-state. However, the AFE

is destabilized by the partial atomic substitution of Zr by Ti atoms, favoring a rhombohedral phase for low concentration of Ti, and a tetragonal phase for higher Ti-concentration. At the phase boundary, where the two phases meet (which occurs around 50%), an enhancement of the piezoelectric response is observed. In fact, at that point in the phase diagram, an applied electric field can easily induce a transition between the rhombohedral and tetragonal phases going through monoclinic phases, with associated large strain response and rotation of polarization [48, 49, 105]. A similar mechanism concerns BCTZ, of interest here. In fact the end members in the compositional line of the phase diagram are $(Ba,Ca)TiO_3$ and $Ba(Ti,Zr)O_3$. In $(Ba,Ca)TiO_3$ the original rhombohedral ground-state of $BaTiO_3$ is destabilized by the partial atomic substitution of Ba by Ca, favoring a tetragonal phase, while $Ba(Ti,Zr)O_3$ preserves the rhombohedral ground-state for low Zr-concentration. At the proximity of the phase boundary line of the ferro-ferro transition an outstanding piezoelectric response has been, indeed, measured [44, 51, 106].

2.5   Conclusions

In this chapter we have had an excursus on the main features of bulk ABO_3 perovskites with a particular focus on the ferroelectric oxides. The aim was to provide all the necessary knowledge and explanation of the main physical properties investigated in the results part for a clear understanding of them. Necessary complementary explanations of the used method will be introduced in the next chapter.

From such an overview, we can summarize a global background like in the following: the perovskite structure adopted by this class of ABO_3 compounds exhibits the tendency to structural distortions in order to improve the bonding properties between the cations and oxygens. This behavior manifests in structural phase transitions as a function of temperature. Specifically, polar and/or antiferrodistortive distortions are the ones producing the energy lowering of the system with respect to the cubic reference structure, which is therefore unstable to such pattern of distortions.

The microscopic origin of such instabilities relies on a delicate balance between short-range and long-range interactions. In particular, most of these compounds are characterized by peculiar charge transfers when the atoms are displaced because of the usual mixed ionic-covalent character of their bonding, resulting in anomalous effective charges. Such behavior is responsible for the important Coulomb interaction, able to compensate the stabilizing short-range forces and to produce a structural ferroelectric instability.

The presence of an unstable phonon mode at the Γ point of the cubic Brillouin zone and the associated negative curvature at the origin of the adiabatic energy surface for a given pattern of polar atomic displacements are thus the fingerprint of the ferroelectric instability. Similarly, instabilities at the edge points of the cubic BZ to anti-polar atomic displacements and/or oxygens rotations are the fingerprint of the antiferrodistortive instabilities.

Directly related to this ground-state behavior of ferroelectrics is the softening of the polar mode with the temperature, which is responsible for the enhanced dielectric and piezoelectric responses of these compounds. Additionally, ABO_3 compounds allow it easily to tune and optimize such functional properties by means of chemical modifications of the parent ABO_3 system, such as via partial atomic substitutions at the A and/or B sites. Such kind of modifications of the physical properties when going from the parent ABO_3 compound to $(A, A')BO_3$ and $A(B, B')O_3$ solid solutions will be analyzed in detail in the results part.

Part II

Method

Chapter 3

Density Functional Theory: a general overview

In the previous chapter, we have seen that ABO_3 ferroelectric perovskites are characterized by complex mechanisms related to their specific structural and chemical properties leading to competing interactions, which manifest in various functional properties. Therefore, accurate and quantitative insight into such properties is essential for the understanding of the observed behavior and optimization of properties. In this respect, first-principles calculations based on *Density Functional Theory* (DFT) have yielded several breakthroughs in the understanding of the underlying physics in such a systems.

DFT is likely the most commonly used approach for the study of the electronic structure, as it determines the ground-state energy of the system by minimizing the one-body density functional. The electronic charge density plays the central role. It succeeds in describing structural and electronic properties for a wide class of materials. Additionally, complementary implementations, like the calculation of the polarization via the Berry phase formalism and the merging with the perturbation theory (DFPT), have expanded its range of application and success. Moreover, DFT is computationally efficient and well implemented in many different codes.

In the following we provide a general overwiev of DFT and related implementation used all along the present thesis.

3.1 Many-body Schrödinger equation and the adiabatic approximation

The peculiarity of density functional approach in its practical implementation is to rely on one-electron Schrödinger equation with a local effective potential in the study of the ground-state properties of the many-electron systems.

Considering a system of N electrons, the time-independent Schrödinger equation takes the

form

$$\hat{H}\Psi = E\Psi \tag{3.1}$$

where $\hat{H}$ is the Hamiltonian describing all the interactions of the system, E is the total energy of the system and Ψ is the many-body wave function, which depends on the position of each electron and each nucleus in the system. The full Hamiltonian for the system of electrons and nuclei can be expressed as

$$
\begin{aligned}
\hat{H} &= -\frac{\hbar^2}{2m_e}\sum_i \nabla_i^2 - \sum_I \frac{\hbar^2}{2M_I}\nabla_I^2 + \frac{1}{2}\sum_{i\neq j}\frac{e^2}{\mid \mathbf{r}_i - \mathbf{r}_j \mid} + \frac{1}{2}\sum_{I\neq J}\frac{Z_I Z_J e^2}{\mid \mathbf{R}_I - \mathbf{R}_J \mid} - \sum_{iI}\frac{Z_I e^2}{\mid \mathbf{r}_i - \mathbf{R}_I \mid} = \\
&= \hat{T}_e + \hat{T}_N + \hat{V}_{ee} + \hat{V}_{NN} + \hat{V}_{eN}
\end{aligned} \tag{3.2}
$$

where $\hat{T}_e$ and $\hat{T}_N$ refer to kinetic energies of electrons and nuclei respectively, and $\hat{V}_{ee}$, $\hat{V}_{NN}$, $\hat{V}_{eN}$ are the interaction potential terms; indices i, j and I, J refer to the electrons and to the nuclei respectively.

If we consider the mass of nuclei to be large in comparison to that of electrons, so that the inverse term $1/M_I$ can be regarded as "small", then the nuclear kinetic operator can be ignored in the total Hamiltonian (3.2) and the nuclei can be considered as fixed at the positions $\boldsymbol{R}$. Hereafter $\boldsymbol{R}$ is a shorthand notation indicating the set of nuclear coordinates $\{\boldsymbol{R}_I\}$. Similarly, the shorthand notation $\boldsymbol{r}$ indicates the set of electrons coordinates $\{\boldsymbol{r}_i\}$. This is the so-called *Born-Oppenheimer* or *adiabatic approximation*. Then, the kinetic energy of the nuclei can be used to determine the lattice dynamics in the *harmonic approximation*.

Within the adiabatic approximation, the so-called electronic adiabatic Hamiltonian, $\hat{H}_e(\mathbf{R};\mathbf{r})$, can be written as

$$\hat{H}_e(\mathbf{R};\mathbf{r}_1,\mathbf{r}_2,\ldots,\mathbf{r}_N) = \hat{T}_e + \hat{V}_{ee} + \hat{V}_{NN} + \hat{V}_{eN} = \hat{T}_e + \hat{V}(\mathbf{R};\mathbf{r}_1,\mathbf{r}_2,\ldots,\mathbf{r}_N) \tag{3.3}$$

where the variable $\mathbf{R}$ appears as parameter, rather than as a quantum dynamical observable.

The Schrödinger equation within the adiabatic approximation becomes

$$\hat{H}_e(\mathbf{R};\mathbf{r}_1,\mathbf{r}_2,\ldots,\mathbf{r}_N)\Psi_n(\mathbf{R};\mathbf{r}_1,\mathbf{r}_2,\ldots,\mathbf{r}_N) = E_n(\mathbf{R})\Psi_n(\mathbf{R};\mathbf{r}_1,\mathbf{r}_2,\ldots,\mathbf{r}_N) \tag{3.4}$$

where the electronic wave function $\Psi_n(\mathbf{R};\mathbf{r}_1,\mathbf{r}_2,\ldots,\mathbf{r}_N)$ and eigenvalues $E_n(\mathbf{R})$ depend on the parameter $\mathbf{R}$ and the subscript n summarizes the electronic quantum numbers. The eigenvalues $E_n(\mathbf{R})$ define the so-called *adiabatic potential-energy surface*.

In order to solve this many-body problem of electrons, that involves such a large number of particles and the difficult electron-electron interaction, further approximations must be applied.

3.2   The Hohenberg-Kohn theorem

Let's consider a system of N interacting electrons, without spin polarization for the moment. Starting from previous Eq. 3.3, it is convenient to decompose $\hat{H}_e$ into the sum of an "internal" and an "external" part, which refer to the kinetic energy of electrons plus the electron-electron interactions and the electronic-nuclear Coulomb interactions respectively. The nucleus-nucleus interaction $\hat{V}_{NN}$ can be ignored as it is not relevant for the description of the electrons problem. With rearrangement of notations, we have

$$\hat{H}_e = \hat{H}_{int} + \hat{V}_{ext} \tag{3.5}$$

where $\hat{H}_{int} = \hat{T}_e + \hat{V}_{ee}$ and $\hat{V}_{ext} = \hat{V}_{eN}$. $\hat{V}_{ext}$ is the only variable of such many-electrons problem. The Hohenberg-Kohn theorem state that *there is a one-to-one correspondence between the ground-state density of a N electron system and the external potential acting on it* [107]: the electronic density $n(\mathbf{r})$ in the ground-state is a functional of the external potential, $n[V(\mathbf{r})]$, and, conversely, the external potential is a unique functional of $n(\mathbf{r})$, $V[n(\mathbf{r})]$ [108]. The demonstration of this theorem presented in their seminal paper [108].

A straightforward consequence of the Hohenberg-Kohn theorem is that the ground-state energy is uniquely determined by the ground-state charge density, or, equivalently, the total energy of the system can be written as a functional of the density:

$$
\begin{aligned}
E[n(\mathbf{r}), \hat{V}_{ext}(\mathbf{r})] &= T[n(\mathbf{r})] + \hat{V}_{ee}[n(\mathbf{r})] + \int d\mathbf{r}\ n(\mathbf{r})\hat{V}_{ext}(\mathbf{r}) = \\
&= F[n(\mathbf{r})] + \int d\mathbf{r}\ n(\mathbf{r})\hat{V}_{ext}(\mathbf{r})
\end{aligned}
\tag{3.6}
$$

where $F[n(\mathbf{r})]$ is a universal functional of $n(\mathbf{r})$ containing the kinetic energy and the electron-electron interactions, i.e. it does not depend on $\hat{V}_{ext}$. By applying the variational principle to the energy functional (3.6), it result that the ground-state energy is minimized by the ground-state charge density, and its minimum gives the *exact ground-state energy* of the many-body electron system.

In this way, DFT exactly reduces the N interacting particles problem to the determination of a function $n(\mathbf{r})$ of three-coordinates. However, some approximations are required to estimate the unknown functional $F[n(\mathbf{r})]$.

3.3   The Kohn-Sham equations and the Effective one-electron potential

In 1965 Kohn and Sham [109] developed an approximation scheme to exploit the Hohenberg-Kohn theorem by including exchange and correlation effects. They proposed to replace the

many-body electron problem by an alternative fictitious independent-particles problem. The concept is to map the system of interacting particles into a set of fictitious particles moving in an effective potential, with the same ground-state electronic density.

Within this framework, the density of the system is defined by the one-electron wave function $\psi_i(\boldsymbol{r})$ as

$$n(\mathbf{r}) = \sum_i^{occ} |\psi_i(\mathbf{r})|^2 \tag{3.7}$$

The total electronic energy in term of the density $n(\mathbf{r})$ is written

$$E[n] = \int d\mathbf{r} \ n(\mathbf{r})\hat{V}_{ext}(\mathbf{r}) + \frac{e^2}{2} \int \int d\mathbf{r}d\mathbf{r}' \ \frac{n(\mathbf{r})n(\mathbf{r}')}{|\mathbf{r}-\mathbf{r}'|} + T_s[n] + E_{xc}[n] \tag{3.8}$$

where the first integral represents the interaction between the electrons and the fixed ions, the second integral term represents the Coulomb interaction energy of an electronic cloud of density $n(\mathbf{r})$ (Hartree energy $E_{Hartree}[n]$), T_s represents the kinetic energy of the non-interacting electrons and E_{xc} is the exchange and correlation energy, that contains all the electron-electron interaction going beyond the classical Coulomb interaction.

For a given set of atomic positions, the ground-state is determined via the minimization of Eq. (3.8) under the orthonormalization constraints

$$< \psi_i|\psi_j >= \delta_{ij} \tag{3.9}$$

This provides the total energy of the system and the associated electronic density.

In practice, the variational calculation of the functional (3.8) with respect to $n(\mathbf{r})$ leads to the single-particle Schrödinger-like equation of the type

$$\left[-\frac{\hbar^2\nabla^2}{2m_e} + \hat{V}_{eff}(\mathbf{r}) \right] \psi_i(\mathbf{r}) = \epsilon_i\psi_i(\mathbf{r}) \tag{3.10}$$

where ϵ_i and $\Psi_i(\mathbf{r})$ are the so-called Kohn-Sham eigenvalues and eigenfunctions respectively. $\hat{V}_{eff}$ is the effective one-electron potential, also called *self-consistent potential* [141], associated to the Hohenberg-Kohn ground-state charge density of the interacting many particles potential:

$$\hat{V}_{eff}(\mathbf{r}) = e^2 \int d\mathbf{r}' \ \frac{n(\mathbf{r}')}{|\mathbf{r}-\mathbf{r}'|} + \hat{V}_{eN}(\mathbf{r}) + \hat{V}_{xc}(\mathbf{r}) \tag{3.11}$$

where the extra term $\hat{V}_{xc}(\mathbf{r})$ is called *exchange-correlation potential* and is given by the functional derivate

$$\hat{V}_{xc}(\mathbf{r}) = \frac{\partial E_{xc}[n]}{\partial n(\mathbf{r})} \tag{3.12}$$

Equations (3.10), (3.11), (3.7) have to be solved in a self-consistent way: one starts by guessing a certain $n(\mathbf{r})$ in order to construct $\hat{V}_{eff}(\mathbf{r})$, and then finds a new $n(\mathbf{r})$ from (3.10)

and (3.7). The initial and final density are then mixed by means of appropriate converging schemes, until self-consistency is reached (i.e. when the initial and final densities are different by less than a certain threshold).

Once the Kohn-Sham orbitals and energies have been determined, the exact total ground-state energy (3.8) of the interacting electronic system can be written as

$$E_0[n] = \sum_i^{occ} \epsilon_i - \int d\mathbf{r} \ n(\mathbf{r})\hat{V}_{xc}(\mathbf{r}) - E_{Hartee}[n] + E_{xc}[n] \tag{3.13}$$

The Kohn-Sham equations are standard differential equations with a local effective potential $\hat{V}_{eff}(\mathbf{r})$. Any difficulty in the resolution has been confined to the choice of a reasonable exchange-correlation functional $E_{xc}[n]$. Conceptually, the Kohn-Sham equations determine the electron density and the ground-state energy. However, the eigenvalues ϵ_i in (3.10) are formal Lagrange multipliers within the *variational principle* and don't have any physical meaning. The identification of ϵ_i with occupied and unoccupied one-electron states is however often performed and empirically found to give a good results in many cases for the occupied states. On the contrary, as DFT is a ground-state theory, the description of excited states is rather poor. Indeed, on the one hand, the general result of DFT calculations is to underestimate the energy band gap in semiconductors and insulators, independently on the exchange-correlation functional $\hat{V}_{ex}$ used in (3.11). On the other hand, the dispersion curves of valence and conduction bands are described with good accuracy in many cases. However, the accuracy and capability of DFT vary strictly as a function of the investigated physical system.

3.4 Approximations for the Exchange-Correlation energy

3.4.1 LDA

The crucial quantity in the Kohn-Sham approach is the exchange-correlation energy $E_{xc}[n]$, which is expressed as a functional of the density. Even though the exact definition of the functional $E_{xc}[n]$ is very complex, the first suggestion came from Kohn and Sham themselves [109]. Their *ansatz* was that the exchange-correlation $E_{xc}[n]$ can be reasonably approximated as a local or nearly local functional of the density. They proposed the so-called *local density approximation*, better known as LDA, which is particularly justified in systems with reasonably slowly varying spatial density $n(\mathbf{r})$. They approximated the functional $E_{xc}[n]$ with a function of the local density $n(\mathbf{r})$ writing down

$$E_{xc}^{LDA}[n] = \int d\mathbf{r} \ n(\mathbf{r})\epsilon_{xc}(n(\mathbf{r})) \tag{3.14}$$

where $\epsilon_{xc}(n(\mathbf{r}))$ is the exchange-correlation energy per particle for a homogeneous electron gas with density n at the point $\mathbf{r}$. The *exchange* part can be obtained analytically from the Hartree-Fock technique and it scales like [109]

$$\epsilon_x = -\frac{3}{4}e^2(3\pi^2)^{1/3}[n(\mathbf{r})]^{1/3} \tag{3.15}$$

The expression of *correlation* energy has been estimated by means of different numerical parametrizations [110, 109, 111, 112, 113, 114, 115], all of which lead to very similar total-energy results [116].

As mentioned before, the LDA appears to give a well defined global minimum for the energy of a non-spin-polarized system of electrons in a fixed ionic potential. Therefore, subsequent works reformulated density functional theory in the local density approximation for spin dependent systems, [117, 118]. Such extension is known as *Local Spin Density Approximation* (LSDA). Traditional DFT is based on two fundamental theorems, according to which the ground-state wave function is a unique functional of the electronic charge density and the ground-state energy functional is stationary with respect to variations in the charge density. LSDA formalism can include all these results in spin dependent cases by replacing the scalar effective one-electron potential $\hat{V}_{eff}$ in equation (3.11) with the spin dependent effective single-particle potential

$$\hat{V}_\sigma^{eff}(\mathbf{r}) = e^2 \int d\mathbf{r}' \frac{n(\mathbf{r}')}{|\mathbf{r} - \mathbf{r}'|} + \hat{V}_{eN}(\mathbf{r}) + \hat{V}_\sigma^{xc}(\mathbf{r}) \tag{3.16}$$

Here, the charge density $n(\mathbf{r})$ is intended as the sum of spin densities $n_\uparrow(\mathbf{r})$ and $n_\downarrow(\mathbf{r})$ with

$$n_\sigma(\mathbf{r}) = \sum_{i,\sigma}^{occ} |\Psi_{i,\sigma}(\mathbf{r})|^2 \tag{3.17}$$

where $\Psi_{i,\sigma}(\mathbf{r})$ are the spin dependent Kohn-Sham one electron orbitals and the sum runs over all occupied states with spin σ. To obtain a reasonable approximation for $\hat{V}_\sigma^{eff}(\mathbf{r})$, the external potential $\hat{V}_{eN}(\mathbf{r})$ is considered as slowly varying and the electronic system dived into small boxes. Within the box centered at $\mathbf{r}$, the electrons can be considered to form a spin polarized homogeneous electron gas of local density $n(\mathbf{r})$ and the spin dependent exchange-correlation potential is given by

$$\hat{V}_\sigma^{xc}(\mathbf{r}) = \frac{\partial(n(\mathbf{r})\epsilon_{xc}(n_\uparrow, n_\downarrow))}{\partial n_\sigma(\mathbf{r})} \tag{3.18}$$

Accordingly, the exchange-correlation energy functional can be still written in the following form

$$E_{xc}^{LSDA}[n_\uparrow, n_\downarrow] = \int d\mathbf{r}\, n(\mathbf{r})\epsilon_{xc}(n_\uparrow(\mathbf{r}), n_\downarrow(\mathbf{r})) \tag{3.19}$$

For weakly correlated materials, such as semiconductors and simple metals, the LDA accurately describes structural and dynamical properties: the correct structure is usually found

to have the lowest energy, while bond lengths, bulk moduli, and phonon frequencies are accurate to within a few percent [119]. However, such accuracy appears in some cases as a serious limitation. In perovoskite oxides, for instance, the ferroelectric instability is very sensitive to pressure, and thus to the structural parameters. Additionally, LDA tends to underestimate energy band gap in semiconductors and insulators by about 40% [120], and to overestimate cohesive energies and bond strengths. The latter and its inability to properly describe strongly correlated systems are the LDA biggest limitations. Therefore, gradient corrections to the LDA have been developed.

3.4.2   GGA

There have been several attempts to construct improved functionals in order to go beyond the local density approximation. A first alternative, but connected approach, have been the *Generalized-gradient approximations*, better known as GGAs. The physical ideas that are the basis for the construction of GGAs is to build a "semi-local" functional depending both on the density at r and on its gradient. Accordingly, starting from the LSD approximation, the exchange-correlation functional $E_{xc}[n]$ within GGAs is approximated by the form [121, 122, 123]

$$E_{xc}^{GGA}[n_\uparrow, n_\downarrow] = \int d\mathbf{r} \ f(n_\uparrow, n_\downarrow, \nabla n_\uparrow, \nabla n_\downarrow) \tag{3.20}$$

where f is a parametrized analytic functions.

GGAs usually improve the accuracy of the local spin-density (LSD) approximation in electronic structure calculations, namely provide a better description of total energies, cohesive energies, energy barriers and structural properties by correcting bond strengths and lengths with respect the basic local density functionals. Different derivations and formal properties of various GGAs have been developed. For detailed descriptions of different GGA and meta-GGA functionals refer to Refs. [121],[124]-[130]. Among them, the most known and used is the one designed by Perdew, Burke and Ernzerhof in 1996, the so-called PBE functional, in which all parameters improving the LSD approximation are fundamental constants. Derivation and properties of such functional are presented in their famous paper [122]. The general form for the PBE exchange-correlation functional including nonlocality is

$$E_{xc}^{GGA_{PBE}}[n_\uparrow, n_\downarrow] = \int d\mathbf{r} \ n\epsilon_x^{unif}(n)F_{xc}(r_s, \zeta, s) \tag{3.21}$$

where n is the electron density, ϵ_x^{unif} is the exchange energy of a uniform electron gas (3.15) and $F_{xc}(r_s, \zeta, s)$ is the enhancement factor over local exchange [121], with r_s the local Seitz radius ($n = 3/4\pi r_s^3$), $\zeta = (n_\uparrow - n_\downarrow)/n$ the relative spin polarization and $s = |\nabla n|/[2(3\pi^2)^{1/3}n^{4/3}]$ a dimensionless density gradient [122].

However, cases in which GGAs, and so the PBE, overcorrect LSD predictions, such as lattice constants, could occur [131]. As for the previous case of LDA, such inaccuracy can be dramatic

especially for ferroelectrics which are extremely sensitive to volume. The worst results concern volume and strain of relaxed tetragonal $PbTiO_3$ [132]. A considerable improvement for solid systems has been achieved via the so-called "WC" functional constructed by Wu and Cohen in 2006. Using the PBE correlation functional, they reformulated the exchange part of the PBE enhancement factor (3.21) relying on the fact that solid systems usually have valence electron density varying more slowly than electron densities of atoms and molecules. In their work [133], they show that WC predicts highly accurate volumes, strains, and atomic displacements, whereas LSD and PBE underestimate and overestimate these values, respectively. In particular, the recovered agreement with experiments for the case of $PbTiO_3$ is surprising. Moreover, they also show results for relaxed rhombohedral $BaTiO_3$.

According to the high capability in reproducing properties of ferroelectric materials, we used therefore the GGA-based WC functional for all our calculations.

3.5 Practical Implementation

Despite the *Adiabatic Approximation* and the *Density Functional Theory* reduces the many-body problem to an equivalent effective single-electron problem in frozen-in configurations of nuclei, there still remains the task of treating a huge number of non-interacting electrons within the static potential of a huge number of nuclei. Two associated difficulties thus arise: a wave function should be calculated for each electron; since each electronic wave function extends over the entire solid, the basis set required to expand each wave function is infinite [116]. Such difficulties are overcome in periodic systems, like the ones of interest here, satisfying the Bloch's theorem.

The ABINIT package

Various first-principles based on DFT have been implemented in different codes and softwares. The one used to obtain all the results in this thesis is ABINIT, a package whose main program allows to calculate the ground-state total energy, charge density and electronic structure of electrons-ions systems within Density Functional Theory, using pseudopotentials (or PAW atomic data) and a plane waves basis. Additionally, ABINIT also allows to perform optimization of the geometry according to the definition of forces and stresses in the DFT; implementation for molecular dynamics simulations are also available. Moreover, thanks to an advanced implementation of the Density Functional Perturbation Theory DFPT, it is possible to calculate phonons at every point within the Brillouin zone of the analysed structure as well as to calculate Born effective charges, dielectric tensors, piezoelectric tensors, polarization. The latter quantity is attainable with the implementation of the Berry phase theory. Many other properties are achievable by means of other developments. In addition to the main ABINIT code, different utility programs for post-processing treatment of data are provided. Detailed descriptions can

be found in Refs. [156, 157, 158, 159].

In the following basic descriptions of some practical implementations for the usage of DFT as well as of DFPT as exploited by ABINIT are provided.

3.5.1   Bloch's Theorem and Plane wave basis set

For infinite periodic solids obtained by imposing periodic boundary conditions, the electronic wave functions $\psi_{n,\boldsymbol{k}}(\boldsymbol{r})$ can be related to the product of a plane wave function of wave vector $\boldsymbol{k}$ and a cell periodic function $u_{n,\boldsymbol{k}}(\boldsymbol{r})$

$$\psi_{n,\boldsymbol{k}}(\boldsymbol{r}) = \frac{1}{\sqrt{N\Omega_0}} e^{i\boldsymbol{k}\cdot\boldsymbol{r}} u_{n,\boldsymbol{k}}(\boldsymbol{r}) \tag{3.22}$$

where N is the number of unit cells repeated in the Born-von Karman periodic box, and Ω_0 is the volume of the unit cell. Specifically, $u_{n,\boldsymbol{k}}(\boldsymbol{r})$ satisfies the lattice periodicity condition: $u_{n,\boldsymbol{k}}(\boldsymbol{r}) = u_{n,\boldsymbol{k}}(\boldsymbol{r}+\boldsymbol{R})$ for any $\boldsymbol{R}$ belonging to the Bravais lattice. As a consequence, $u_{n,\boldsymbol{k}}(\boldsymbol{r})$ can be expanded in terms of a discrete set of plane waves whose wave vectors $\boldsymbol{G}$ are vectors belonging to the reciprocal lattice of the crystal and defined by $\mathbf{G}\cdot\mathbf{R} = 2\pi m$ with m integer (i.e. discrete Fourier transform). The electronic wave function thus can be expanded as

$$\psi_{n,\boldsymbol{k}}(\boldsymbol{r}) = \frac{1}{\sqrt{N\Omega_0}} \sum_{\boldsymbol{G}} c_{n,\boldsymbol{k}}(\boldsymbol{G}) e^{i(\mathbf{k}+\mathbf{G})\cdot\mathbf{r}} \tag{3.23}$$

An infinite plane wave basis set is required to expand $\psi_{n,\boldsymbol{k}}(\boldsymbol{r})$. However, in practical calculations, the expansion can be truncated to include only plane waves that have a kinetic energy smaller that a chosen "cut-off energy", namely $\frac{\hbar^2}{2m}|(\mathbf{k}+\mathbf{G})|^2 \leq E_{cut}$. Such truncation introduces a computational error. However, the amplitude of such error can be reduced by increasing the value of E_{cut} until the calculated total energy reaches a chosen convergence.

Similarly, the accuracy of calculations also rely on the sampling of the Brillouin zone as the use of the Bloch functions is associated with integration over the periodic $\boldsymbol{k}$-space. In principle, electronic wave functions for an infinite number of $\boldsymbol{k}$ points should be calculated However, electronic wave functions at $\boldsymbol{k}$ points that are close to each other are mostly identical, so that it possible to represent $\psi_{n,\boldsymbol{k}}(\boldsymbol{r})$ over a region of $\boldsymbol{k}$ space by that at a single $\boldsymbol{k}$ point. In such a way calculations are performed for a finite number of $\boldsymbol{k}$ points [116]. As a consequence, different sampling methods have been developed among which the so-called "Monkhorst-Pack" is the most used [134, 135, 136]. Of course, the total energy will converge as the density of the $\boldsymbol{k}$ points increases, and the error due to such sampling then approached zero, like in the case of the cuff-energy for the plane waves basis set expansion. Therefore, specific convergence tests on the $\boldsymbol{k}$ point sampling and E_{cut} have to be performed for any compound of interest.

3.5.2   Pseudopotential approximation
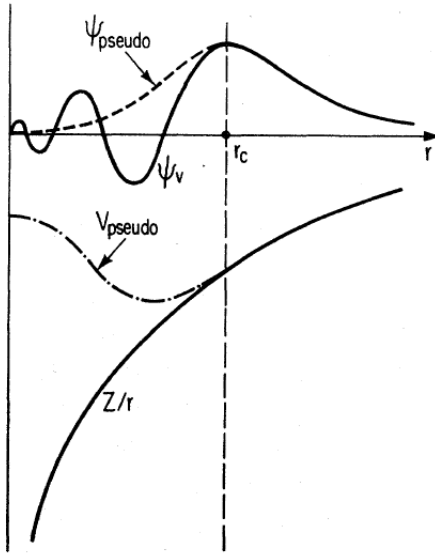
Figure 3.1: Schematic illustration of all-electron (solid lines) and pseudoelectron (dashed lines) potentials and their corresponding wave functions. The radius at which all-electrons and pseudopotential values match is designated r_c. From Ref. [116].

Despite the computational advantages associated to the plane waves basis, two major difficulties, one related to the description of tightly bounded core states and the other to the rapid oscillations of the wave functions of the valence electrons in the core region, have required the development of a joint approximation: the pseudopotential.

At the basis of such approximation, there is a first observation referred as "frozen-core" approximation, according to which the physical and chemical properties of solids are usually essentially dependent on the valence electrons, while the core electrons, which do not participate to the chemical bonding, are only slightly affected by the atomic environment. The pseudopotential approximation exploits this by removing the core electrons and by replacing them and the strong ionic potential by a fictitious potential acting on valence electrons only such that the valence wave functions remain unchanged beyond a given cutoff radius r_c and are replaced by smoothly varying function inside the core region [116, 61], as illustrated in Fig. (3.1). In practice, in order to further validate the frozen-core and pseudopotential approximations, electrons from deep energy levels can be treated as valence electrons. This is what has been done for the study of $BaTiO_3$, $CaTiO_3$, $CaZrO_3$, and $BaZrO_3$ (see Sec. 4).

As seen before, the total energy of the electronic system is a function of the electron density (3.7). Therefore, it is necessary that outside the core region the pseudo wave functions and real wave functions are identical both in their spatial dependences and in their absolute magnitudes, so that the two wave functions generate identical charge densities. Pseudopotentials preserving the charge are termed *norm conserving*. A list of references related to different pseudopotential developments can be found in the review of Payne *et al.* [116].

The typical method for generating an ionic pseudopotential is to perform at first all-electron calculations for an isolated atom and then, an analytical pseudopotential is fitted in order to reproduce the real potential and wave functions outside the cutoff radius. It is then expected that such potential is *transferable* to the solid systems, within which the frozen-core approximation remains valid. The most general form for a pseudopotential is

$$V_{ps} = \sum_{lm} |lm > V_l < lm| \tag{3.24}$$

where $|lm >$ are the spherical harmonics and V_l is the pseudopotential for angular momentum l [116]. V_{ps} using the same potential for all the angular momentum is called *local* pseudopotential,

while angular momentum dependent V_{ps} is called *nonlocal* pseudopotential. The "Optimized Norm-Conserving" pseudopotentials [137] used for the calculations in this work belong to the nonlocal type.

VCA

The application of first-principles calculations to the study of disordered alloys and solid solutions generally requires the use of the supercell approximation, namely to study one or more atomic configurations in large cells with imposed periodic boundary conditions within the framework of Bloch's theorem. Such calculations, however, tend to be computationally very demanding. In this respect, a less expensive approach has been developed to treat such complex systems, that is the virtual crystal approximation (VCA). Within this approximation, one studies a crystal with the primitive periodicity, but composed of "fictitious virtual" atoms that interpolate between the behavior of the real atoms occupying alternatively the same site [138]. By its nature, VCA is closely related to the pseudopotential approximation. In its general formulation, the VCA operator equation for any type of pseudopotential is formally defined by averaging the pseudopotentials of the combined homovalent elements, i.e. $C_{1-x}D_x$, on a specific atomic site I as [138, 139]

$$V_{ps}^I[x] = (1 - x)V_{ps}^C + xV_{ps}^D \tag{3.25}$$

where V_{ps}^C and V_{ps}^D are the pseudopotentials of the combined C and D atoms and x the mixing concentration at the site I.

Pioneering works [138, 139, 140] have demonstrated good accuracy for the VCA in some ferroelectric perovskite solid solutions, such as $Pb(Zr_{0.50}Ti_{0.50})O_3$ and $Ba_xSr_{1-x}TiO_3$. Relying on these observations, we performed first-principles calculations using the VCA on the solid solutions of interest in this thesis, such as $(Ba,Ca)TiO_3$ and $Ba(Ti,Zr)O_3$. However, the comparison with complementary calculations based on the use of supercells and available experiments have revealed severe limits to the applicability of the VCA for these systems. Detailed results and explanations will be provided in specific sections of the results part.

3.6 Merging DFT and Perturbation Theory

As seen so far, many of the properties of interest in crystalline solids are related to the derivative of the total energy $E(\boldsymbol{R})$ with respect to adiabatic perturbations (mainly atomic displacements, electric field and strain) around the equilibrium configuration. Within DFT, the simplest method is a direct approach, called *finite differences*, in which a finite amplitude perturbation is frozen into the system and the perturbed system is then compared to the unperturbed one. Despite being rather straightforward computationally, such approach suffers from limitations mostly related to incommensurability of some perturbations with the periodic lattice and limited size used cells [141, 142, 143]. The merging of the perturbation theory and DFT, instead, has

brought several advantages in the description and treatment of perturbations. Such a method, known as *density functional perturbation theory* (DFPT) had been first reported by Baroni, Giannozzi, and Testa [141] for linear response to atomic displacements and then generalized to other perturbations [144, 145, 146, 147]. A different algorithm, based on a variational principle, has been then proposed by Gonze *et al*, generalizing previous formulations by making use of the *2n+1* theorem [148, 149, 150].

3.6.1 Perturbative development

Within the perturbation theory, the basic idea is that all quantities X ($X = H, E_n, \psi_n(\boldsymbol{r}), n(\boldsymbol{r}), etc.$) can be expanded in terms of a small external perturbation λ around the unperturbed state $X^{(0)}$, as follow [149, 150]

$$X(\lambda) = X^{(0)} + \lambda X^{(1)} + \lambda^2 X^{(2)} + \lambda^3 X^{(3)} + \dots \tag{3.26}$$

where

$$X^{(n)} = \frac{1}{n!} \frac{d^n X}{d\lambda^n} \Big|_{\lambda=0} \tag{3.27}$$

Focusing on the change in the unperturbed Hamiltonian of the system $H^{(0)}$ due to an external perturbative potential, namely $H(\lambda) = H^{(0)} + V_{ext}(\lambda)$, the perturbed Schödinger equation to be solved takes the form

$$H(\lambda) \, |\psi_n(\lambda)\rangle = E_n(\lambda) \, |\psi_n(\lambda)\rangle \quad \forall \lambda \tag{3.28}$$

with the normalization condition

$$\langle \psi_n(\lambda) | \psi_m(\lambda) \rangle = \delta_{nm} \tag{3.29}$$

Inserting in Eq. (3.28) the expansion (3.26) as a function of λ, i.e.

$$
\begin{aligned}
H(\lambda) &= H^{(0)} + \lambda H^{(1)} + \lambda^2 H^{(2)} + \lambda^3 H^{(3)} + \dots \\
|\psi_n(\lambda)\rangle &= |\psi_n^{(0)}\rangle + \lambda \, |\psi_n^{(1)}\rangle + \lambda^2 \, |\psi_n^{(2)}\rangle + \lambda^3 \, |\psi_n^{(3)}\rangle + \dots \\
E_n(\lambda) &= E_n^{(0)} + \lambda E_n^{(1)} + \lambda^2 E_n^{(2)} + \lambda^3 E_n^{(3)} + \dots
\end{aligned}
$$

and grouping terms with the same power of λ result in a set of equations of the type

$$
\begin{aligned}
&\text{for } \lambda^0 & H^{(0)} \, |\psi_n^{(0)}\rangle &= E_n^{(0)} \, |\psi_n^{(0)}\rangle \\
&\text{for } \lambda^1 & H^{(0)} \, |\psi_n^{(1)}\rangle + H^{(1)} \, |\psi_n^{(0)}\rangle &= E_n^{(0)} \, |\psi_n^{(1)}\rangle + E_n^{(1)} \, |\psi_n^{(0)}\rangle \\
&\text{for } \lambda^2 & H^{(0)} \, |\psi_n^{(2)}\rangle + H^{(1)} \, |\psi_n^{(1)}\rangle + H^{(2)} \, |\psi_n^{(0)}\rangle &= E_n^{(0)} \, |\psi_n^{(2)}\rangle + E_n^{(1)} \, |\psi_n^{(1)}\rangle + E_n^{(2)} \, |\psi_n^{(0)}\rangle
\end{aligned}
$$

$$\dots$$

Similarly, introducing the perturbative expansion of $|\psi_n(\lambda)\rangle$ in the normalization condi-

tion (3.29), the orthonormality relationships for the perturbed wave functions are

$$
\begin{aligned}
&\text{for } \lambda^0 & \langle \psi_n^{(0)} | \psi_n^{(0)} \rangle &= 1 \\
&\text{for } \lambda^1 & \langle \psi_n^{(0)} | \psi_n^{(1)} \rangle + \langle \psi_n^{(1)} | \psi_n^{(0)} \rangle &= 0 \\
&\text{for } \lambda^2 \quad \langle \psi_n^{(0)} | \psi_n^{(2)} \rangle + \langle \psi_n^{(1)} | \psi_n^{(1)} \rangle + \langle \psi_n^{(2)} | \psi_n^{(0)} \rangle &= 0
\end{aligned}
$$

$$\cdots$$

Previous expansions for the Schödinger equation and normalization condition then become, at generic order i [148]

$$i \sum_{j=0}^{i} (H - E_n)^{(j)} | \psi_n^{(i-j)} \rangle = 0 \tag{3.30}$$

$$\sum_{j=0}^{i} \langle \psi_n^{(j)} | \psi_n^{(i-j)} \rangle = 0, \quad i \neq 0 \tag{3.31}$$

In order to determine i^{th}-order correction to the energies, it is necessary to project on $\langle \psi_n^{(0)} |$ the Schödinger equation of the ith-order of interest and to make use of the associated relationships between the perturbed wave functions obtained from the normalization condition. Moreover, it is worthy remembering that the Hamiltonian is Hermitian. Proceeding, for instance, for the first- and second-order derivatives, we obtain

$$
\begin{aligned}
E_n^{(1)} &= \langle \psi_n^{(0)} | H^{(1)} | \psi_n^{(0)} \rangle \\
E_n^{(2)} &= \langle \psi_n^{(0)} | H^{(2)} | \psi_n^{(0)} \rangle + \langle \psi_n^{(0)} | H^{(1)} - E_n^{(1)} | \psi_n^{(0)} \rangle
\end{aligned}
$$

Therefore, it results that to obtain the 1st-order correction to the energy, only the knowledge of the 0th-order wave function is required; to obtain the 2st-order correction to the energy, the 0th- and 1st-order wave functions are required.

Alternatively, it is possible to develop as a function of λ the following equation

$$\langle \psi_n(\lambda) | H(\lambda) - E_n(\lambda) | \psi_n(\lambda) \rangle = 0 \quad \forall \lambda \tag{3.32}$$

Developing (3.32) up to the second-order perturbative expansion, another expression for $E_n^{(2)}$ is obtained, that is

$$
\begin{aligned}
E_n^{(2)} = &\langle \psi_n^{(0)} | H^{(2)} | \psi_n^{(0)} \rangle + \langle \psi_n^{(1)} | H^{(0)} - E_n^{(0)} | \psi_n^{(1)} \rangle + \\
&+ \langle \psi_n^{(0)} | H^{(1)} - E_n^{(1)} | \psi_n^{(1)} \rangle + \langle \psi_n^{(1)} | H^{(1)} - E_n^{(1)} | \psi_n^{(0)} \rangle
\end{aligned} \tag{3.33}
$$

The general expression of the perturbation expansion, which allows to isolate specific i^{th}-

order corrections is [148]

$$\sum_{j=0}^{i} \sum_{k=0}^{i} \langle \psi_n^{(j)} | (H - E_n)^{(i-j-k)} | \psi_n^{(k)} \rangle = 0 \tag{3.34}$$

and the extension of the previous observation is the "$2n + 1$ theorem", which states that the $(2n+1)$-order derivative of the eigenenergies can be calculated from the knowledge of the wave function and its derivatives up to order n [148, 149]. Specifically, from the wave functions up to order n, it is possible to construct the derivatives of the energy up to order $2n + 1$. The search for the wave functions of order n can be achieved either by minimization of the energy functional of order $2n$ under the orthonormality constraints (3.31) or by direct resolution of Eqs. (3.30) [150].

3.6.2 Density Functional Perturbation Theory

Having defined the general expression of the equations within the perturbation theory, the application to the DFT formalism is straightaway. In fact, in previous sections, we have seen that within DFT the search for the ground-state of the electronic system can be achieved either by the minimization of the electronic energy functional with respect to the Kohn-Sham wave functions $|\psi_n\rangle$

$$E_{el}\{\psi_n^{(0)}\} = \sum_{n}^{occ} \langle \psi_n^{(0)} | (T + V_{ext})^{(0)} | \psi_n^{(0)} \rangle + E_{xc}^{(0)}[n^{(0)}] \tag{3.35}$$

under the constraint $\langle \psi_n^{(0)} | \psi_m^{(0)} \rangle = \delta_{nm}$, or by the self-consistent solution of Eq. (3.10), which can be rewritten in a compact formulation, as

$$H^{(0)} | \psi_n^{(0)} \rangle = [-\frac{1}{2} \nabla^2 + V_{ext}^{(0)} + V_{xc}^{(0)}] | \psi_n^{(0)} \rangle = E_n^{(0)} | \psi_n^{(0)} \rangle \tag{3.36}$$

with the exchange-correlation potential $V_{xc}^{(0)}(\boldsymbol{r}) = \frac{\delta E_{xc}[n^{(0)}]}{\delta n(\boldsymbol{r})}$, and $n(\boldsymbol{r}) = \sum_n \psi_n^*(\boldsymbol{r}) \psi_n(\boldsymbol{r})$.

Therefore, the perturbed electronic energy functional to be minimized is

$$E_{el}\{\psi_n(\lambda)\} = \sum_{n}^{occ} \langle \psi_n(\lambda) | T + V_{ext}(\lambda) | \psi_n(\lambda) \rangle + E_{xc}(\lambda)[n(\lambda)] \tag{3.37}$$

under the constraint (3.29), $\langle \psi_n(\lambda) | \psi_m(\lambda) \rangle = \delta_{nm}$, or, alternatively, the perturbed Schödinger equation to be solved is

$$H(\lambda) | \psi_n(\lambda) \rangle = [-\frac{1}{2} \nabla^2 + V_{ext}(\lambda) + V_{xc}(\lambda)] | \psi_n(\lambda) \rangle = E_n(\lambda) | \psi_n(\lambda) \rangle \tag{3.38}$$

with $V_{xc}(\boldsymbol{r}; \lambda) = \frac{\delta E_{xc}[n(\lambda)]}{\delta n(\boldsymbol{r})}$.

Then, the obtained in DFPT for the 1st derivative of the electronic energy is

$$E_{el}^{(1)} = \sum_n^{occ} \langle \psi_n^{(0)} | (T + V_{ext})^{(1)} | \psi_n^{(0)} \rangle + \frac{d}{d\lambda} E_{xc}[n^{(0)}]\Big|_{\lambda=0} \tag{3.39}$$

and the 2nd order derivative arises from the minimization with respect to $|\psi^{(1)}\rangle$ of the following expression

$$E_{el}^{(2)}\{\psi^{(0)}; \psi^{(1)}\} = \sum_n^{occ}[\langle \psi_n^{(1)} | (T + V_{ext})^{(1)} | \psi_n^{(0)} \rangle + \langle \psi_n^{(0)} | (T + V_{ext})^{(1)} | \psi_n^{(1)} \rangle] + \tag{3.40}$$

$$+ \sum_n^{occ}[\langle \psi_n^{(0)} | (T + V_{ext})^{(2)} | \psi_n^{(0)} \rangle + \langle \psi_n^{(1)} | (H - E_n)^{(0)} | \psi_n^{(1)} \rangle] +$$

$$+ \frac{1}{2} \int \int \frac{\delta^2 E_{xc}[n^{(0)}]}{\delta n(\boldsymbol{r})\delta n(\boldsymbol{r}')} n^{(1)}(\boldsymbol{r}) n^{(1)}(\boldsymbol{r}') d\boldsymbol{r} d\boldsymbol{r}' +$$

$$+ \int \frac{d}{d\lambda} \frac{\delta E_{xc}[n^{(0)}]}{\delta n(\boldsymbol{r})}\Big|_{\lambda=0} n^{(1)}(\boldsymbol{r}) d\boldsymbol{r} + \frac{1}{2} \frac{d^2 E_{xc}[n^{(0)}]}{d\lambda^2}\Big|_{\lambda=0}$$

Detailed descriptions, formulas, implementations and applications are provided in Refs. [141, 148, 149, 150, 142, 143, 152, 119, 151].

3.6.3   Accessible ground-state quantities

By focusing on quantities associated with first- and second- order derivatives of the total energy E with respect to atomic positions $\boldsymbol{R}_k$, homogeneous strain ξ and homogeneous electric field $\boldsymbol{\mathcal{E}}$ perturbations, all the functional properties of interest can be defined, namely forces $\boldsymbol{F}$, polarization $\boldsymbol{P}$, stress σ, dynamical Born effective charges Z^*, interatomic force constants C, indirect clamped-ion piezoelectric tensor e^0, optical dielectric tensor ϵ^∞, clamped-ion elastic constants c^0 and the internal strain coupling parameter g. Such a correspondence between quantities via successive derivatives is reported in Table 3.1.

E	1st-order	2nd-order		
		$\partial/\partial \boldsymbol{R}$	$\partial/\partial \xi$	$\partial/\partial \boldsymbol{\mathcal{E}}$
$\partial/\partial \boldsymbol{R}$	$\boldsymbol{F}$	C	g	Z^*
$\partial/\partial \xi$	σ	g	c^0	e^0
$\partial/\partial \boldsymbol{\mathcal{E}}$	$\boldsymbol{P}$	Z^*	e^0	ϵ^∞

Table 3.1: Physical quantities related to first- and second-order derivatives of the total energy E. Adapted from Ref. [92].

In the following, we focus on the specific description of the nuclear forces $\boldsymbol{F}$ and spontaneous polarization $\boldsymbol{P}$, while other physical properties, such as interatomic force constants, Born effective charges, and dielectric and piezoelectric responses have already been introduced in the previous Chapter [see Secs. (2.3.1), (2.3.3), and (2.4)].

Optimization of Ionic Positions: the Hellmann-Feyman theorem

In all the discussions related to DFT, no comment has been made about ionic positions, which have been assumed fixed, in turn leading to the correct electronic ground-state through the self-consistent relaxation of the electronic configuration. Actually, the determination of the lowest energy configuration for a given system also relies on the relaxation of the ionic positions and the size and shape of the unit cell. In many cases, the atomic configurations are known from experimental data, such as X-ray scattering or neutron diffraction, and they can be used as initial guess to find the minimum of the total energy as a function of atomic positions.

The equilibrium geometry of the system is given by the condition that the forces acting on individual ions I, given by differentiation of the adiabatic potential-energy surface $E(\boldsymbol{R})$ (3.4) with respect to the nuclear position $\boldsymbol{R}_I$, vanish:

$$\boldsymbol{F}_I = -\frac{\partial E(\boldsymbol{R})}{\partial \boldsymbol{R}_I} = 0 \tag{3.41}$$

In practice, the calculation of the equilibrium geometry relies on computing the first derivative of the Born-Oppenheimer energy surface. Such results arise from the application of the Hellmann-Feyman theorem to the interacting electronic-nuclear system. This theorem states that the gradient depending on a parameter λ along which to move to minimize the energy is obtained from the expectation value of the derivative of the Hamiltonian, as

$$\langle \psi_\lambda | \frac{\partial H_\lambda}{\partial \lambda} | \psi_\lambda \rangle = \frac{\partial E_\lambda}{\lambda} \tag{3.42}$$

It is worthy recognizing that such formulation corresponds to the first-order derivative of the energy previously introduced.

In this specific case the parameters λ are the coordinates $\boldsymbol{R}$ of the nuclei in the electronic adiabatic Hamiltonian (3.3). Therefore, derivation of both sides of Eq. (3.4) with respect to $\boldsymbol{R}_I$ reduces to the derivation of the electrons-nuclei V_{eN} interaction potential and Coulomb nuclei-nuclei E_{NN} repulsion energy, obtaining

$$\mathbf{F}_I = -\nabla_{\mathbf{R}_I} E = -\int d\mathbf{r}\, n(\mathbf{r}) \nabla_{\mathbf{R}_I} V_{eN}(\mathbf{r}) - \nabla_{\mathbf{R}_I} E_{NN} \tag{3.43}$$

Thus, the force acting on a given nucleus I depends on the negative gradient of the electrostatic potential energy originated from all the other nuclei and the unperturbed electronic charge density. Therefore, the forces on the nuclei should not be calculated until the electronic configuration is near at its ground-state: each time that the positions of the ions or the size and shape of the cell are changed, the electrons must be brought close to the ground-state of the new ionic configuration in order to calculate forces (and stresses) of the new ionic configuration [116]. In practice, this means that for each step in the relaxation of the ionic configuration, the relaxation of the electronic configuration to obtain the ground-state density must be performed.

The Hessian matrix of the Born-Oppenheimer energy surface is thus obtained by differentiating $\mathbf{F}_I$ with respect to nuclear coordinates,

$$\frac{\partial^2 E(\boldsymbol{R})}{\partial \mathbf{R}_I \partial \mathbf{R}_J} = -\frac{\partial \boldsymbol{F}_I}{\partial \boldsymbol{R}_J} = \int \frac{\partial n(\boldsymbol{r})}{\partial \mathbf{R}_J} \frac{\partial V_{eN}(\boldsymbol{r})}{\partial \mathbf{R}_I} d\boldsymbol{r} + \int n(\boldsymbol{r}) \frac{\partial^2 V_{eN}(\boldsymbol{r})}{\partial \mathbf{R}_I \partial \mathbf{R}_J} d\boldsymbol{r} + \frac{\partial^2 E_{NN}}{\partial \mathbf{R}_I \partial \mathbf{R}_J} \tag{3.44}$$

Eq. (3.44) therefore shows that the calculation of the Hessian matrix, which is referred as the matrix of the *interatomic force constants* (IFCs), requires the calculation of the ground-state electron charge density $n(\boldsymbol{r})$ as well as of its linear response to a distortion of the lattice, $\partial n(\boldsymbol{r})/\partial \mathbf{R}_I$ [119].

Polarization

As already discussed in the previous Chapter, the electric polarization $\mathbf{P}$ is one of the essential quantities in the physics of dielectric materials, being related to electric permittivity, ferroelectricity, dynamical effective charges, piezoelectricity, pyroelectricity and other phenomena. Specifically, the presence of a spontaneous and switchable macroscopic polarization is the signature of a ferroelectric material. A knowledge of the periodic electronic charge distribution in a polarized crystalline solid, cannot be used to construct a meaningful definition of *bulk polarization*. In this way $\mathbf{P}$ wrongly results being dependent on the shape and location of the unit cell of the investigated system [60]. In real materials, in fact, it is not possible to localize unambiguously the electronic charge, mainly in the ferroelectric ABO_3 oxides, which displays a mixed ionic/covalent character of the bondings.

Experimentally, the approach of measuring spontaneous polarization is through the polarization difference $\Delta \boldsymbol{P}$ rather than direct measurements of "polarization itself" exploiting its switchability: in a typical experiment, application of a sufficiently strong electric field switches the polarization from $\boldsymbol{P}$ to $-\boldsymbol{P}$. The quantity measured then corresponds to the difference in polarization between the two zero-field values of $\boldsymbol{P}$ in the hysteresis loop; one can then equate this difference to twice the spontaneous polarization [60].

Proceeding from the ambiguity in defining $\boldsymbol{P}$ as a single-value equilibrium property of the crystal in a given broken-symmetry state, the theoretical microscopic theory of polarization has also relied on differences in polarization between two different states, as suggested by Resta [153, 154]. Within the adiabatic approximation at zero temperature, the basic assumption of such theory is the existence of a continuous adiabatic transformation of the Kohn-Sham Hamiltonian connecting the two crystal states, under the hypothesis that (i) the transformation is performed at null electric field, and (ii) the system remains an insulator [154]. By parametrizing the transformation with a variable λ assuming values 0 and 1 at the initial and final states respectively, the change $\Delta \boldsymbol{P}$ can be expressed as

$$\Delta \boldsymbol{P} = \int_0^1 d\lambda \frac{\partial \boldsymbol{P}(\lambda)}{\partial \lambda} \tag{3.45}$$

As an example, λ could be an internal coordinate of the system representing the relative displacements of sublattices in the periodic crystal. Such a case is representative of the polarization induced by the zone-center polar phonon modes described in Sec. (2.3.2). This approach applies both to transformations that conserve volume and shape of the cell and to "cell-conserving" transformations [154].

The polarization $\boldsymbol{P}(\lambda)$ after integration with respect to λ (3.45) can be decomposed into ionic and electronic contributions:

$$\boldsymbol{P}(\lambda) = \boldsymbol{P}_{ion}(\lambda) + \boldsymbol{P}_{el}(\lambda) \tag{3.46}$$

The ionic term can be directly computed as

$$\boldsymbol{P}_{ion}(\lambda) = \frac{e}{V} \sum_k Z_k \boldsymbol{R}_k \tag{3.47}$$

where $\mathbf{R}_k$ and eZ_k are the position and charge of the atom k and V is the volume of the cell. The electronic polarization, instead, can be formulated by making use of the periodic Kohn-Sham orbitals $\psi_n(\mathbf{k}, \mathbf{r}; \lambda)$ and results

$$\mathbf{P}_{el}(\lambda) = \frac{e}{(2\pi)^3} \Im \sum_n \int d\boldsymbol{k} \, \langle u_n(\mathbf{k}, \mathbf{r})| \, \nabla_k \, |u_n(\mathbf{k}, \mathbf{r})\rangle \tag{3.48}$$

where the sum n runs over the occupied states. The latter form is then related to the *Berry phase* [60]. Formally, the central result of the modern theory of polarization is that $\boldsymbol{P}$ defined via the summation of (3.47) and (3.48) is only well-defined *mod $e\boldsymbol{R}$*/V, called quantum of polarization [154, 60], because of the translational invariance of bulk macroscopic property.

A quantitative and reliable estimation of the spontaneous polarizations in ferroelectrics can be achieved by the use of the *Born Effective Charges* (Sec. 2.3.3), which takes into account the contribution from the charges of both nuclei and electrons, by means of the following relation

$$P_\alpha = \frac{1}{\Omega_0} \sum_{k,\beta} Z^*_{k,\alpha\beta} \tau_{k,\beta} \tag{3.49}$$

with $Z^*_{k,\alpha\beta} = Z^{ion}_k \delta_{\alpha\beta} + Z^{el}_{k,\alpha\beta}$ [99, 155]. Such method can be a useful hint to find out the final value of $\boldsymbol{P}$ from direct Berry phase calculations.

3.7 Conclusions

In this chapter we have had an excursus over the first-principles technique based on the Density Functional Theory. The main general equations and approximations have been reported in order to introduce the general method used for the determination of the physical properties discussed and analyzed all along this thesis.

The basic approximations behind the access to the properties of materials at the atomic scale are the Born-Oppenheimer approximation and the Hohenberg-Kohn theorem, which via the variational principle allow to determine the ground-state electronic charge density of interacting particles. This reduces the problem to that of one-electron, defining an effective potential. The capability of the DFT to properly reproduce properties depends strongly on the form of the exchange-correlation energy introduced in such potential. The first formulation has relied on the local density approximation (LDA), but characterized by considerable inaccuracy in the determination of some electronic properties. An improvement has been then made by the semi-local generalized gradient approximations (GGA). Further developments due to the addition of perturbation theory within DFT have allowed the possibility to access directly properties associated to variations of the total energy by various perturbations. Accordingly, DFT and DFPT have become a standard and reliable methods for the investigation of the properties of solids.

Part III

Computational Results and Analysis

Chapter 4

Technical Details

4.1 Computational Details

We use the general framework of the density functional theory (DFT) (Chap. 3) to compute the structural properties and the electric polarization. Dynamical and piezoelectric properties have been calculated using Density Functional Perturbation Theory (DFPT) [142], as implemented in the ABINIT package [156, 157, 158]. The exchange-correlation potential was evaluated within the generalized gradient approximation (GGA) using the Wu-Cohen (WC) functional [133] for all simulations. Optimized Norm-Conserving Pseudopotentials [137] have been employed with the following orbitals considered as the valence states: $5s$, $5p$ and $6s$ for Ba, $3s$, $3p$ and $4s$ for Ca, $3s$, $3p$, $4s$ and $3d$ for Ti, $4s$, $4p$, $4d$ and $5s$ for Zr and $2s$ and $2p$ for O. The energy cutoff for the expansion of the electronic wave functions has been fixed to 45 Ha. Before performing computationally demanding calculations on ordered supercells by using a standard DFT approach, a first investigation has been performed using the VCA, which relies on virtual atoms obtained from combination of the reference atomic pseudopotentials [138, 139], as introduced in Sec. 3.5.2. In order to make proper comparative analysis, calculations have been performed with lattice parameters obtained by first-principles for all the studied systems, as experimental values are not available for all them. Accordingly, for the optimization of the cubic perovskite structures, phonons and polarization calculations within VCA, we used a $6 \times 6 \times 6$ k-points mesh for the Brillouin zone sampling for which energy is converged to $0.5\,meV$. For the optimization of the polar $P4mm$, $R3m$ and $Amm2$ and piezoelectric response calculations different sampling from $8 \times 8 \times 8$ to $8 \times 6 \times 6$ were used. For the optimization of the supercells and for the associated phonons calculations we used the $8 \times 8 \times 8$ k-mesh. For all the tetragonal superlattices we used $8 \times 8 \times 6$ k-mesh sampling. In order to allow comparison between different structures, energy will be reported in meV/f.u. (i.e. per 5 atoms). The q-points for the phonon dispersion curves and IFCs of the four pure compounds included Γ, X, M, R and the Λ point halfway from Γ to R of the simple cubic Brillouin zone.

4.2   Structure of the parent compounds

The optimized lattice parameters of the cubic structure of the four parent compounds are reported in Table 4.1. There, the atoms in the ABO_3 perovskite structure are labelled according to Fig 4.1. These values are used in Sec. 5.1 for the calculation of the phonon dispersion curves and interatomic force constants. The obtained values are in excellent agreement with experimental data for $BaTiO_3$ and $BaZrO_3$ [162, 163] (within 1%), whereas for $CaTiO_3$ the underestimation is of about 2% [164]. The larger error for $CaTiO_3$ can be assigned to the fact that the 0 K DFT results are compared to measurements at 1720 K. For $CaZrO_3$ the optimized lattice parameter overestimates the experimental value [165] of about 2%.

	$BaTiO_3$	$CaTiO_3$	$BaZrO_3$	$CaZrO_3$
Present	3.975	3.840	4.184	4.099
Exp.	4.003 [162]	3.897 [164]	4.191 [163]	4.020 [165]

Table 4.1: Relaxed lattice parameter a_{cell} (in Å) of the cubic structure of the four parent compounds. Experimental values are also reported for comparison.

4.3   Supercell structures

We have considered different supercells describing the Ca and Zr atomic substitutions in $BaTiO_3$ and performed DFPT calculations on the corresponding relaxed high-symmetry paraelectric structures.

For $Ba_{7/8}Ca_{1/8}TiO_3$ and $BaTi_{7/8}Zr_{1/8}O_3$, we have used the smallest reference structure which is the cubic $Pm\bar{3}m$ (O_1^h) with 40 atoms. The GGA-WC optimized lattice constants are 7.917 Å and 8.003 Å respectively (Fig. 4.2).

For $Ba_{0.50}Ca_{0.50}TiO_3$ and $BaTi_{0.50}Zr_{0.50}O_3$ three distinct geometric arrangements of the 40-atom cell were considered: columns of same cations along the [001] direction, layers of same cations parallel to the [110] planes and rocksalt configuration, Fig. 4.2. The paraelectric

Structure		$Ba_{0.50}Ca_{0.50}TiO_3$	$BaTi_{0.50}Zr_{0.50}O_3$
$P4/mmm$	columnar [001]	$a = b = 5.535$ $c = 3.899$	$a = b = 5.752$ $c = 4.104$
	layered [110]	$a = b = 3.911$ $c = 7.803$	$a = b = 4.098$ $c = 8.125$
$Fm\bar{3}m$		$a = b = c = 7.825$	$a = b = c = 8.150$

Table 4.2: Optimized lattice parameters (in Å) of the tetragonal-$P4/mmm$ and the cubic-$Fm\bar{3}m$ structures for $Ba_{0.50}Ca_{0.50}TiO_3$ and $BaTi_{0.50}Zr_{0.50}O_3$ solid solutions. For the tetragonal $P4/mmm$ we report values related to the reduced 10-atom cell. The relations with respect to the $2 \times 2 \times 2$ supercell are: (columnar) a=b=$a_{(2\times2\times2)}/\sqrt{2}$ and c=$c_{(2\times2\times2)}/2$; (layered) a=b=$a_{(2\times2\times2)}/2$ and c=$c_{(2\times2\times2)}$.

reference of the two first "ordered" structures are characterized by a tetragonal symmetry within the $P4/mmm$ (D_1^{4h}) space-group and they can be reduced by symmetry to 10-atom cell, whereas the rocksalt configuration has the cubic symmetry within the $Fm\bar{3}m$ (O_5^h) space-group. Structural relaxation have been done on the $2 \times 2 \times 2$ supercells (40 atoms) for each geometrical ordering, whereas DFPT calculations and structural relaxation of lower symmetry structures have been performed on the reduced 10-atom cell for the $P4/mmm$ structures and on the 40-atom cell for the $Fm\bar{3}m$ one. The optimized lattice parameters of the high-symmetry references are reported in Table 4.2. Figures have been produced by using the VESTA package [219].

A	(0.0, 0.0, 0.0)	A'	(0.0, 0.0, 1.0)
B	(0.5, 0.5, 0.5)	B'	(1.5, 0.5, 0.5)
O_1	(0.5, 0.5, 0.0)	O_4	(-0.5, 0.5, 0.0)
O_2	(0.5, 0.0, 0.5)	O_5	(0.5, 0.5, -1.0)
O_3	(0.0, 0.5, 0.5)	O_6	(-0.5, 0.0, 0.5)
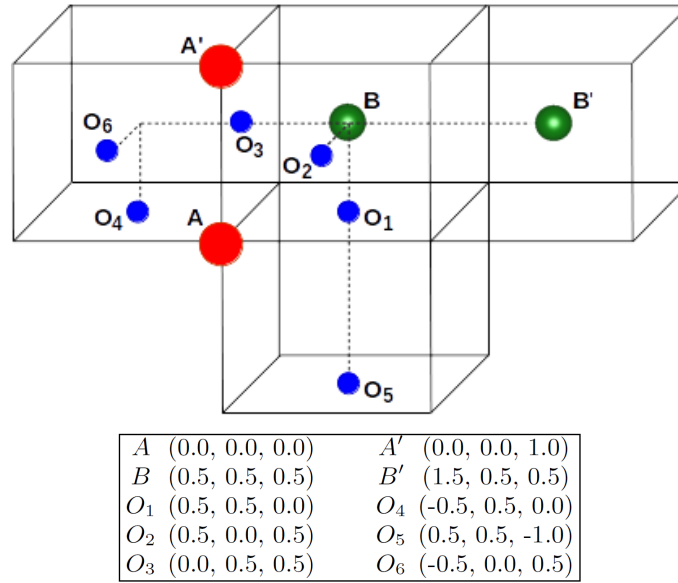
Figure 4.1: (Top) Schematic 3D-view of atoms. (Bottom) Positions in reduced coordinates of the atoms in the perovskite structure.
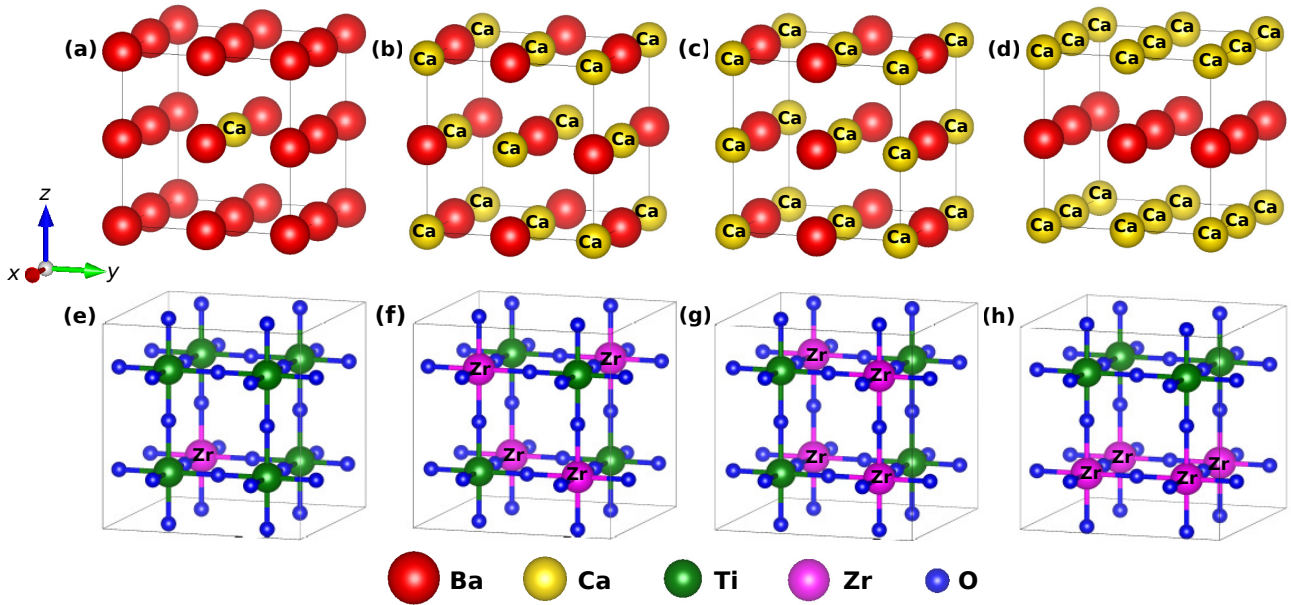
Figure 4.2: Schematic representation of different atomic ordering in $2 \times 2 \times 2$ supercells for the two investigated solid solutions. (Top) Sublattice of A cations in $Ba_{1-x}Ca_xTiO_3$. (Bottom) Sublattice of B cations and oxygens in $BaTi_{1-y}Zr_yO_3$. Ca and Zr atoms are labelled to help the visualization. (a,e) $x, y = 0.125$. (b,f) rocksalt order, (c,g) columnar order along the z axis and (d,h) layered order perpendicular to z axis for $x, y = 0.50$.

Chapter 5

Parent compounds

We start our study by considering individually the $BaTiO_3$, $CaTiO_3$, $CaZrO_3$ and $BaZrO_3$ parent compounds. The dynamics and the energetics of these systems is fundamental to understand the key features of the related solid solutions. Compared to other *ab-initio* studies on these systems, we report a careful analysis of the interatomic interactions, which helps to identify the key mechanisms driving their properties.

$BaTiO_3$ is one of the most studied perovskite, both from the theoretical [25, 166, 167, 168, 169] and experimental [170, 171, 172] points of view. This perovskite is characterized by a tolerance factor t greater than 1, $t \simeq 1.06$ [173], that allows to predict a polar distorted ground-state [173]. In fact, while stable at high temperature in the centrosymmetric cubic ($Pm\bar{3}m$) phase, it undergoes [172] ferroelectric structural phase transitions to a tetragonal ($P4mm$) structure at $\simeq 393~K$, to a orthorhombic ($Amm2$) phase at $\simeq 278~K$ and to a rhombohedral ($R3m$) ground-state at 183 K.

$CaTiO_3$, on the contrary, has a tolerance factor t smaller than 1, $t \simeq 0.97$ [173]. Accordingly, this compound displays a non-polar orthorhombic ($Pnma$) ground-state. It exhibits at least two observed phase transitions at high temperatures: from a cubic ($Pm\bar{3}m$) to a tetragonal phase ($I4/mcm$) at $\simeq 1634~K$ and from a tetragonal ($I4/mcm$) to the orthorhombic ground-state ($Pnma$) at ~ 1486 K [164, 174, 175].

$CaZrO_3$, that has $t \simeq 0.91$, was observed only in two different structures: the high temperature cubic ($Pm\bar{3}m$) form and its orthorhombic ($Pnma$) ground-state with the transition temperature at $\simeq 2170~K$ [177, 176, 178].

$BaZrO_3$, with $t \simeq 1.00$ [173], is experimentally not known to undergo any structural phase transition and remains in the paraelectric cubic phase down to 2 K [163].

In Sec. 5.1, we provide a comparison of the dynamical properties (phonon dispersion curves and interatomic force constants) of the parent compounds in their cubic phase. Then, in Sec. 5.2, we compare the energetics of various metastable phases of lower symmetry arising from the condensation of individual and combined distortions related to the unstable phonon modes identified in Sec. 5.1.

5.1 Dynamical properties

As introduced in Sec. 2.3.1, the identification of imaginary phonon frequencies and the corresponding displacement patterns allow us to pinpoint the main instabilities behind the structural phase transitions in our systems. Thus, we considered the cubic reference structure and we computed the phonon dispersion curves along selected high-symmetry lines in the simple Brillouin zone (Fig 2.2). The results are shown in Fig. 5.1.

The presence of imaginary phonon frequencies (shown as negative values in Fig. 5.1) reveals the structural instabilities of the cubic phase. The nature of the corresponding transition is usually determined by the character of the main unstable modes, and the related eigendisplacement vectors indicate the pattern of distortion, which spontaneously brings the system to more stable configurations. Furthermore, we complement this analysis with the calculation of the interatomic force constants in real space. As we have seen in the previous chapters, these constants are defined as $C_{k\alpha,k'\beta}(l,l') = \partial^2 E_{tot}/\partial\tau_{k\alpha}^l \partial\tau_{k'\beta}^{l'}$, where E_{tot} is the total energy of a periodic crystal and $\tau_{k\alpha}^l$ is the displacement of the atom k in the cell l along direction α from its equilibrium position. Their interpretation has been introduced in Sec. 2.3.4. In our analysis, we further separate the distinct contributions of the dipole-dipole interaction (DD) and short-range forces (SR) in order to identify the key mechanisms that lead the system to exhibit or not specific phonon instabilities. For a more detailed description of the physical meaning and its practical implementation see Refs. [142, 152, 101].

In the following we address a systematic description of the phonon dispersion curves reproduced in Fig. 5.1.

5.1.1 BaTiO$_3$

Ferroelectricity in BaTiO$_3$ is known to be related to the Ti off-centering driven by an unstable polar mode at Γ [168, 102]. This ferroelectric (FE) instability is such that it expand over the entire $\Gamma - X - M$ planes of the simple cubic Brillouin zone, as can be seen in Fig. 5.1(a). While each atom is at a position stable against individual displacements (Table 5.1), the origin of this distortion has to be primarily ascribed to the destabilizing Ti-O interaction, reflected in the positive value of the interatomic force constant along the bond's direction (Table 5.3). An additional contribution comes from the strong interaction of subsequent Ti-atoms along the B-B' chain direction compared to the small value in the transverse component. These anisotropic couplings give rise to a branch of unstable modes almost flat in the $\Gamma - X - M$ plane and highly dispersive along $\Gamma - R$. This reflects the chain-like nature of the instability in real space. The polar distortion requires cooperative atomic displacement along Ti-O chains [168]. Furthermore, the negligible contribution of Ba-atom to the ferroelectric distortion, has to be ascribed to its sizeable on-site force constant and very weak Ba-O$_1$ coupling.

In Table 5.2, we also compare the eigendisplacements associated to the unstable $F_{1u}(TO_1)$ mode to those of the stable $F_{1u}(TO_2)$ and $F_{1u}(TO_3)$ ones and we report the related mode
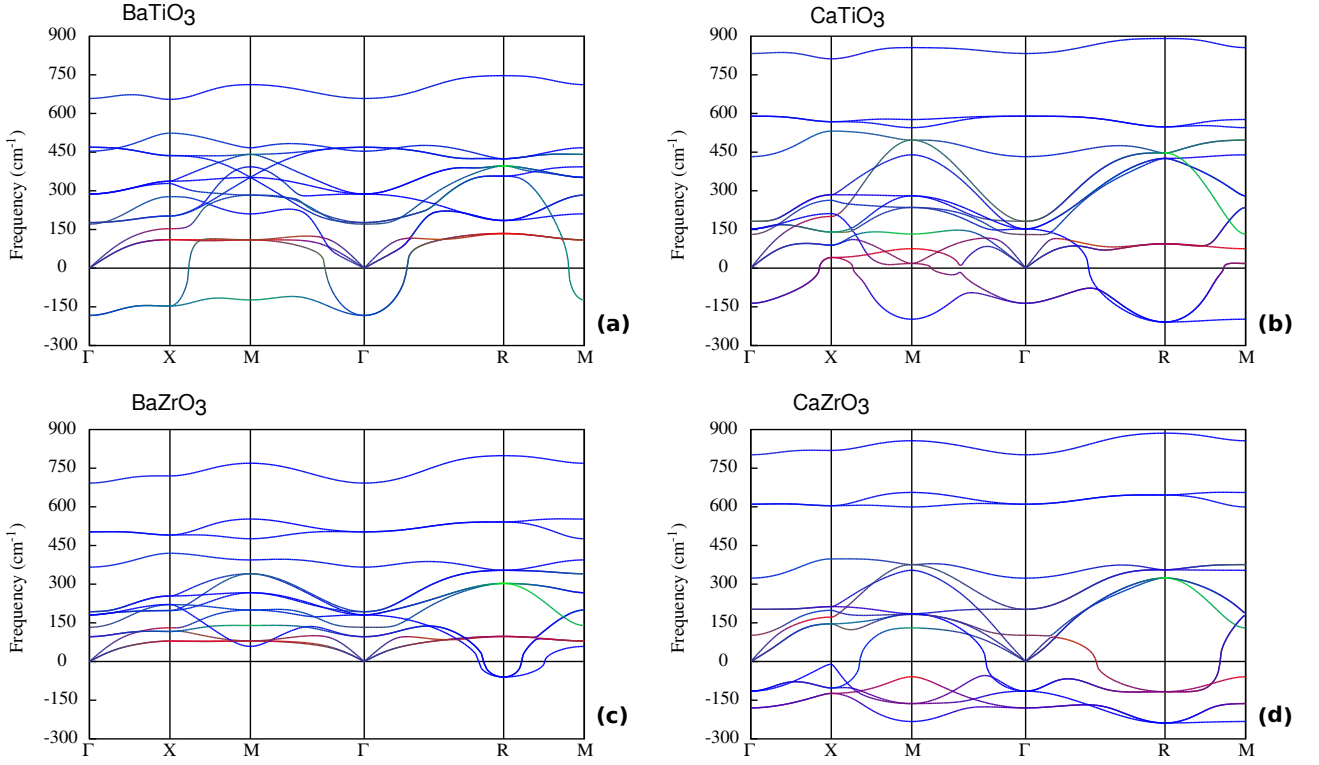
Figure 5.1: Calculated phonon dispersion curves of $BaTiO_3$ (a), $CaTiO_3$ (b), $BaZrO_3$ (c) and $CaZrO_3$ (d) along different high-symmetry lines in the simple cubic Brillouin zone. Negative values of frequencies refer to imaginary frequencies (ω are in cm^{-1}). The different colors indicate the different atomic contributions in the corresponding eigenvectors as in Ref. [102] (red for the A atom, green for B atom and blue for O atoms).

effective charges, as described in Ref. [142]. The mode effective charge is giant for the unstable mode in comparison to the others [100, 101]. In fact, the very anomalous Born effective charges on Ti and $O_{\parallel}$ combined through the specific pattern of eigendisplacements associated to the TO_1 mode produce a large spontaneous polarization. For the TO_2 and TO_3 modes, the motions are coupled so that Ti and O generate polarizations that partly compensate.

5.1.2 CaTiO$_3$

CaTiO$_3$ displays two main non-polar instabilities at the R and M points of the cubic Brillouin zone related to antiferrodistortive (AFD) motions ($\omega \simeq 209i\ cm^{-1}$ and $\omega \simeq 198i\ cm^{-1}$, respectively). These correspond to cooperative rotations of oxygen octahedron, around the B-atoms, with consecutive octahedron along the rotation axis being in-phase at M ($a^0a^0c^+$ in Glazer's notation [79]) and anti-phase at R ($a^0a^0c^-$). As such, the M-instability appearing in the phonon spectrum is a continuation of the instability at R, while in BaTiO$_3$ it is a continuation of the polar instability at Γ. The description of such AFD instabilities has been introduced in Sec. 2.3.2.

In addition, there is an unstable mode at the Γ-point that is also polar. This FE instability is now restricted to a region around the Γ-point highlighting a larger and more isotropic

ferroelectric correlation volume. This mode enables the condensation of a polar distortion. However, the character of the corresponding ferroelectricity is rather different compared to that in $BaTiO_3$ where it is dominated by the Ti displacements (B-site ferroelectricity). In fact, in $CaTiO_3$, this instability turns out to be dominated by the Ca displacements (A-type ferroelectricity) as can be seen from the eigendisplacements displayed in Table 5.2 and the red color of the corresponding phonon in Fig. 5.1(b). Despite this important involvement of the A-cation in the polar distortion, its Born effective charge is not strongly anomalous. This has to be ascribed to the fact that the polar distortion of Ca is driven by a steric effect. In fact, we already mentioned that $CaTiO_3$ has $t < 1$. Therefore, the small size of the Ca ionic radius allows its distortion in the cubic perovskite structure. Consequently, the involvement of the oxygens in the distortion is inverted with respect to the $BaTiO_3$ case, as the $O_{2/3}$ lying on the plane perpendicular to the direction of the distortion are now more involved than the apical oxygen (see Table 5.2).

These results can be rationalized by looking at the effect of the substitution of Ba by Ca on the "on-site" and interatomic force constants. In fact, the "on-site" force constant of Ca as well as the A-A' interaction are significantly smaller than the corresponding ones in $BaTiO_3$, while the "on-site" force constant of Ti is increased. Additionally, the destabilizing A-O_1 interaction (xx', Table 5.3) become significantly positive in agreement with the opposite direction of the respective atomic eigendisplacements (Table 5.2), whereas along the Ti-O_1 chain a stronger repulsive interaction prevents an important participation of the B-cation to the polar distortion.

These previous observations can be also related to the concurrent appearance of AFD distortions in the system. Although the IFCs between the reported pairs of oxygen are remarkably similar in $BaTiO_3$ and $CaTiO_3$ (and also in $BaZrO_3$ and $CaZrO_3$ as we will see below), the oxygens tilting is favored by the fast decrease of the oxygen "on-site" forces (linked to the destabilizing A-O_1 interaction) in the directions perpendicular to the B-O chains and to the increasing stiffness in the parallel direction (Table 5.1). Moreover, the phonon dispersion curves appear substantially flat along $R - M$ suggesting the absence of coupling between the oxygens in different planes, but, as can be seen in Tables 5.3 and 5.4, the transverse interactions are far to be negligible. As proposed in Ref. [102], this could be due to the joint action of the A-O coupling with a compensation between different interplane interaction of the oxygens (see also Ref. [179]).

5.1.3 $CaZrO_3$

$CaZrO_3$ exhibits much more intricate phonon branches than $CaTiO_3$. However, the dynamical properties of both compounds show some similarities. As in $CaTiO_3$, the strongest instabilities in cubic $CaZrO_3$ are the one at the R and M points of the Brillouin zone associated to AFD oxygen rotations ($\omega \simeq 238i \ cm^{-1}$ and $\omega \simeq 233i \ cm^{-1}$, respectively). Also, the dispersion curve

along $R - M$ appears completely flat.

Nevertheless, the lowest polar instability is no more confined at Γ, but the polar-antipolar instability extends all over the cubic Brillouin zone. This reflects a FE instability more localized in real space.

In $CaZrO_3$, the distortion is fully driven by the A-cation (Ca) and the $O_{2/3}$ anions. In fact, Zr at the B-site does not participate to the polar distortion with subsequent reduced participation of the apical O_1 [see Table 5.2-(TO_1 mode)]. Finally, the dynamical effective charges of both Zr and $O_\parallel$ appear less anomalous than in the titanates, resulting in a lower value of the mode effective charge.

As before, these dynamical properties can be understood in terms of IFCs. In fact, the "on-site" force associated to Ca and the in-plane "on-site" force of O are drastically reduced while for Zr it is strengthened. This reflects the fact that, with respect to their high-symmetry positions, the A-cation and the $O_{2/3}$ anions are highly unstable, while the B-cation remains almost fixed. Accordingly, the Ca-O_1 interatomic force constants are largely dominated by the dipole-dipole interaction, while the Zr-O_1 interaction is strongly repulsive. The interplay between all these features allows the understanding of the strong A-site driven character of the instabilities. In fact individual Ca displacements are nearly unstable (Table 5.1).

A proper comparison of $CaZrO_3$ an $CaTiO_3$ with respect to $PbZrO_3$ and $PbTiO_3$ respectively, can be done via the lattice dynamics analysis presented in Ref. [102].

5.1.4 BaZrO$_3$

Starting from the analyzed dynamics in $BaTiO_3$ and $CaZrO_3$, the dynamical properties of $BaZrO_3$ are fairly predictable. The substitution of the Ti atoms with Zr on the B-site joined to the presence of Ba on the A-site leads to the "quasi"-stability of the cubic phase, also confirmed by steric arguments, since the tolerance factor is close to 1. In fact, unlike the previous perovskite systems, the phonon spectrum of $BaZrO_3$ shows only a very weak instability at the R-point with associated phonon frequency $\omega \simeq 60.2i~cm^{-1}$ and no unstable polar modes.

By looking at the specific quantities reported in Table 5.2, the softest polar mode (TO_1) displays the smallest polarity ($\bar{Z}^*$) with respect to the corresponding modes in the other compounds. Moreover, unlike Ti in $BaTiO_3$, a tendency of Zr to decrease the spontaneous polarization results from the specific combination of the associated pattern of distortion with the dynamical charges. Conversely, the second stable polar mode (TO_2), even if stiffer, displays bigger polarity because of the additive contribution of Zr and O.

This behaviour can be justified by means of the force constants. In fact, the B-cation and O, along the transverse direction, experience now increased "on-site" terms with respect to $BaTiO_3$. The Zr-O_1 is then strongly dominated by the short-range forces. The A-cation, conversely, shows an "on-site" force constant in between $BaTiO_3$ and $CaTiO_3$, but the A-O interaction is still too weak to destabilize Ba (see Tables 5.1 and 5.3).

For all the four compounds, the interatomic force constants associated to the $A - B$ cations and to the O-O interactions have the same sign and order of magnitude. This trend points out the key role played by the on-site force constants in generating different kinds of instabilities according to the environment, which each atom experiences in the different perovskites. In fact, changes in the A-O and B-O interactions (Tables 5.1 and 5.3) are primarily associated to changes of those values.

Atom	Direction	BaTiO$_3$	CaTiO$_3$	BaZrO$_3$	CaZrO$_3$
A	$xx = yy = zz$	+0.0893	+0.0269	+0.0550	+0.0099
B	$xx = yy = zz$	+0.1635	+0.2236	+0.2198	+0.2510
O	$xx = yy$	+0.0711	+0.0432	+0.0396	+0.0171
	zz	+0.1454	+0.2624	+0.2135	+0.2909

Table 5.1: "On-site" force constants (in Ha/bohr^2) related to different atoms in the cubic phase of the four bulk compounds. A positive value means that the atomic position is stable against isolated displacement of the considered atom.

	BaTiO$_3$	CaTiO$_3$	BaZrO$_3^{**}$	CaZrO$_3$
Atom	Born effective charge Z^*			
$A^{(+2)}$	2.751	2.575	2.732	2.623
$B^{(+4)}$	7.289	7.188	6.099	5.903
$O_\parallel^{(-2)}$	-5.756	-5.730	-4.808	-4.862
$O_\perp^{(-2)}$	-2.142	-2.017	-2.012	-1.832
	$F_{1u}(TO_1)$			
ω (cm^{-1})	183.45i	136.21i	96.39	179.91i
$\bar{Z}^*$	9.113	6.453	3.954	4.455
	Eigendisplacements			
A	+0.0012	+0.0950	+0.0561	+0.1120
B	+0.0978	+0.0298	-0.0337	+0.0002
O_1	-0.1480	-0.0763	-0.0687	-0.0390
$O_{2/3}$	-0.0774	-0.1254	-0.1103	-0.1215
	$F_{1u}(TO_2)$			
ω (cm^{-1})	176.91	181.36	193.26	202.42
$\bar{Z}^*$	1.937	5.344	5.784	3.268
	Eigendisplacements			
A	+0.0547	-0.0922	-0.0228	-0.0823
B	-0.0800	+0.1116	+0.0781	+0.0698
O_1	-0.0715	-0.0189	-0.0353	-0.0039
$O_{2/3}$	-0.0793	-0.0421	-0.1068	-0.0940
	$F_{1u}(TO_3)$			
ω (cm^{-1})	468.91	589.62	503.07	610.29
$\bar{Z}^*$	1.281	4.269	3.777	4.601
	Eigendisplacements			
A	-0.0012	+0.0083	+0.0024	-0.0065
B	+0.0253	+0.0135	+0.0140	-0.0225
O_1	+0.1767	-0.2213	-0.2315	+0.2353
$O_{2/3}$	-0.1212	+0.0801	+0.0653	-0.0454

** BaZrO$_3$ has no instabilities at Γ, whereas the TO_1 mode is unstable for BaTiO$_3$, CaTiO$_3$ and CaZrO$_3$.

Table 5.2: Born effective charges (in $|e|$) of individual atoms in each parent compound followed by the frequencies, mode effective charges, and eigendisplacements ($< \eta|M|\eta >= 1$ with M in amu), of $F_{1u}(TO)$ phonon modes at Γ on the optimized cubic phase (Table 4.1). The mode effective charge is defined as in Ref. [142], $\bar{Z}^*_{TO} = \left| \frac{\sum_{k,\beta} Z^*_{k,\alpha\beta} \eta^{TO}_{k,\beta}}{\sqrt{< \eta^{TO}|\eta^{TO} >}} \right|$

Atoms		BaTiO₃			CaTiO₃			BaZrO₃			CaZrO₃		
		Total	DD	SR	Total	DD	SR	Total	DD	SR	Total	DD	SR
$A-A'$	(∥)	-0.0115	-0.0054	-0.0061	-0.0085	-0.0056	-0.0029	-0.0094	-0.0062	-0.0032	-0.0071	-0.0064	-0.0007
	(⊥)	+0.0039	+0.0027	+0.0012	+0.0040	+0.00281	+0.0012	+0.0130	+0.0106	+0.0024	+0.0042	+0.0032	+0.0010
$B-B'$	(∥)	-0.0693	-0.0379	-0.0314	-0.0788	-0.0438	-0.0350	-0.0564	-0.0308	-0.0256	-0.0593	-0.0323	-0.0270
	(⊥)	+0.0078	+0.090	-0.0111	+0.0084	+0.0219	-0.0135	+0.0071	+0.0154	-0.0083	+0.0065	+0.0162	-0.0097
$B-O_1$	(∥)	+0.0037	+0.2394	-0.2357	-0.0382	+0.2794	-0.3176	-0.0409	+0.1940	-0.2349	-0.0719	+0.2129	-0.2847
	(⊥)	-0.0203	-0.0445	+0.0243	-0.0184	-0.0492	+0.0308	-0.0166	-0.0406	+0.0240	-0.0148	-0.0401	+0.0253
$A-B$	(∥)	-0.0298	-0.0220	-0.0078	-0.0266	-0.0242	-0.0025	-0.0281	-0.0212	-0.0069	-0.0244	-0.0221	-0.0023
	(⊥)	+0.0139	+0.0110	+0.0029	+0.0150	+0.0121	+0.0029	+0.0130	+0.0106	+0.0024	+0.0133	+0.0111	+0.0023
$A-O_1$	(xx')	-0.0022	+0.0119	-0.0140	+0.0108	+0.0125	-0.0017	+0.0058	+0.0129	-0.0070	+0.0141	+0.0126	-0.0015
	(yy')	-0.0042	-0.0059	+0.0017	-0.0055	-0.0062	+0.0007	-0.0051	-0.0064	-0.0013	-0.0056	-0.0063	+0.0007
	(zz')	-0.0111	-0.0160	+0.0049	-0.0116	-0.0177	+0.0061	-0.0105	-0.0154	+0.0049	-0.0107	-0.0167	+0.0060
O_1-O_4	(xx')	-0.0020	-0.0033	+0.0013	-0.0022	-0.0035	+0.0012	-0.0019	-0.0034	+0.0014	-0.0020	+0.0012	-0.0078
	(yy')	+0.0018	+0.0016	+0.0002	+0.0014	+0.0017	-0.0003	+0.0018	+0.0017	+0.0001	+0.0012	+0.0016	-0.0003
	(zz')	+0.0093	+0.0118	-0.0025	+0.0107	+0.0139	-0.0032	+0.0070	+0.0096	-0.0026	+0.0078	+0.0110	-0.0032
O_1-O_5	(xx')	-0.0004	+0.0016	-0.0020	-0.0009	+0.0017	-0.0026	-0.0009	+0.0017	-0.0026	-0.0013	+0.0016	-0.0028
	(yy')	-0.0004	+0.0016	-0.0020	-0.0009	+0.0017	-0.0026	-0.0009	+0.0017	-0.0026	-0.0013	+0.0016	-0.0028
	(zz')	-0.0339	-0.0236	-0.0102	-0.0379	-0.0278	-0.0101	-0.0345	-0.0191	-0.0154	-0.0372	-0.0219	-0.0153

Table 5.3: Interatomic force constants in (Ha/bohr²) between different pairs of atoms in their local coordinates system, xx' (∥), yy' (⊥) and zz' (⊥) for ABO_3 bulk compounds. Transverse (⊥) directions for some atomic pairs are degenerate. The two different dipole-dipole (DD) and short-range (SR) contributions also reported.

Atoms		

	BaTiO$_3$			**CaTiO$_3$**		
$O_1 - O_2$	$\begin{pmatrix} +0.0038 & 0.0000 & 0.0000 \\ 0.0000 & -0.0091 & +0.0284 \\ 0.0000 & +0.0126 & -0.0091 \end{pmatrix}$			$\begin{pmatrix} +0.0057 & 0.0000 & 0.0000 \\ 0.0000 & -0.0120 & +0.0322 \\ 0.0000 & +0.0177 & -0.0120 \end{pmatrix}$		
	BaZrO$_3$			**CaZrO$_3$**		
	$\begin{pmatrix} +0.0039 & 0.0000 & 0.0000 \\ 0.0000 & -0.0060 & +0.0234 \\ 0.0000 & +0.0110 & -0.0060 \end{pmatrix}$			$\begin{pmatrix} +0.0051 & 0.0000 & 0.0000 \\ 0.0000 & -0.0071 & +0.0249 \\ 0.0000 & +0.0137 & -0.0071 \end{pmatrix}$		
	BaTiO$_3$			**CaTiO$_3$**		
$O_1 - O_6$	$\begin{pmatrix} -0.0007 & -0.0007 & +0.0013 \\ -0.0013 & +0.0014 & +0.0025 \\ +0.0007 & +0.0007 & +0.0014 \end{pmatrix}$			$\begin{pmatrix} -0.0007 & -0.0006 & +0.0017 \\ -0.0017 & +0.0015 & +0.0029 \\ +0.0006 & +0.0005 & +0.0015 \end{pmatrix}$		
	BaZrO$_3$			**CaZrO$_3$**		
	$\begin{pmatrix} -0.0077 & -0.0007 & +0.0013 \\ -0.0013 & +0.0012 & +0.0021 \\ +0.0007 & +0.0006 & +0.0012 \end{pmatrix}$			$\begin{pmatrix} -0.0007 & -0.0005 & +0.0016 \\ -0.0016 & +0.0013 & +0.0023 \\ +0.0005 & +0.0004 & +0.0013 \end{pmatrix}$		

Table 5.4: Interatomic force constant matrix in (Ha/bohr^2) between other pairs of oxygen in the Cartesian coordinates system. Rows and columns of the matrices correspond, respectively, to x, y and z directions.

5.2 Energetics of metastable phases

In the previous section we have seen that the parent compounds can develop two types of instability: a FE instability associated to a polar mode at Γ and AFD instabilities associated to unstable modes at M and R. In particular, now we quantify the energy difference associated to the condensation of the corresponding polar distortions and oxygen rotations with respect to the cubic phase. The results are shown in Fig. 5.2. A careful crystallographic explanation of the symmetry changes associated to these distortions can be found in Ref. [81].
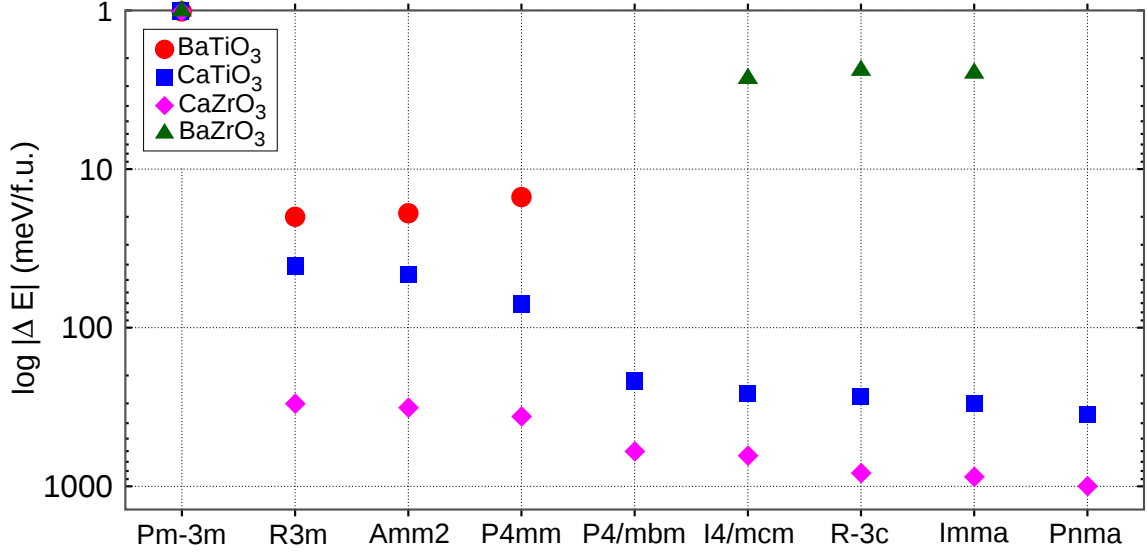

Figure 5.2: Energy landscape (in log scale) for BaTiO$_3$ (red closed circles), CaTiO$_3$ (blue closed squares), CaZrO$_3$ (pink closed rhombus) and BaZrO$_3$ (green closed triangle). For each ABO_3 perovskite, we report the energy gain with respect to the corresponding simple cubic phase, for different optimized phases allowed by dynamical properties (phonon spectra Fig. 5.1). Polar distortions, characterizing ferroelectric structures, and oxygen rotations, characterizing non-polar distorted structures, have been taken into account separately. All the structures have been fully relaxed within GGA-WC functional. Main features for the different structures are reported in Table 5.5.

5.2.1 BaTiO$_3$

In BaTiO$_3$ the energy sequence of the polar phases arising from the condensation of the polar mode is in line with the experimental sequence of phase transitions when lowering the temperature ($Pm\bar{3}m \rightarrow P4mm \rightarrow Amm2 \rightarrow R3m$). To be noticed is that the energy landscape is relatively flat. The $R3m$ ground-state is only 20 meV/f.u. below the paraelectric $Pm\bar{3}m$ phase and the energy difference between the polar phases is $\simeq 5$ meV/f.u. Interestingly, the anisotropy of the energy landscape (as well as of the polarization) is linked to the corresponding polar mode [168] and remain qualitatively unaffected by strain relaxation [see Figs. 6.5(a,d) in next chapter (Sec. 6.2)]. This is the signature of a relatively weak polarization-strain coupling in BaTiO$_3$ [187]. Accordingly, the calculated c/a ratio in the tetragonal phase is only ~ 1.02.

Polar structures		
Space group	Notation	Modes
$P4mm$ (99)	$a_0a_0a_1$	Γ_4^-
$Amm2$ (38)	$a_0a_1a_1$	Γ_4^-
$R3m$ (160)	$a_1a_1a_1$	Γ_4^-

Antiferrodistortive structures		
Space-group	Notation	Modes
$P4/mbm$ (127)	$a^0a^0c^+$	M_3^+
$I4/mcm$ (140)	$a^0a^0c^-$	R_4^+
$Imma$ (74)	$a^0b^-b^-$	R_4^+
$R\bar{3}c$ (167)	$a^-a^-a^-$	R_4^+
$Pnma$ (62)	$a^-b^+a^-$	R_4^+, M_3^+, X_5^+

Table 5.5: Space-group and main active modes in the two allowed classes of distortions. By referring to the simple cubic Brillouin zone: polar motion is due to instabilities at Γ (0,0,0), oxygen tilting to instabilities at M ($\frac{1}{2}, \frac{1}{2}, 0$) and R ($\frac{1}{2}, \frac{1}{2}, \frac{1}{2}$), and anti-polar motion to instabilities at X ($\frac{1}{2}, 0, 0$) or to the trilinear coupling with the two latter instabilities [81, 87], as in $CaTiO_3$. The polarization direction associated to the ferroelectric structures and Glazer notation associated to the antiferrodistortive structures are also reported.

5.2.2 $CaTiO_3$

Interestingly, in $CaTiO_3$ the energy sequence of the polar phases, arising from the condensation of the unstable polar mode, is reversed. In addition, the relative energy difference is larger than in $BaTiO_3$. In fact, the tetragonal $P4mm$ structure is the lowest energy configuration among the polar ones with a relative energy gain of about 70 meV/f.u. Moreover, unlike in $BaTiO_3$, we note that the initial instability is relatively isotropic and the strain relaxation is now crucial to obtain the eventual anisotropy [see Figs. 6.5(c,f) in Sec. 6.2]. Accordingly, the calculated c/a ratio in the tetragonal phase becomes ~ 1.06. It is noteworthy that such large strain coupling was previously reported in compounds with stereochemically active lone pair at the A-site like $PbTiO_3$ [84, 180] and $BiFeO_3$ [181, 182]. However, the above indicates that it is a more generic feature related to strongly A-type ferroelectricity.

Additional non-polar structures arising from the condensation of the unstable AFD modes at M and R also appear as metastable or eventually stable. As usual in perovskites with $t < 1$ [81], in fact, the ground-state corresponds to the $Pnma$ ($a^-b^+a^-$) structure which is $\simeq -350$ meV per f.u. below the reference cubic phase. One-tilt structures, such as $P4/mbm$ ($a^0a^0c^+$) or $I4/mcm$ ($a^0a^0c^-$), and the two-tilts $Imma$ ($a^0b^-b^-$) are intermediate metastable structures that appear $\simeq 100$ meV and $\simeq 50$ meV per f.u. above the ground-state, respectively.

5.2.3 CaZrO$_3$

In CaZrO$_3$ the energy sequence of both the polar and AFD phases is the same as CaTiO$_3$, but they are shifted down in energy becoming very spread. The AFD-*Pnma* ground-state is lower by about -1 eV/f.u. than the $Pm\bar{3}m$ phase. This is in tune with the very high transition temperature experimentally observed for the sequence $Pm\bar{3}m \rightarrow Pnma$, even if the phonon frequencies related to the unstable modes are close to the ones in CaTiO$_3$.

5.2.4 BaZrO$_3$

For BaZrO$_3$ we found competitive stable $R\bar{3}c$ $(a^-a^-a^-)$, $Imma$ $(a^0b^-b^-)$ and $I4/mcm$ $(a^0a^0c^-)$ antiferroditortive structures. From phonon calculations performed on the three distorted structures, in fact, no instabilities have been found. Further details are provided in Appx. A. According to the very tiny value of the instability in the cubic phase then [Fig. 5.1(c)], the condensation of the oxygen rotations provides an energy gain relative to the cubic phase of about $\simeq 2.5$ meV per f.u., while the three distorted phases have an energy that differs by less than 0.2 meV/f.u. In spite of the negligible energy gain, the amplitude of the AFD distortion is significant. The biggest distortion is appearing in the tetragonal phase with an angle of rotation of $\sim 4°$ about the [001] direction.

5.2.5 Polar modes and ferroelectric phases

In order to interlock the optimized polar structures with the lattice dynamics, we evaluated the contribution of each polar mode to the condensed distortion. The overlap matrix is reported in Table 5.6. It is interesting to notice, that the three ferroelectric states are mostly due to the condensation of the unstable optical mode for all the three perovskites BaTiO$_3$, CaTiO$_3$ and CaZrO$_3$, so that it is possible to establish a nearly one-to-one correspondence with the pattern of distortion associated to the unstable TO_1 mode and the displacements as obtained from the structural optimization, while the contribution of the TO_2 and TO_3 modes remains very small.

An important remark is the huge difference in the total distortion $\boldsymbol{\tau}$ between BaTiO$_3$ and the Ca-based perovskites, that allow for possible bigger spontaneous polarization in the latter compounds even if the A-cation at play is not either stereochemically active or involved in the hybridization with the oxygens.

5.3 Conclusions

The previous analysis of the dynamics and energetics associated to the four parent compounds has emphasized some similarities and differences. In particular through the analysis of the "on-site" and interatomic force constants, we have identified some key interactions tuning the different dynamical and related properties. This is helpful for a better understanding of prop-

BaTiO$_3$			
	$P4mm$	$Amm2$	$R3m$
$|\boldsymbol{\tau}|$	0.188	0.209	0.214
$F_{1u}(TO_1)$	0.993	0.975	0.971
$F_{1u}(TO_2)$	0.110	0.087	0.129
$F_{1u}(TO_3)$	0.032	0.194	0.228

CaTiO$_3$			
	$P4mm$	$Amm2$	$R3m$
$|\boldsymbol{\tau}|$	0.601	0.478	0.435
$F_{1u}(TO_1)$	0.985	0.970	0.970
$F_{1u}(TO_2)$	-0.171	-0.203	-0.199
$F_{1u}(TO_3)$	0.033	0.129	-0.143

CaZrO$_3$			
	$P4mm$	$Amm2$	$R3m$
$|\boldsymbol{\tau}|$	0.903	0.886	0.868
$F_{1u}(TO_1)$	0.976	0.910	0.897
$F_{1u}(TO_2)$	-0.060	0.202	-0.208
$F_{1u}(TO_3)$	-0.067	-0.336	-0.197

Table 5.6: Overlap matrix between the total distortion $\boldsymbol{\tau}$ of the three optimized polar structures and the eigendisplacements $\boldsymbol{\eta}_i$ associated to the $F_{1u}(TO)$ modes of the optimized cubic phase, $\langle \boldsymbol{\eta}_i | M | \boldsymbol{\tau} \rangle = \alpha_i$. The distortion $\boldsymbol{\tau}$ has been normalized such that $\langle \boldsymbol{\tau} | M | \boldsymbol{\tau} \rangle = 1$, with M in atomic mass units, and results to be defined as $\boldsymbol{\tau} = \sum_{i=1,2,3} \alpha_i \boldsymbol{\eta}_i$, with $|\boldsymbol{\tau}| = \sqrt{\langle \boldsymbol{\tau} | M | \boldsymbol{\tau} \rangle}$. Since BaZrO$_3$ has no polar instabilities we report results only for BaTiO$_3$, CaTiO$_3$ and CaZrO$_3$.

erties arising while mixing cations at the A- and B-sites in (Ba,Ca)TiO$_3$ and Ba(Ti,Zr)O$_3$ solid solutions, respectively. Additionally, we note that the parent BaTiO$_3$ and CaTiO$_3$ compounds display inverted sequence of polar phases. Then, for the (Ba,Ca)TiO$_3$ solid solutions, the emergence of a region with strong competition between these phases and a crossing point in energetics can be expected. This will be confirmed in the next chapter.

We will now present results coming from a systematic characterization of the latter systems by also testing and comparing two different approaches: the "virtual crystal approximation" (VCA) and supercell-based calculations.

Chapter 6

(Ba,Ca)TiO$_3$ solid solutions

In the last few years, Ba$_{1-x}$Ca$_x$TiO$_3$ (BCT) has started to arouse curiosity in the experimental community as the Ca off-centering seems to play an important role in stabilizing ferroelectricity against chemical pressure effects [183, 184, 185]. In particular, in Ref. [184], Fu and Itoh have characterized single crystals of BCT in a temperature range from 2 K to 400 K and for compositions ranging from $x = 0.00$ up to $x = 0.34$. They found that the Curie point is nearly independent of the Ca-concentration for the $Pm\bar{3}m \rightarrow P4mm$ transition, whereas there is a shift of the $P4mm \rightarrow Amm2$ and $Amm2 \rightarrow R3m$ phase transitions toward lower temperatures. Accordingly, the effect of Ca-substitution is the stabilization of the tetragonal ferroelectric phase.

Let us now analyze the dynamics and energetics as predicted by means of first-principles calculations. We first report results from the VCA approach in Sec. 6.1, then from the use of supercells in Sec. 6.2.

6.1 VCA approach

6.1.1 Lattice parameter

First, we report the evolution of the lattice parameter of the $Pm\bar{3}m$-cubic phase as obtained from the structural optimization within VCA. Because of the reduced volume of CaTiO$_3$ with respect to BaTiO$_3$ (Table 4.1), the lattice parameter decreases monotonically with the Ca-concentration, but the trend deviates from the linearity of the Vegard's law, as shown in Fig. 6.1(a).

As for the pure compounds, for solid solutions we can define the tolerance factor as $t = (\overline{r_A} + r_O)/\sqrt{2}(r_B + r_O)$, with $\overline{r_A} = (1-x)r_{Ba} + (x)r_{Ca}$. Values of the ionic radii, r_i, for the pure atoms have been taken from Ref. [186]. For increasing x, t decreases from 1.06 to 0.97 reaching 1 at $x = 0.6$, as reported on top of Fig. 6.1.

6.1.2 Dynamical properties

We analyze the evolution of the lowest phonon frequencies at the high symmetry points of the Brillouin zone of the cubic reference. DFPT calculations have been performed on the optimized structures. We find that, for increasing Ca-concentration, the original polar instabilities of BaTiO$_3$ changes character by becoming confined to the center of the Brillouin zone (AFE instabilities at X and M disappear), while the AFD modes due to oxygen rotations become unstable, as shown Fig. 6.1(b). Changes in the phonon instabilities are linked to the evolution of t. In fact, the polar instability dominates until t becomes smaller than one at which the AFD rotational modes become largely unstable. Specifically, the lattice dynamics is BaTiO$_3$-like for $0 \leq x \leq 0.2$. The unstable polar mode at Γ is mainly sustained by the destabilizing Ti-O interaction, while the A-O interaction stays mostly repulsive, resulting in the inactivity of the A-site, as reproduced in Fig. 6.1(c,d,e). Accordingly, the instabilities at the X- and M-points are also due to Ti-O polar motion. For $0.3 \leq x \leq 0.6$, the scenario starts to change. The polar instability becomes weaker as it results from the important reduction in the amplitude of the associated frequencies. Particularly, the polar distortion remains unstable at Γ, while it becomes progressively stable at X and M. These smooth changes can be related to smooth changes in the type of interaction between the cations and the oxygens. A change of sign is observed along both the Ti-O and A-O interaction that corresponds to a strong competition between attractive and repulsive forces in determining the nature and character of the polar instability: a reduction of the amplitude of the Ti-motion corresponds to increasing negative value of the Ti-O interaction, while an increasing contribution to the polar distortion of the A-site arises from positive values of the A-O interaction, as shown in Fig. 6.1(c,d,e). Finally, for $0.7 \leq x \leq 1.0$, the lattice dynamics becomes CaTiO$_3$-like. Accordingly, instabilities related to oxygen rotations appear at the M- and R-points of the cubic Brillouin zone and are more unstable than the polar one at Γ. This situation results from strong destabilizing A-O interactions and largely repulsive Ti-O interactions. Accordingly, the character of the polar distortion also changes by becoming largely driven by the motion of the A-site with respect to the B-one.

Moreover, changes in the phonon behavior also affect the dynamics of the oxygens. The increasing contribution to the distortion from the A-site, i.e. increasing long-range forces between the A-cation and oxygens, favors the motion of the planar oxygens with respect to the apical one (labelled O$_{2/3}$ and O$_1$ in Fig. 6.1(e), respectively). Specifically, the contribution is reversed when going from $t > 1$ to $t < 1$.

The latter analysis of the evolution of the dynamical properties when going from the BaTiO$_3$-rich region to the CaTiO$_3$-rich one in the Ba$_{1-x}$Ca$_x$TiO$_3$ "virtual-system" reveals the presence of two parallel mechanisms: the progressive weakening of the long-range forces between Ti and O atoms in favor of their strengthening between the A-atoms and oxygens. In terms of character of the phonons instabilities, this change corresponds to a smooth evolution from the B-driven
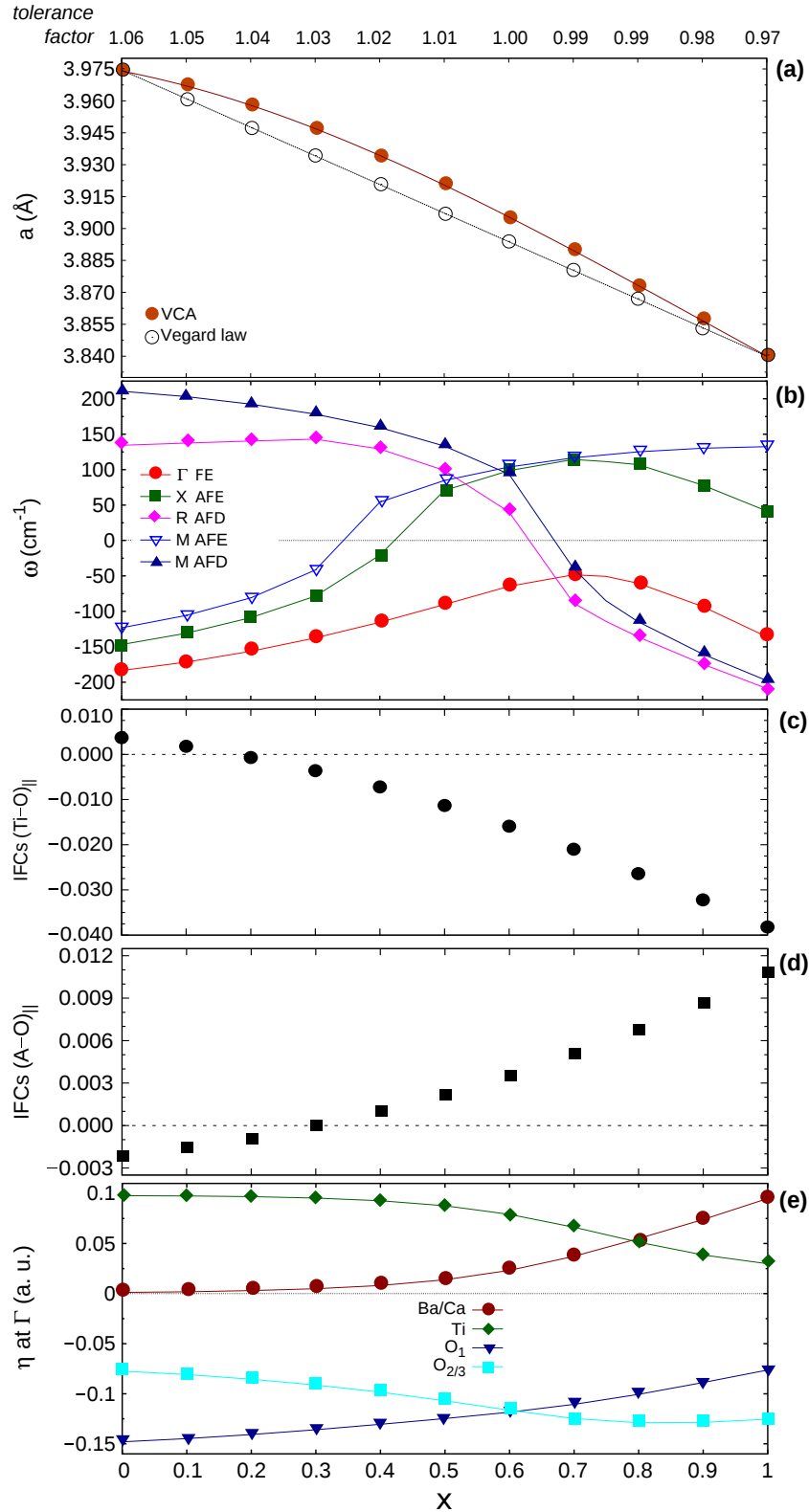
Figure 6.1: Evolution of different lattice properties as a function of x-composition in $Ba_{1-x}Ca_xTiO_3$ as obtained by the use of VCA. (a) Cubic lattice parameter a_{cell} (in Å). Vegard's law has been built on the theoretical values of the cubic $BaTiO_3$ and $CaTiO_3$ reported in Table 4.1: $a(x) = (1-x)a_{BTO} + (x)a_{CTO}$. (b) Trend of the lowest phonon frequencies at the high-symmetry points of the simple cubic Brillouin zone. Evolution of the total Ti-O (c) and A-O (d) Interatomic Force Constants (IFCs in $Ha/bohr^2$). (e) Evolution of normalized eigendisplacements (in $a.u.$) associated to the unstable polar mode at the Γ-point of the simple cubic Brillouin zone. Lines are guide for the eyes.

into the A-driven distortions associated to the parents BaTiO$_3$ and CaTiO$_3$, respectively. The reasons behind these two phenomena are also different and complementary. In fact, Ca-doping of the virtual A-site produces: (i) varying interatomic force constants between the A-O atomic pair in favors of destabilizing long-range forces sustained by the progressive lowering of the A-cation stiffness when going from BaTiO$_3$ to CaTiO$_3$ (see Table 5.1); (ii) reduction of the volume, that can be considered as increasing isotropic pressure on the ATiO$_3$ system and, therefore, shortening of the Ti-O bond lengths. The latter effect produces increasing stiffness of Ti-atoms, that results in the change of sign of the Ti-O interatomic force constants and associated weakening of the B-type ferroelectricity. In fact, as investigated at the first-principle level in Refs. [187, 188, 189] and as it turns out when comparing graphs (a) and (c) reported in Fig. 6.1, the balance between short-range and long-range forces between the Ti and O atoms is strongly sensitive to pressure. At variant, the varying composition does not affect significantly the A-B interaction, that in fact remains almost the same as in the pure parent compounds (see Tables 5.3 and 6.1).

6.1.3 Energy landscape

As we previously did for the pure parent compounds, now that the main instabilities of BCT "virtual-system" have been identified, we look at the energy competition between different phases arising from the condensation of the corresponding modes in order to obtain an overview of the energetics as a function of concentration. As shown in Fig. 6.2, the main effect of
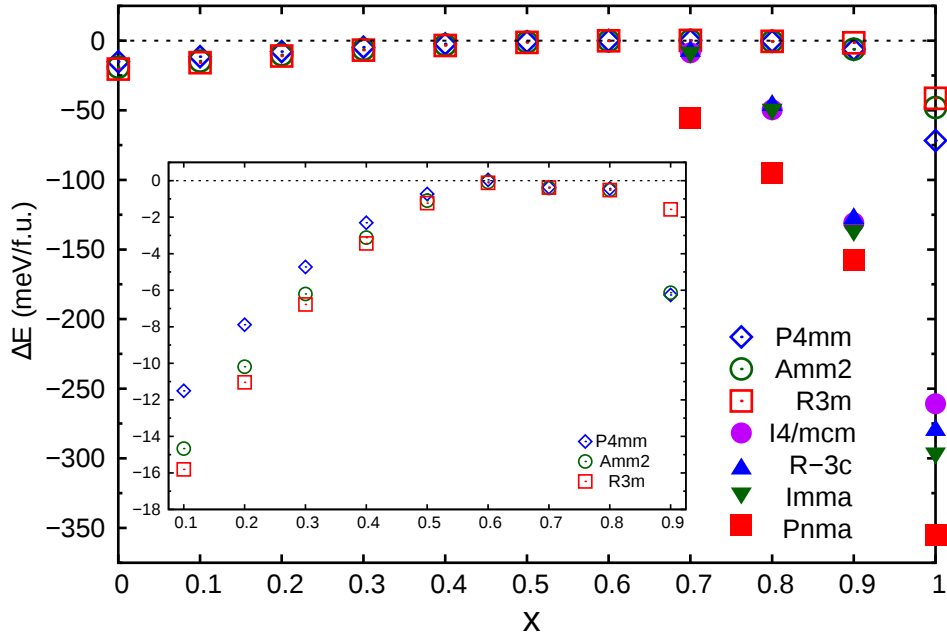

Figure 6.2: Energy gain with respect to the simple cubic phase for different optimized structures allowed by dynamical properties within VCA as a function of x-composition in Ba$_{1-x}$Ca$_x$TiO$_3$. Structures properties reported in Table 5.5. The inset shows a zoom on the energetics of the polar phases for $0.1 \leq x \leq 0.9$.

the Ca-substitution is to reduce the energy gain both between the three ferroelectric phases and with respect to the cubic phase by making them strongly competitive, while additional antiferrodistortive structures appear as metastable in the CaTiO₃-rich region by providing a non-polar ground-state.

Such behaviour proceeds from the evolution of the dynamical properties previously analyzed. In fact, an important energy competition between polar phases starts at $x = 0.3$, that corresponds to the concentration where we observe the change of sign of the Ti-O IFCs [see Fig. 6.2(c)]. Then, the energies of the polar phases smoothly converge to that of the cubic one in line with the progressive weakening of the polar instability. Noteworthy is that the inversion in the energy sequence of the three polar phases happens at $x = 0.9$ where we observe the inversion of the dominant character of the polar instability between virtual A-cation and Ti [see Fig. 6.2(e)].

Additional structures with oxygen rotations appear with an higher energy gain from $x = 0.7$ proceeding from the appearance of the related phonons instabilities in the cubic phase [see Figs. 6.1(b) and 6.2]. It is also noteworthy that the contribution to the polar distortion arising from the apical and planar oxygens is inverted from this point, with the dominant motions of the latter ones (see Fig. 6.1(e)).

6.1.4 Polarization and piezoelectric response

Proceeding from the previous observation that for $0.0 \leq x \leq 0.6$ the BCT "virtual-system" experiences a progressive weakening of the ferroelectric instability and that no other phonons are unstable, we now evaluate the evolution of the spontaneous , P_s, and piezoelectric coefficients, d_{ij}. According to the VCA results, we performed calculations on the lowest energy rhombohedral-$R3m$ structure (Fig 6.2). Values are normalized to the calculated ones of pure $R3m$-BaTiO₃, that are $P_s^{BTO} \simeq 38 \ \mu C/cm^2$ and $d_{11}^{BTO} \simeq 76 \ pC/N$, $d_{15}^{BTO} \simeq 270 \ pC/N$ and $d_{33}^{BTO} \simeq 15 \ pC/N$.

Specifically, in Fig. 6.3, we report P_s as obtained both via first-principles calculations by means of the Berry Phase Theory [191] (blue circles) and via the Born effective charges by means of the approximation $P_{s,\alpha} = \frac{1}{\Omega} \sum_{k,\beta} Z_{k,\alpha\beta}^* \Delta \tau_{k,\beta}$ [99] (green rhombus). It results that P_s decreases as function of increasing Ca-composition in tune with the decreasing energy gain associated to the polar phases in this range of composition, i.e. the weakening of the polar instability detected within VCA (Figs. 6.1 and 6.2). In order to clarify if changes in the polarization are mostly due to varying effective charges or atomic distortions, we disentangled the two contributions. In the first case, we kept constant the atomic displacements of pure $R3m$-BaTiO₃ and took into account the different effective charges associated to each BCT compositions (orange triangles). In the second case, we kept constant the Born effective charges of pure $R3m$-BaTiO₃ and considered the distortion arising from different compositions (red circles). It results that the evolution of P_s has to be widely ascribed to changes in atomic distortion in BCT "virtual-
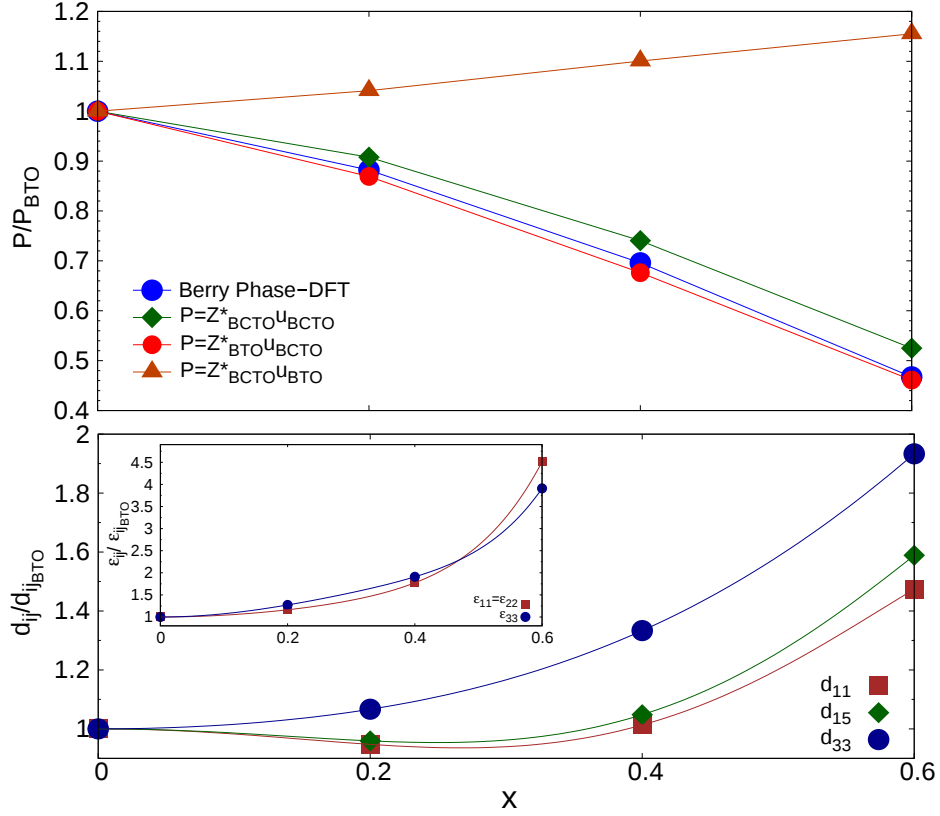
Figure 6.3: Evolution of polarization, piezoelectric and stress-free dielectric coefficients in the rhombohedral-$R3m$ phase as a function of x-composition in Ba$_{1-x}$Ca$_x$TiO$_3$ within VCA. Values are normalized to the ones of $R3m$-BaTiO$_3$: $P_s^{BTO} \simeq 38~\mu C/cm^2$; $d_{11}^{BTO} \simeq 76~pC/N$, $d_{15}^{BTO} \simeq 270~pC/N$ and $d_{33}^{BTO} \simeq 15~pC/N$; $\varepsilon_{11}^{BTO} \simeq 208$ and $\varepsilon_{33}^{BTO} \simeq 11$. Upper panel: variation of the polarization as directly computed by Berry-phase calculations (blue circles) and by Born effective charges approximation to disentangle the contribution of varying atomic charges and displacements. Lower panel: trend of the d_{ij} coefficient and stress-free dielectric response ε_{ij}.

system" in such range of composition, as shown in Fig. 6.3 (top). In fact, this behaviour is in line with the evolution of the eigendisplacements associated to the unstable polar mode at Γ with a pronounced reduction of the titanium and oxygens motion Fig. 6.1(e).

Despite the decrease of polarization, the piezoelectric response increases with the Ca-concentration (Fig. 6.3 bottom). This trend is due to the fact that the stress-free dielectric response, ε_{ij}, remarkably increases as well, as shown in the inset of Fig. 6.3. By writing down the piezoelectric coefficient as $d_{ik} = \frac{de_{s,i}}{dE_k} \propto (\chi_{j,k}P_{s,l} + P_{s,j}\chi_{l,k})$ [46] (Sec. 2.2), it is easier to understand such a trend: near a phase transition, where the lowest-frequency polar mode, i.e. the soft mode, goes to zero, the dielectric response diverges [93]. Accordingly, the calculated values of the lowest-frequency polar modes in the $R3m$-phase evolve like 169, 160, 124, 73 (in cm^{-1}) for 0.0, 0.2, 0.4 and 0.6 x-composition, respectively. Therefore, the softening of the polar mode overcomes the reduction of P_s in the piezoelectric response within the VCA approach.

$Ba_{0.875}Ca_{0.125}TiO_3$								
VCA					**2x2x2 CELL**			
Atoms		Total	DD	SR	Atoms		Total	DD	SR

Atoms		Total	DD	SR	Atoms		Total	DD	SR
$A - A'$ d=3.967 Å	($\parallel$)	-0.011	-0.005	-0.006	Ba-Ba' d=3.959 Å	($\parallel$)	-0.012	-0.006	-0.006
						($\perp$)	+0.004	+0.003	+0.001
	($\perp$)	+0.004	+0.003	+0.001	Ca-Ba d=3.959 Å	($\parallel$)	-0.009	-0.005	-0.004
						($\perp$)	+0.004	+0.003	+0.001
$B - B'$ d=3.967 Å	($\parallel$)	-0.070	-0.038	-0.032	Ti-Ti' d=3.929 Å	(xx')	-0.072	-0.040	-0.033
	($\perp$)	+0.008	+0.019	-0.011		(yy')	+0.008	+0.020	-0.012
						(zz')	+0.009	+0.020	-0.011
$A - B$ d=3.436 Å	($\parallel$)	-0.030	-0.022	-0.008	Ba-Ti d=3.437 Å	($\parallel$)	-0.030	-0.022	-0.008
						($\perp$)	+0.014	+0.011	+0.003
	($\perp$)	+0.014	+0.011	+0.003	Ca-Ti d=3.403 Å	($\parallel$)	-0.023	-0.022	-0.001
						($\perp$)	+0.013	+0.011	+0.003
$B - O_1$ d=1.984 Å	($\parallel$)	+0.002	+0.242	-0.241	Ti-O_1 d=1.994 Å	($\parallel$)	+0.005	+0.236	-0.231
						($\perp$)	-0.020	-0.045	+0.025
	($\perp$)	-0.020	-0.045	+0.025	Ti-O_2 d=1.965 Å	($\parallel$)	-0.007	+0.253	-0.260
						($\perp$)	-0.020	-0.044	+0.024
$A - O_1$ d=2.805 Å					Ba'-O_1 d=2.783 Å	(xx')	-0.004	+0.012	-0.016
						(yy')	-0.011	-0.016	+0.005
						(zz')	-0.004	-0.006	+0.002
	(xx')	-0.001	+0.012	-0.013	Ba'-O_2 d=2.800 Å	(xx')	-0.003	+0.012	-0.015
	(yy')	-0.004	-0.006	+0.002		(yy')	-0.005	-0.006	+0.001
	(zz')	-0.011	-0.016	+0.005		(zz')	-0.011	-0.016	+0.005
					Ca-O_2 d=2.750 Å	(xx')	+0.011	+0.011	-0.000
						(yy')	-0.005	-0.006	+0.001
						(zz')	-0.011	-0.016	+0.005

Table 6.1: Interatomic force constants for $Ba_{0.875}Ca_{0.125}TiO_3$ from VCA and super cell calculations. Units are in Ha/bohr^2. Directions xx' ($\parallel$), yy' ($\perp$) and zz' ($\perp$) refer to local coordinates system of the different pairs of atoms. Distances (in Å) between the selected atoms are also reported. Atoms' notation in the second column is consistent with Fig. 6.6(a)

6.2 Supercell approach

In order to check the validity of VCA and to better characterize the impact of the (Ba,Ca) substitution on the dynamics of the system we performed direct DFT calculations on the $Ba_{0.875}Ca_{0.125}TiO_3$ and $Ba_{0.50}Ca_{0.50}TiO_3$ compositions by means of supercells. Details about the atomic arrangements have been provided in Sec. 4.3.

6.2.1 $Ba_{0.875}Ca_{0.125}TiO_3$

Phonons calculations performed at the Γ-point of the cubic $Pm\bar{3}m$ $Ba_{0.875}Ca_{0.125}TiO_3$ supercell [Fig. 4.2(a)] have revealed several instabilities related to polar modes. The most unstable one,

with $\omega \simeq 169i\ cm^{-1}$, is associated to a polar distortion driven by all the Ti-atoms and the single Ca-atom against the oxygens. Ba-atoms are almost fixed as in the parent BaTiO$_3$. Therefore, Ca is polar active on the A-site already at low concentration. The different dynamics can be analyzed in terms of interatomic force constants between the A-cations and oxygens in the investigated solid solution. In fact, the A-O interaction results to be opposite if we focus on Ba or Ca atoms in line with the dynamical properties of the respective pure compounds (Table 5.3). As reported in Table 6.1, the Ba-O interaction remains dominated by repulsive forces, while the Ca-O interaction is largely dominated by the destabilizing long-range interaction. Moreover, the Ti-O interaction also appears to be indirectly affected by such atomic substitution at the A-site; in fact, from values reported in Table 6.1 in relationship with the atomic structure illustrated in Fig. 6.6(a), it is evident that interatomic force constants between the Ti cations and oxygens change alternately sign, reflecting strong competition between long- and short-range forces.

Such behavior is the result of a steric effect induced by the Ca substitution. In fact, the ionic radii of Ba and Ca are 1.61 Å and 1.34 Å respectively [186]. Thus, to accommodate the difference in size introduced by the partial substitution of Ba by Ca, a structural relaxation takes place, changing the Ti-O distances already in the reference cubic structure. Specifically, Ti atoms experiences shorter and longer bonds with the corresponding apical oxygen [Table 6.1 and Fig. 6.6(a)]. Such structural relaxation in turn strongly affects the Ti-O interatomic interaction and consequently, the dynamics behind the emergence of ferroelectricity in BaTiO$_3$ [102, 168]. In BaTiO$_3$, in fact, ferroelectricity is quickly suppressed by decreasing Ti-O distance as revealed under hydrostatic pressure [189]. In Fig. 6.4(a), in fact, we see that the overall ferroelectric instability in the cubic phase rapidly evolves as a function of the Ti-O distance and becomes localized at the Γ point before it disappears. This happens below $d_{Ti-O} \sim 1.979$ Å, which is shorter by only a 0.4% of the optimal Ti-O distance in cubic BaTiO$_3$. At the same time, the longitudinal Ti-O interatomic force constant changes sign, and so the nature of the interaction transforms from destabilizing into stabilizing, as can be seen Fig. 6.4(c). Together with this weakening of the polar instability, the relative energy difference between the two polar states with polarization along the [100] and [111] directions abruptly decreases [Fig. 6.4(b)]. In CaTiO$_3$, on the contrary, the increase of the Ti-O distance, which is now analogous to volume expansion with respect to its ideal cubic phase, keeps the overall behavior qualitatively unchanged. The corresponding Ca-O IFCs are, in fact, always positive, as we can see in Fig. 6.4(d), whereas, the Ti-O IFCs change sign also in this case, as shown in Fig. 6.4(c). However, in Sec. 5.1.2 we have seen that in CaTiO$_3$ the key interatomic interaction for the ferroelectric instability is the Ca-O one, leading to the A-site driven character of the associated polar distortion. Therefore, the persistence of this destabilizing Ca-O interaction is another key feature of the Ca substitution in the solid solution.

The intriguing manifestation of such an interplay between weakened Ti-driven ferroelectricity and emergent Ca-driven one in Ba$_{0.875}$Ca$_{0.125}$TiO$_3$ is the achievement of a quasi-degeneracy between different polar states. In fact, we analyzed five different polar states corresponding
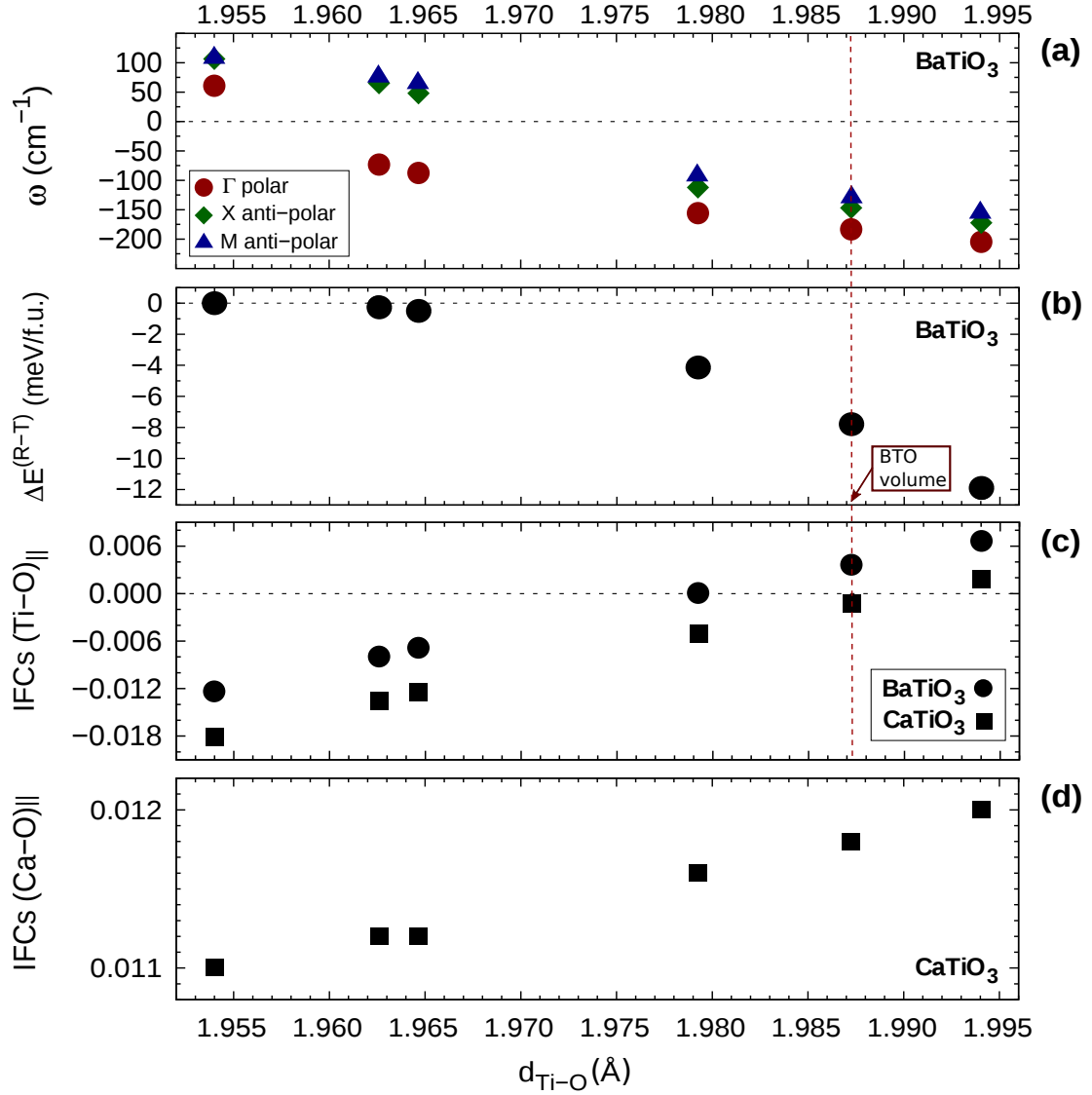
Figure 6.4: Evolution with Ti-O distance, i.e. different volume, of the dynamical properties of BaTiO₃ and CaTiO₃ in the cubic phase. (a) Phonon frequencies (in cm^{-1}) at the high-symmetry Q-points of the cubic Brillouin zone of BaTiO₃. (b) Relative energy difference (in meV/f.u.) between [111]-R and [001]-T distortions in BaTiO₃ constrained to the cubic unit cell. (c) Total Interatomic Force constants (in Ha/bohr^2) along the Ti-O coupling in BaTiO₃ and CaTiO₃. (d) Total Interatomic Force constants (in Ha/bohr^2) along the Ca-O coupling in CaTiO₃.

to the tetragonal, orthorhombic, rhombohedral, monoclinic and triclinic phases with $P4mm$, $Amm2$, $R3m$, Pm and $P1$ space-group symmetry, respectively, obtained by fully relaxing lattice vectors and atomic positions. Specifically, the average gain in energy with respect to the $Pm\bar{3}m$-cubic phase is about -20 meV/f.u. as for the parent BaTiO₃ [Fig. 6.5(a), Sec. 5.2]. Nevertheless, the maximum energy difference between the different polar phases is of about 0.5 meV/f.u. In particular, the energy of the tetragonal phase is lower than in BaTiO₃. This is likely because of the larger lattice-strain coupling effect [187, 180, 190] brought by the Ca substitution, as evident from Figs. 6.5(a,d) and Figs. 6.5(c,f). The evolution of the energy landscape when going from pure BaTiO₃ to CaTiO₃ passing through Ba₀.₈₇₅Ca₀.₁₂₅TiO₃ as
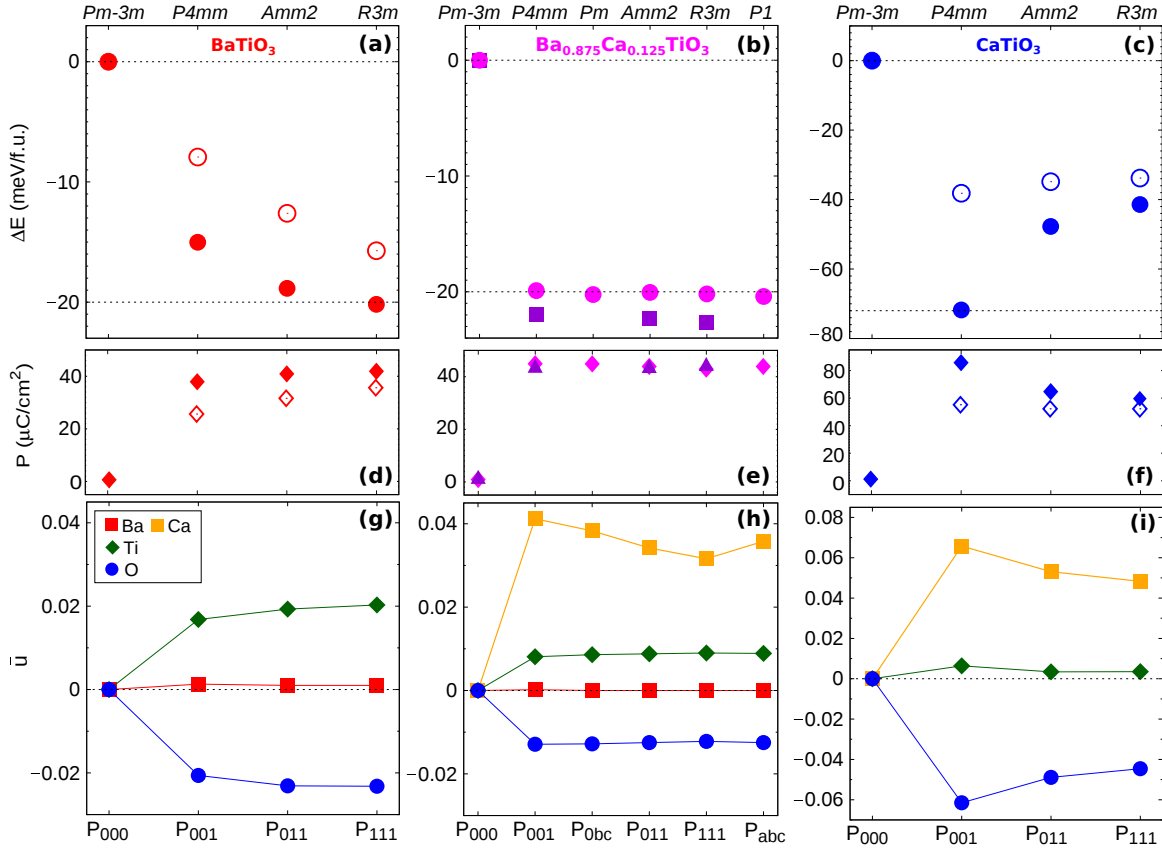
Figure 6.5: Comparison of the energetics, spontaneous polarization and atomic displacements for (a,d,g) $BaTiO_3$, (b,e,h) $Ba_{0.875}Ca_{0.125}TiO_3$ and (c,f,i) $CaTiO_3$. (Top) Energy gain (in meV/f.u.) relative to the cubic reference for states with different orientation of polarization. Closed circles represent structures relaxed both in the atomic positions and volume. In (a) and (c) open circles reproduce the energy-lowering associated to the polar distortion within fixed cubic unit cell (i.e. no strain relaxation) for $BaTiO_3$ and $CaTiO_3$ respectively. For $Ba_{0.875}Ca_{0.125}TiO_3$ (b) closed squares reproduce the energetics as obtained from Eq. 6.1. (Center) Trend of spontaneous polarization (in $\mu C/cm^2$) calculated by means of computed atomic displacements and Born effective charges, $P_{s,\alpha} = \frac{1}{\Omega}\sum_{k,\beta} Z^*_{k,\alpha\beta}\Delta\tau_{k,\beta}$ [99], for different polar states. In (d) and (f) open rhombus reproduce polarization constrained to the cubic unit cell for $BaTiO_3$ and $CaTiO_3$ respectively. For $Ba_{0.875}Ca_{0.125}TiO_3$ (e) closed triangles reproduce the polarization as obtained from Eq. 6.2. (Bottom) Evolution of average atomic displacements (in internal coordinates) relative to the center of mass of corresponding cells.

well as the effect of the strain relaxation on the energetics of the two parent compounds are reproduced in Fig. 6.5.

Interestingly, this degeneracy can be reproduced via a simple heuristic model in which the relative energy of each ferroelectric phase (E^i) and their spontaneous polarization (P^i) are expressed as a linear combination of the corresponding quantities of the parent compounds:

$$E^i(x) = (1-x)E^i_{BTO} + xE^i_{CTO} \tag{6.1}$$

$$P^i(x) = (1-x)P^i_{BTO} + xP^i_{CTO} \tag{6.2}$$

where x is the Ca concentration. This simple model exploits the reversed sequence of ferro-electric states displayed by the two parent compounds. Noteworthy, the strain effect has to

be included to properly reproduce the degeneracy of phases. The obtained from this model is shown in Fig. 6.5(b,e).

Going back to the specific results from supercell calculations for $x = 0.125$, it is worthy to emphasize the emergence of the triclinic and monoclinic structures absent in the energetics of the parent compounds. Specifically, the triclinic-$P1(C_1)$ phase displays polarization P_{abc} nearly between the [001]-[111] direction of the original cubic structure ($P_a/P_c \simeq 0.53$, $P_b/P_c \simeq 0.48$) and the monoclinic-$Pm(C_1^s)$ phase displays polarization P_{0bc} in between the [001]-[011] direction ($P_b/P_c \simeq 0.53$) [Figs. 6.5(b,e)]. Furthermore, the spontaneous polarization and related atomic distortions are essentially the same for all the ferroelectric phases as we show in Figs. 6.5(e,h) ($P \sim 39\mu C/cm^2$ as computed via the Berry phase [191]). Together with the the quasi-degeneracy of the energies, these results disclose a remarkably isotropic energy landscape. We also note that, compared to the parent BaTiO₃, the relative displacements of both Ti and O atoms are reduced for $x = 0.125$, which is more pronounced for the Ti atoms, while the current distortion also contains a sizable displacement of Ca [see Fig. 6.5(h)]. Such behavior has been actually observed experimentally in Refs. [193, 194]. This reduction of the Ti and O displacements contributes to reduce the overall anisotropy of the system. Therefore, the specific dynamics in $Ba_{0.875}Ca_{0.125}TiO_3$ is a clear manifestation of the appearance of a A-driven character of the distortion accompanied by the reduction of the B-driven one.

Additionally, we calculated the d_{ij} coefficients of the piezoelectric tensor in the stable $R3m$-phase. The d_{33} component, parallel to the polarization direction, remains unchanged with respect to BaTiO₃, while the d_{11} and d_{15} components, transversal to the polar axis, are considerably enhanced. Specifically they are: $d_{33} \simeq 15$, $d_{11} \simeq 344$ and $d_{15} \simeq 1458$ in pC/N. This behavior can be related to the increase of the stress-free dielectric response along the corresponding directions due to the softening of the polar modes. In fact, the lowest-frequency polar mode in the stable $R3m$-phase is of about 61 cm⁻¹ instead of 169 cm⁻¹ in BaTiO₃.

6.2.2 Ba₀.₅Ca₀.₅TiO₃

First result in $Ba_{0.5}Ca_{0.5}TiO_3$ [Fig. 4.2(b-d)] is the preference of an ordered configuration composed by alternating layers of the same type of A-cations with respect to a columnar and rocksalt ordering. The relative energy gain of the high-symmetry columnar and layered configurations with respect to the rocksalt one is about -35.5 meV/f.u. and -81.4 meV/f.u., respectively.

Then, as previously, we performed DFPT calculations on the three high-symmetry reference supercells. All three configurations display several instabilities. In all of them the most unstable mode corresponds to a polar distortion driven by both the Ti and Ca atoms like in $Ba_{0.875}Ca_{0.125}TiO_3$, but with an average major contribution from calcium. The phonon frequency associated to that mode is $\omega \simeq 141i$ cm^{-1} in all three cases. Additionally, AFD modes related to oxygen rotations become unstable. However, the energy gain carried to the system

Ba$_{0.50}$Ca$_{0.50}$TiO$_3$					
VCA			**1x1x2 CELL**		
Atoms		Total	Atoms		Total
$B-O_1$			Ti-O$_1$	$(\parallel)$	-0.009
d=1.960 Å			d=1.956 Å	$(\perp)$	-0.019
	$(\parallel)$	-0.011	Ti-O$_2$	$(\parallel)$	-0.047
	$(\perp)$	-0.020	d=1.890 Å	$(\perp)$	-0.017
			Ti-O$_3$	$(\parallel)$	+0.010
			d=2.011 Å	$(\perp)$	-0.019
$A-O_1$			Ba-O$_1$	(xx')	-0.001
d=2.772 Å			d=2.837 Å	(yy')	-0.005
				(zz')	-0.011
			Ba-O$_3$	(xx')	-0.005
			d=2.765 Å	(yy')	-0.005
	(xx')	+0.002		(zz')	-0.011
	(yy')	-0.005	Ca-O$_1$	(xx')	+0.010
			d=2.690 Å	(yy')	-0.006
	(zz')	-0.011		(zz')	-0.012
			Ca-O$_2$	(xx')	+0.011
			d=2.765 Å	(yy')	-0.005
				(zz')	-0.012

Table 6.2: Interatomic force constants for Ba$_{0.50}$Ca$_{0.50}$TiO$_3$ within VCA and the layered supercell. Units are in Ha/bohr^2. Directions xx' $(\parallel)$, yy' $(\perp)$ and zz' $(\perp)$ refer to local coordinates system of the different pairs of atoms. Distances (in Å) between the selected atoms are also reported. Atoms' notation in the second column is consistent with Fig. 6.6(b)

by the condensation of the latter distortions alone is lower than the one coming from the polar distortions, that determine the ground-state.

Accordingly, the most stable polar phase results to be the $P2mm$-structure with the polarization along the [100] direction of the layered atomic arrangement. The associated P_s is of about 51 $\mu C/cm^2$ and it is considerably greater than the one calculated in $P4mm$-BaTiO$_3$, that is $P_s \simeq 34 \ \mu C/cm^2$. Moreover, in order to see eventual effects of the atomic configuration on the energy competition between different polar states, we condensed different patterns of polar distortions in the three arrangements. The associated energy landscape is quite spread as reported in Fig. 6.6(c). It results that, for $x = 0.50$, the system prefers a state with only "one-component" polarization independently of the atomic configuration. The $R3m$-like state with polarization along the [111] pseudo-cubic direction is largely penalized.

Also in this case, changes in the dynamical properties (i.e. substantial contribution from Ca-atoms to the polar distortion and the appearance of unstable AFD modes) and in the energetics of the polar phases can be analyzed in term of interatomic force constants. As made clear in Table 6.1 and Table 6.2, the main features are the same as the ones described for the $x = 0.125$ Ca-concentration. However, the higher concentration of calcium induces shorter Ti-O
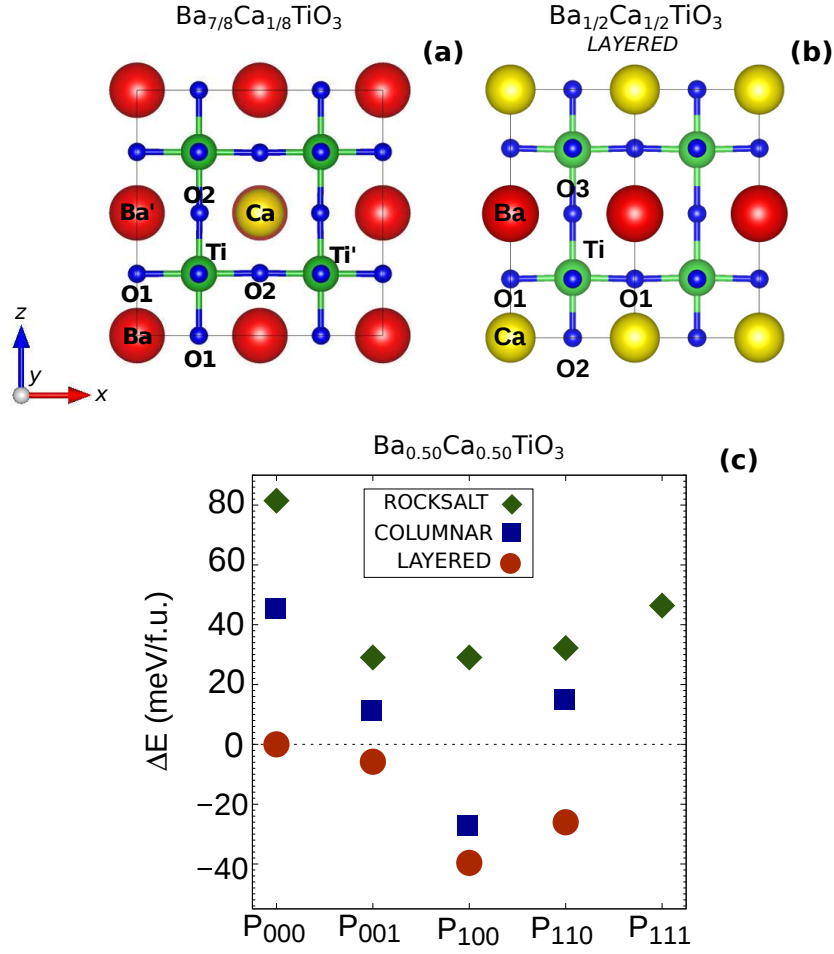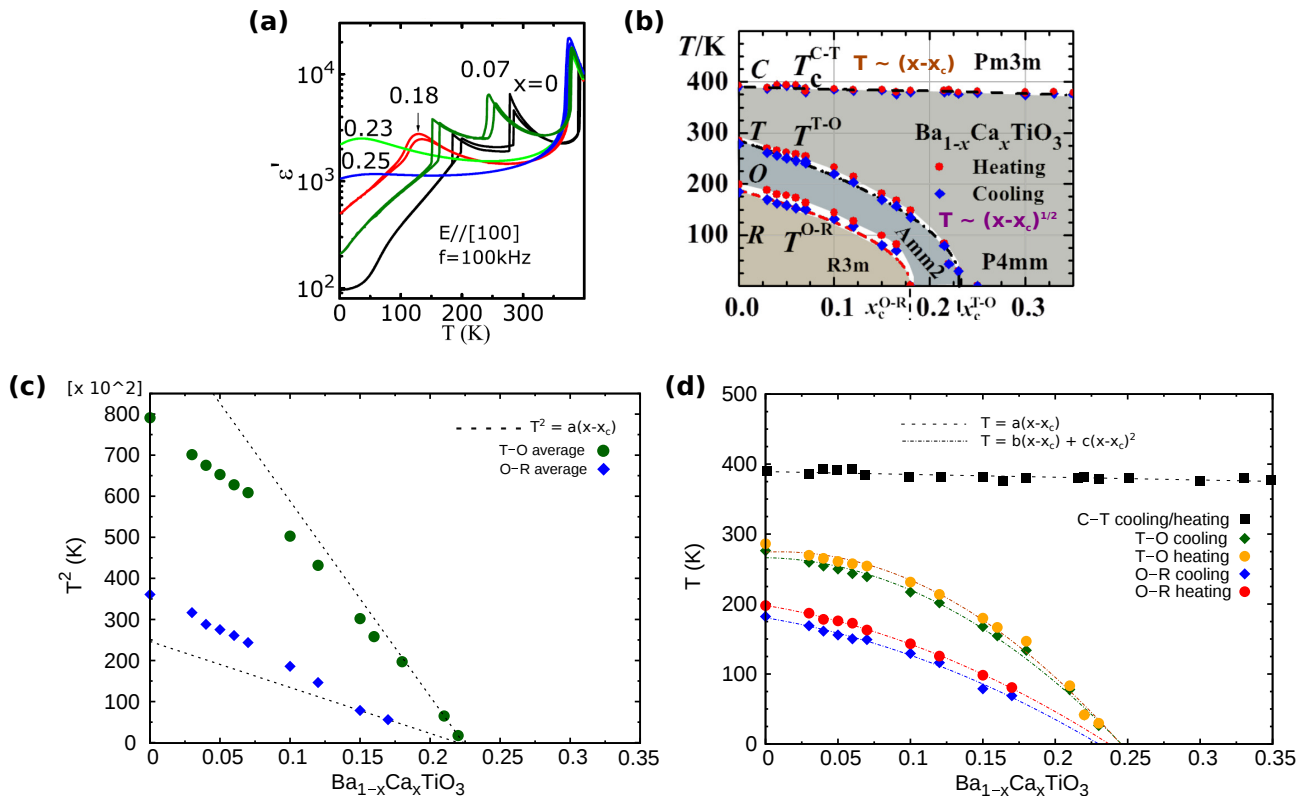
Figure 6.6: Schematic representation of the atomic arrangement in $Ba_{0.875}Ca_{0.125}TiO_3$ (a) and in layered-$Ba_{0.5}Ca_{0.5}TiO_3$(b). Direction along y is equivalent to the x-one. Labels help the visualization of the main atomic pair analyzed in Tables 6.1 and 6.2. (c): Energy gain (in meV/f.u.) with respect to the highy-symmetry $P4mmm$-layered structure for different optimized polar states in the $Ba_{0.5}Ca_{0.5}TiO_3$ supercells. The x-axis notation refers to the direction of the components of polarization.

distances, i.e. more contracted $[TiO_6]$-octahedra. On the one hand, this produces the overall weakening of the long-range interaction between Ti and O atoms in favor of repulsive forces hindering the B-driven polar distortion. Therefore, the polar instability remains mostly Ca-driven, promoting "tetragonal-like" polar states. Accordingly, the result of such unbalanced competition between Ti- and Ca-driven polar distortion is that the quasi-degeneracy of the ferroelectric phases found out in the low Ca-concentration case is lost and the energy landscape becomes highly anisotropic again, $CaTiO_3$-like. On the other hand, the stiffness of oxygens is reduced in the direction perpendicular to the Ti-O bonds favoring the appearance of oxygen rotations. In fact, the values of the "on-site" oxygens force constants in the solid solution are in between the ones of pure $BaTiO_3$ and $CaTiO_3$ (Table 5.1).

Comparison with experimental phase diagram

It is worth noting that our calculations reproduce qualitatively the $T = 0$ K experimental phase diagram reported by Fu *et al.* in Refs. [184, 195] [Fig. 6.7(b)]. Specifically, at $T = 0$ K, $Ba_{1-x}Ca_xTiO_3$ is experimentally found to be in the rhombohedral $R3m$ phase for $x \sim 0.18$ and in the tetragonal $P4mm$ phase for $x \sim 0.23$. The orthorhombic $Amm2$ phase has been assigned to the intermediate $0.18 \lesssim x \lesssim 0.23$ interval which, in our calculations, appears to be virtually zero [see Figs. 6.5(a)-(c)]. However, we note that in the measurements of the dielectric constant reported in Ref. [195] [Fig. 6.7(a)], it is observed very broad low-temperature features for $x = 0.18$ that can perfectly result from the overlap of the two hysteretic anomalies, having thus still three peaks in total. Additionally, the authors have obtained the critical concentrations x_c(T=0 K) by invoking a "quantum" scaling, of the type $T \propto (x - x_c)^{1/2}$, and fitting the data to this scaling over all the temperature interval from 0 to 300 K of the phase diagram [Fig. 6.7(b)]. This scaling, however, is an asymptotic scaling that can be expected to be valid in the ultra low-temperature limit only, and not above ~ 100 K [197, 198]. Moreover, they ignore the hysteretic behavior of the experimental data (see the temperature dependence of the dielectric constant ϵ' in Fig. 6.7(a)), revealing the first-order character of the transition, that does not allow an universal scaling.

To test the trend $T \propto (x - x_c)^{1/2}$, we have plotted $T^2 \propto (x - x_c)$ as function of x by taking into account in the fit only the data below ~ 100 K. The result shown in Fig.6.7(c) is that such a trend is not representative of all the data. Then, if we simply extrapolate their results without assuming any specific scaling, we find that these results are also compatible with the three polar phases meeting together at $T = 0$ K, as shown in Fig. 6.7(d). The fit has been done on data extracted from the phase diagram reported in Ref. [184] by excluding the last point at $T < 5$ K. Consequently, on the one hand the quasi-degeneracy of the ferroelectric phases found out by our first-principles calculations is compatible with the direct extrapolation of this data to $T = 0$ K. On the other hand, the disagreement in the quantitative prediction of the specific concentration, at which such a convergence occurs, is likely due to the relative small size of our $2 \times 2 \times 2$ supercells, not considering explicitly the effect of disorder. Additionally, the energetics obtained by our specific calculations for the case $x = 0.50$ based on such supercells [Fig. 6.6], are again fully compatible with the experimentally observed stabilization of the tetragonal phase over the orthorhombic and rhombohedral ones for greater Ca-concentration. Nevertheless, the quantitative reproduction of the experimental data, as well as the discussion of quantum critical effects, was not the scope of our study aimed instead to the identification of the microscopic mechanisms leading to this quasi-degeneracy.

Figure 6.7: (a) Temperature dependence of the dielectric constant (ϵ') of Ba$_{1-x}$Ca$_x$TiO$_3$ crystals. (b) Phase diagram of Ba$_{1-x}$Ca$_x$TiO$_3$ derived from dielectric measurements. Blue rhombus and red circles indicate the cooling and heating processes, respectively. From Refs. [184, 195]. (c) and (d) fit of the trend of the transition temperature T as a function of the concentration x: (c) plot of T^2 fitted via the linear behavior $a(x - x_c)$ to test the trend $T \propto (x - x_c)^{1/2}$ as assumed by Fu *et al.* in Refs. [184, 195] for the T-O and O-R phase transitions; (d) fitting of T via the classic trend $(x - x_c)$ for the C-T transition, while via a generic trend $a(x - x_c) + b(x - x_c)^2$ for the T-O and O-R transitions to extrapolate x_c(T=0 K). a and b are fitting parameters. Data for fitting have been extracted from the phase diagram (b) reported in Ref. [184].

6.3 VCA vs SUPERCELL approaches

By comparing results from supercell-based calculations with the ones from VCA, it seems that the latter approach is successful to provide an average and qualitative identification of the main changes occurring in the (Ba,Ca)TiO$_3$ solid solutions. However, it cannot provide a proper description of the microscopic mechanism behind properties. The reason of such a limitation is that, by construction, VCA considers all A atoms as equivalent and forces them to behave similarly while, in fact, Ba and Ca want to adopt different behaviors. The importance of considering the actual local cations is clear by comparing the quantities reported in Tables 6.1 and 6.2, where we clearly see that different results are obtained depending on the method. In fact, as discussed above, evolutions in the dynamics as well as in the energy landscape are strongly related to the presence of calcium that directly interacts with the oxygens and, indirectly, affects the Ti-O interaction via local changes of the structure. These effects have a purely steric nature related to the presence of Ca atoms. Strong changes in the dynamical properties as

steric effects induced by the addition of Ca have also been found in (Ba,Ca)ZrO$_3$ [192].

However, the progressive weakening of ferroelectricity, within VCA, is not representative of the real behaviour: the actual weakening of the Ti-driven ferroelectricity due to decreasing volume is progressively compensated by the Ca-driven ferroelectricity. In fact, the inversion in the sequence of polar phases when going from BaTiO$_3$ to CaTiO$_3$ appears already at $x = 0.50$ within the supercell, while it is expected for $x \geq 0.9$ within VCA. Additionally, an opposite trend of the spontaneous polarization is also obtained within the two approaches: decreasing values for larger x within VCA, while increasing ones within the supercells.

As a global result, the partial success of VCA in detecting changes in the dynamical properties when progressively substituting Ba by Ca is due to two main factors: (i) the volume contraction induced by increasing Ca concentration allows to detect the weakening of the B-driven ferrolectricity; (ii) possible inaccuracies in reproducing the orbital hybridization within VCA are not primary here, as the most relevant hybridization mechanism is only related to the O p and Ti d states, that are not concerned by the VCA mixing procedure. Nevertheless, the trends and microscopic mechanisms involved as predicted by means of supercells calculations are better in line with experimental observations [184, 193]. This remark confirms that, in order to provide a proper first-principles characterization of (Ba,Ca)TiO$_3$, VCA-based approaches can provide some trend, but are not appropriate to explain the underlying physics; for the latter, supercells-based calculations taking explicitly into account the different nature of the cations are more suitable.

Chapter 7

Ba(Ti,Zr)O$_3$ solid solutions

Ba(Ti,Zr)O$_3$ (BTZ) solid solutions involve the homovalent substitution between Ti^{4+} and Zr^{4+}, that are nevertheless quite different atoms both for the ionic radii (0.605 Å and 0.72 Å respectively [186]) and the electronic configuration (Ti 4s^2 3d^2 and Zr 4d^2 5s^2), which enters the hybridization mechanism responsible of the ferroelectricity in BaTiO$_3$.

The first experimental investigation of the phase diagram of the BaTiO$_3$-BaZrO$_3$ binary system dates back to the 1956 with the work of Kell and Hellicar [160], reporting the abrupt effect of Zr-concentration on the decreasing of the Curie point for the three ferroelectric phases of BaTiO$_3$. Subsequently, other solid experimental investigations came out in the late '90s, when Ravez et al. in Refs. [199, 200] provided a clear distinction of phases in the BaTi$_{1-y}$Zr$_y$O$_3$ ceramics diagram: classical ferroelectric BaTiO$_3$-like for $0.00 \leq y \leq 0.10$, only one ferroelectric-paraelectric transition observed in the range $0.10 \leq y \leq 0.27$ and relaxor ferroelectric behavior for $0.27 < y \leq 0.42$. Then, in 2004, Simon et al. also investigated the crossover from a ferroelectric to a relaxor state in lead-free solid solutions in Ref. [201], confirming that beyond a definite concentration y, BTZ ceramics show relaxor properties. For BaTi$_{0.80}$Zr$_{0.20}$O$_3$ only one resonance of the permittivity at the ferroelectric-paraelectric T_C of about 315 K is observed, whereas for $y = 0.35$ the dielectric anomaly is broad and frequency-dependent as a function of temperature. Moreover in Ref. [202], they provide an EXAFS study of BTZ systems and conclude that BTZ is relaxor and the average crystal structure is cubic ($Pm\bar{3}m$ space group) in the range $0.25 \leq y \leq 0.50$. In addition, in a complementary work on BCTZ [203], the X-ray diffraction has revealed (110) peaks in BaTi$_{0.80}$Zr$_{0.20}$O$_3$ ceramic but a weak tetragonality (i.e. $a/c \sim 1$), that means closeness to the cubic phase. However, no experimental data on single crystal samples are available for direct comparison with ab-$initio$ results.

As for the previous case of (Ba,Ca)TiO$_3$, we first investigate the Ba(Ti,Zr)O$_3$ system by means of the virtual crystal approximation. Then, we go beyond by using supercells-based calculations.

7.1 VCA approach

7.1.1 Lattice parameters

We first report the trend of the lattice parameter of the $Pm\bar{3}m$-cubic phase as a function of Zr-composition. Because of the bigger volume of $BaZrO_3$ with respect to $BaTiO_3$ (Table 4.1), the trend is monotonically increasing with the amount of zirconium and the agreement with the linearity of the Vegard's law is quite satisfactory [Fig. 7.1(a)]. Contrariwise, because of the bigger ionic radius of Zr than Ti, the tolerance factor[1] decreases without going below 1, that is the value for pure $BaZrO_3$, as reported on top of Fig. 7.1.

7.1.2 Dynamical properties

We focus on the dynamics by looking at the evolution of the lowest phonon frequencies at the high-symmetry points of the cubic Brillouin zone. Calculations have been performed on the VCA-optimized $Pm\bar{3}m$ structure. It results that the main effect of the Zr-doping is to abruptly stabilize the cubic phase, as clear from Fig. 7.1(b). In fact, already in the Ti-rich region, i.e. $y > 0.10$, the original polar instability vanishes and an AFD unstable mode $BaZrO_3$-like appears at the R-point only for $y \geq 0.90$. The reason behind such abrupt weakening of ferroelectricity in the BTZ "virtual-system" at low y-concentration can be traced back to abrupt changes in the type of interaction between the virtual cation at the B-site and the oxygens. In fact, the total IFC along the B-O direction is of about -0.001 Ha/bohr^2 at $y \geq 0.05$. Therefore, the change of sign with respect to the corresponding interaction in pure $BaTiO_3$ (Tables 5.3) means that the Zr-substitution strongly favors short-range repulsive forces.

Differently from BCT systems, it is not possible to relate such behaviour to the evolution of the tolerance factor or to simple volumetric reasons. In fact, in line with the properties of the two parent compounds, t remains larger than one and the volume increases for each intermediate composition. The main mechanism involved here is the weakening of the Ti-O interaction when "virtually" introducing Zr on the same B-site. This corresponds to either direct changes in the O $2p$ and B d hybridization mechanism from the electronic perspective or breaking correlated Ti-O chains necessary to sustain ferroelectricity in $BaTiO_3$ from the lattice dynamics. In fact, we have already seen in Sec.5.1.4, that the Zr-O interaction in $BaZrO_3$ is strongly repulsive. Moreover, differently than the role played by $CaTiO_3$ in BCT, no contribution from the A-site is observed, as the Ba-O interaction is too weak to sustain alone a polar instability in BTZ.

As a consequence, it is finally not surprising that the "virtual"-BTZ system does not display any instabilities for a very large range of composition.

---

[1]also in this case, we defined an average radius for the B-cation as $\overline{r_B} = (1-y)r_{Ti} + (y)r_{Zr}$
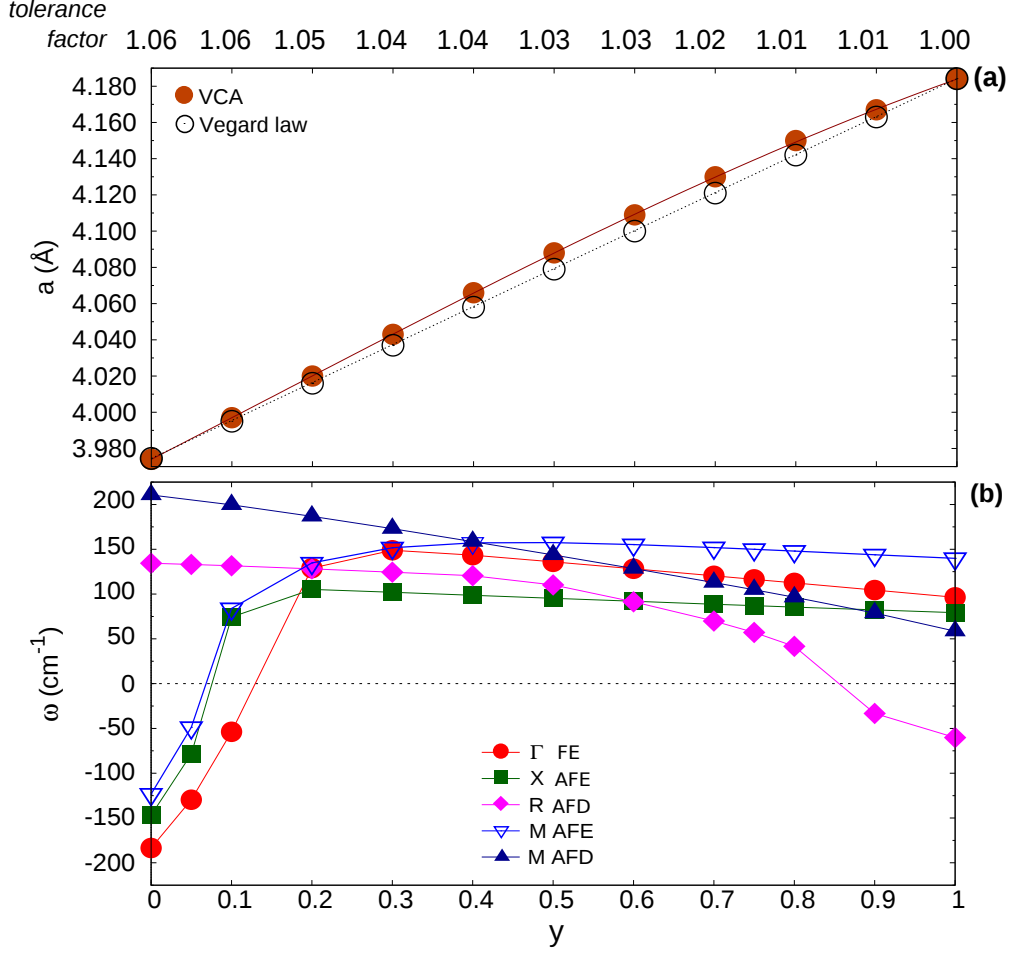
Figure 7.1: (a) Evolution as a function of y-composition in BaTi$_{1-y}$Zr$_y$O$_3$ of the cubic lattice parameter a_{cell} (in Å) relaxed within VCA. Vegard's law has been built on the theoretical values of the cubic BaTiO$_3$ and BaZrO$_3$ reported in Table 4.1: $a(y) = (1-y)a_{BTO} + (y)a_{BZO}$. (b) Trend of the lowest phonon frequencies (in cm^{-1}) at the high-symmetry points of the simple cubic Brillouin zone as a function of different y-compositions.

7.1.3   Energy landscape

In line with the drastic changes of the dynamical properties in BTZ predicted by VCA, the energy difference both between the three polar phases and with respect to the cubic one is abruptly reduced, as shown in Fig. 7.2. In fact, the energy competition is within 0.1 meV/f.u. at $y = 0.10$ and beyond this concentration no stable or metastable polar phases are allowed within VCA.

7.1.4   Polarization and piezoelectric response

After identifying the abrupt weakening of ferroelectricity in the BTZ "virtual-system", we now evaluate the associated effect on the piezoelectric response. Therefore, we calculate the spontaneous polarization P_s and the piezoelectric coefficients d_{ij} for the stable phase, that is the $R3m$-phase for $y = 0.05$ and 0.10 (Fig.7.2). Also in this case, as we are mostly interested in the qualitative trend of these properties as a function of Zr-doping, we report values normalized

to those of $R3m$-BaTiO$_3$.

In Fig. 7.3 we report values of P_s calculated both via Berry phase (blue circles) and Born
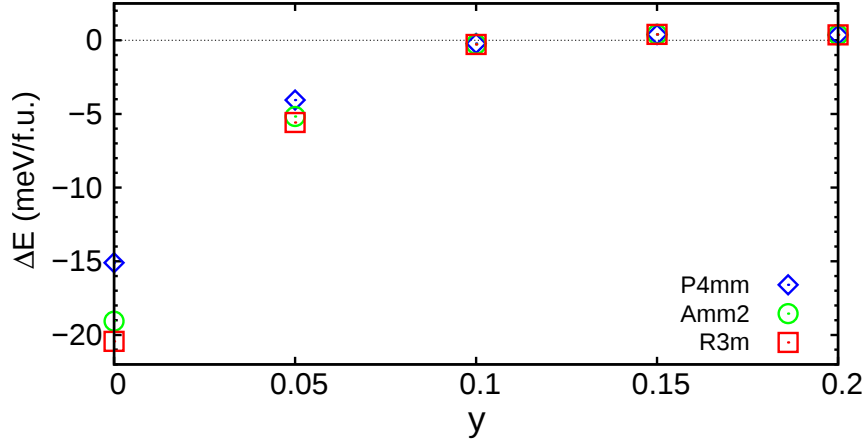

Figure 7.2: Zoom on the evolution of the energy gain (in meV/formula unit) of the three polar structures relative to the cubic phase as a function of y-composition in the Ti-rich region within VCA.
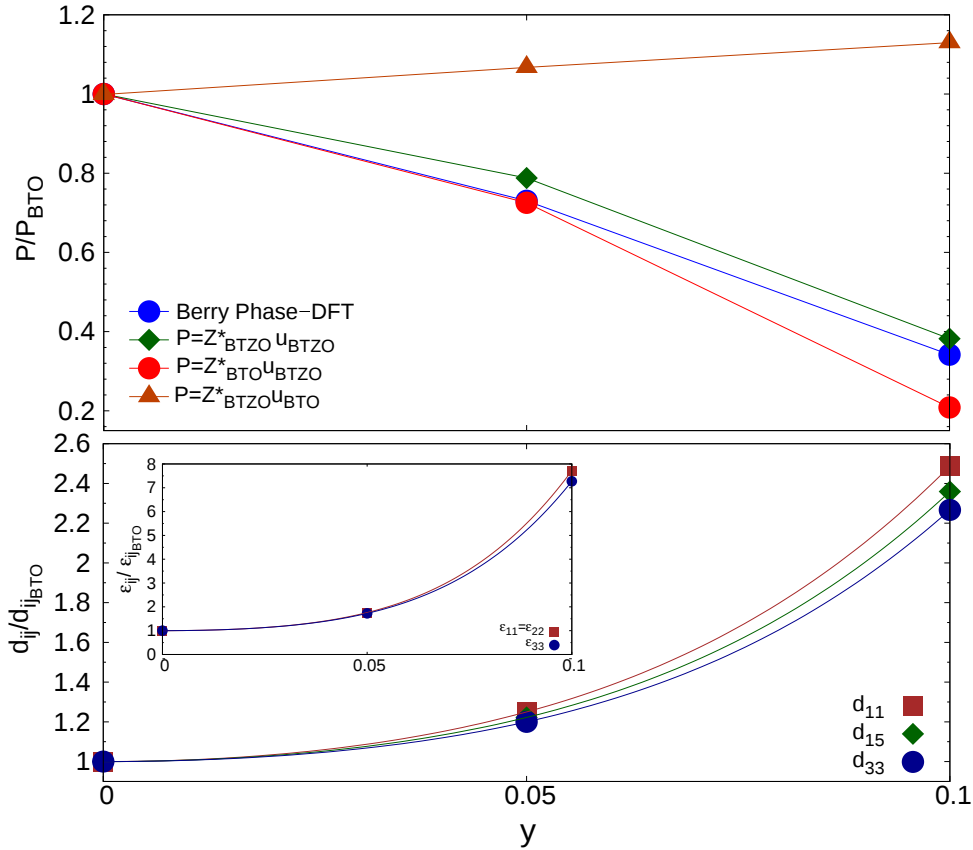

Figure 7.3: Evolution of polarization, stress-free dielectric and piezoelectric coefficients in the rhombohedral-R3m phase as a function of y-composition in BaTi$_{1-y}$Zr$_y$O$_3$ within VCA. Values are normalized to the ones of $R3m$-BaTiO$_3$: $P_s^{BTO} \simeq 38~\mu C/cm^{-2}$; $d_{11}^{BTO} \simeq 76$, $d_{15}^{BTO} \simeq 270$ and $d_{33}^{BTO} \simeq 15~pC/N$; $\varepsilon_{11}^{BTO} \simeq 208$ and $\varepsilon_{33}^{BTO} \simeq 11$. Upper panel: variation of the polarization as directly computed via Berry-phase calculations (blue closed circles) and via Born effective charges to disentangle the contribution of varying atomic charges and displacements. Lower panel: trend of the d_{ij} coefficients and stress-free dielectric response ε_{ij}.

effective charges (green rhombus). This is to be compared with the same calculations for BCT in Fig 6.3. In line with the strong weakening of the polar instability, P_s is drastically reduced by the Zr-doping. Similarly to BCT, from the further analysis of the distinguished contribution from effective charge variation and atomic displacements, it results that the evolution of P_s has to be widely ascribed to largely reduced atomic motions. However, by looking at $y = 0.10$, it is important to note that there is a disagreement between the value of polarization by fixing the Born effective charges to that of pure $R3m$-BaTiO$_3$ (red circles) or to the ones of $R3m$-BTZ "virtual-system" (green rhombus) as the Zr-doping also affects the Born effective charges. In fact, we have already shown that the Z^* associated to Zr is less anomalous than the one of Ti (Table 5.2). Therefore, the average effective charge associated to the "virtual" B-cation is also reduced with increasing Zr-concentration. This is an important warning about the ability of VCA in describing the properties arising from the mixing of Zr and Ti on the B-site, as they have quite different electronic properties (see Sec.7.3 below).

Such decrease of P_s remains compatible with an increase of piezoelectricity. In fact, the huge increase of dielectric response, ε_{ij}, associated to the drastic softening of the polar mode, largely compensates the decrease of P_s. This results in the enhancement of the piezoelectric response with respect to pure BaTiO$_3$, as reported in Fig. 7.3. Accordingly, the values of the lowest-frequency polar mode in the stable $R3m$-phase evolve like 169, 146, 69 (in cm^{-1}) for $y = 0.00, 0.05$ and 0.10, respectively.

As we see, the trends obtained from VCA are in reasonable agreement with the experimental observations. However, to understand the actual impact of the partial substitution of Ti with Zr on the dynamics of the system at the local level, supercells-based calculations are necessary.

7.2 Supercell approach

In this Section, we investigate the dynamical properties of BaTi$_{0.875}$Zr$_{0.125}$O$_3$ and BaTi$_{0.50}$Zr$_{0.50}$O$_3$ supercells. Structural details are provided in Sec. 4.3

7.2.1 BaTi$_{0.875}$Zr$_{0.125}$O$_3$

BaTi$_{0.875}$Zr$_{0.125}$O$_3$ supercell [Fig. 4.2(e)] hosts several instabilities in the cubic $Pm\bar{3}m$ phase, all related to ferroelectric and antiferroelectric distortions. The most unstable, with $\omega \simeq 214i\ cm^{-1}$, is a polar mode mostly related to the opposite motion of Ti and O, while the Zr atom slightly moves in the same direction as the oxygens. The difference in these relative displacements affects the neighboring atom lying on the polar direction, that slightly moves with the oxygens as well. This means that, according to the labels indicated in Fig. 7.4(a), if the polar distortion is, for instance, along the x direction, Ti$_1$ slightly off-centers with Zr in the same direction as the oxygens, but opposite to the other Ti-atoms. Ba-atoms are almost fixed as in
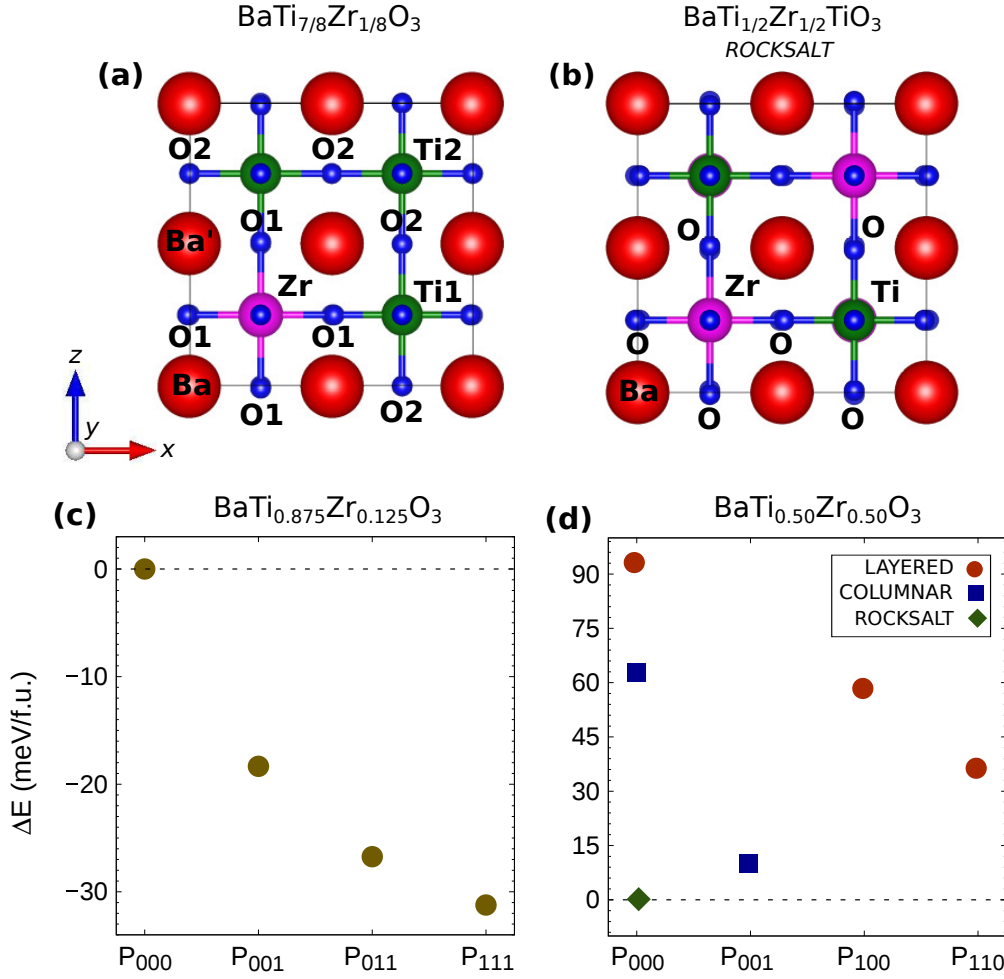
Figure 7.4: Schematic representation of the atomic arrangement in $BaTi_{0.875}Zr_{0.125}O_3$ (a) and in rocksalt-$BaTi_{0.50}Zr_{0.50}O_3$(b). Labels help the visualization of the main atomic pair analyzed in Tables 7.1 and 7.3. Energy lowering (in meV/f.u.) with respect to the high-symmetry $Pm\bar{3}m$ phase for $BaTi_{0.875}Zr_{0.125}O_3$ (c) and with respect to high-symmetry rocksalt-$Fm\bar{3}m$ configuration for $BaTi_{0.50}Zr_{0.50}O_3$ (d) as a function of different optimized polar states by means of supercells. The x-axis notation refers to the direction of the components of polarization.

the parent $BaTiO_3$. Such different dynamics is made clear when looking at the interatomic force constants reported in Table 7.1. In fact, the original destabilizing Ti-O interaction of $BaTiO_3$ is not preserved for each direction in the system. The Ti-atoms having Zr as first-neighbors experience a strong repulsive Ti-O interaction along the O-Zr-O-Ti-O chain direction, while the long-range forces remain the major ones along the other directions as well as for the other Ti-atoms. This is strongly ascribed to the "chain-like" character of the polar instability of $BaTiO_3$, as discussed in Sec. 5.1.1: the polar instability requires a minimum number of correlated Ti-O displacements [168] that, however, are prevented along the chain containing Zr. In fact, according to the properties of $BaZrO_3$ described in Sec. 5.1.4, the Zr-O interaction remains strongly repulsive also in this Ti-rich solid solution. However, along the preserved O-Ti-O-Ti-O chains, the long-range interaction is even indirectly strengthened by the Zr-presence. In fact, the bigger size of Zr (i.e. of the $[ZrO_6]$-octahedral volume) makes the Ti-O bond's length perpendicular

$\mathbf{BaTi_{0.875}Zr_{0.125}O_3}$									
VCA					**2x2x2 CELL**				
Atoms		Total	DD	SR	Atoms		Total	DD	SR
$A-A'$	$(\parallel)$	-0.011	-0.006	-0.005	Ba-Ba'	$(\parallel)$	-0.012	-0.006	-0.0061
d=3.997 Å	$(\perp)$	+0.004	+0.003	+0.001	d=4.043 Å	$(\perp)$	+0.004	+0.003	+0.001
$B-B'$					Ti_1-Ti_2	(xx')	-0.068	-0.038	-0.029
d=3.997 Å	$(\parallel)$	-0.067	-0.037	-0.030	d=4.002 Å	(yy')	+0.008	+0.018	-0.010
	$(\perp)$	+0.009	+0.018	-0.011		(zz')	+0.008	+0.019	-0.011
					Ti_1-Zr	(xx')	-0.069	-0.034	-0.034
					d=4.002 Å	(yy')	+0.008	+0.019	-0.011
						(zz')	+0.008	+0.019	-0.011
$A-B$					Ba-Ti_1	(xx')	-0.028	-0.022	-0.007
d=3.461 Å	$(\parallel)$	-0.030	-0.023	-0.008	d=3.478 Å	(yy')	+0.014	+0.010	+0.003
	$(\perp)$	+0.014	+0.011	+0.003		(zz')	+0.013	+0.011	+0.002
					Ba-Zr	(xx')	-0.031	-0.020	-0.011
					d=3.502 Å	(yy')	+0.013	+0.011	+0.002
						(zz')	+0.013	+0.011	+0.002
$B-O_1$					Ti_1-O_1	$(\parallel)$	-0.032	+0.239	-0.271
d=1.998 Å					d=1.929 Å	$(\perp)$	-0.015	-0.052	+0.037
					Zr-O_1	$(\parallel)$	-0.039	+0.199	-0.238
	$(\parallel)$	-0.009	+0.229	-0.238	d=2.073 Å	$(\perp)$	-0.013	-0.040	+0.027
	$(\perp)$	-0.020	-0.045	+0.025	Ti_1-O_2	(xx')	+0.013	+0.239	-0.226
					d=2.012 Å	(yy')	-0.023	-0.039	+0.016
						(zz')	-0.021	-0.046	+0.025
					Ti_2-O_2	$(\parallel)$	+0.003	+0.244	-0.241
					d=1.990 Å	$(\perp)$	-0.021	-0.043	+0.022
$A-O_1$	(xx')	-0.001	+0.013	-0.014	Ba-O_1	(xx')	+0.000	+0.012	-0.0113
d=2.826 Å	(yy')	-0.005	-0.006	+0.002	d=2.860 Å	(yy')	-0.010	-0.015	+0.005
	(zz')	-0.011	-0.016	+0.005		(zz')	-0.004	-0.006	+0.002

Table 7.1: Interatomic force constants from VCA and supercell-based calculations for BaTi$_{0.875}$Zr$_{0.125}$O$_3$. Units are in Ha/bohr^2. Directions xx' ($\parallel$), yy' ($\perp$) and zz' ($\perp$) refer to local coordinates system of the different pairs of atoms. Distances (in Å) between the selected atoms are also reported. Atoms' notation in the second column is consistent with Fig. 7.4(a).

to the O-Zr-O-Ti-O chain direction longer than in pure BaTiO$_3$. This mechanism locally favors the long-range interaction. Accordingly, the "on-site" force constants tensor associated to the Ti-atoms adjacent to Zr are anisotropic: by referring to Ti1 of Fig. 7.4(a), the "on-site" terms are $(+0.247, +0.132, +0.132)$ Ha/bohr^2. Therefore, they are much more stiffer along the Zr-direction, while softer along the transversal directions than in BaTiO$_3$ (see Table 5.1). The other Ti-atoms display a slightly anisotropic tensor, but similar to the one in BaTiO$_3$: by referring to Ti2 of Fig. 7.4(a), values are $(+0.162, +0.151, +0.162)$ Ha/bohr^2. In contrast, Zr

displays an isotropic tensor BaZrO$_3$-like with diagonal values of about $+0.229$ Ha/bohr^2, as it experiences the same interactions in each direction. Concerning Ba at the A-site, the dynamics is the same as in pure BaTiO$_3$. In fact, the A-O interatomic force constant is close to zero along parallel direction of the coupling meaning that Ba distortion does not lead ferroelectricity in BaTi$_{0.875}$Zr$_{0.125}$O$_3$. The A-B interaction is also similar to the one in the two parent compounds reported in Table 5.3.

Such complex dynamics results in slightly reduced total polarization and more spread energy landscape with respect to the case of the parent BaTiO$_3$. On one hand, the calculated spontaneous polarization is of about 28 $\mu C/cm^2$ and 35 $\mu C/cm^2$ for the $P4mm$ and $R3m$ phases, respectively, while it is of about 34 $\mu C/cm^2$ and 38 $\mu C/cm^2$ for the corresponding phases in pure BaTiO$_3$. This has to be assigned to the local depolarizing contribution arising from the O-Zr-O-Ti-O chain. On the other hand, the energy gain of the three polar phases relative to the cubic phase is higher than in BaTiO$_3$ and it appears much more pronounced for the $Amm2$ and $R3m$ phases as reported in Fig. 7.4(c). This effect traces back to the overall volume increase, that further favors the rhombohedral phase.

In line with the higher anisotropy of the energy landscape and reduced polarity of the system, the piezoelectric response results then reduced than in BaTiO$_3$. Specifically, we calculated the d_{ij} coefficients of the piezoelectric tensor in the stable $R3m$-phase. Values are: $d_{33} \simeq 11$, $d_{11} \simeq 23$ and $d_{15} \simeq 85$ in pC/N.

7.2.2 BaTi$_{0.50}$Zr$_{0.50}$O$_3$

The case of BaTi$_{0.50}$Zr$_{0.50}$O$_3$ [Fig. 4.2(f-h)] clearly reveals the importance of the atomic ordering on the dynamical properties. The first result is that the atomic arrangement associated to the high-symmetry-$Fm\bar{3}m$ rocksalt configuration is lower in energy than the ordered-$P4mmm$ structures based on chains or layers of same type of B-cations: the three structures have been optimized and the energy lowering with respect to the highest energy layered configuration is of about -30.95 meV/f.u. for the columnar configuration and -93.73 meV/f.u. for the rocksalt.

Beyond that, all the three configurations show very different dynamical properties. Looking at the phonon frequencies reported in Table 7.2, unstable modes appear at each high-symmetry point of the $P4mmm$-tetragonal Brillouin zone of the layered-based supercell. Specifically, the

BaTi$_{0.5}$Zr$_{0.5}$O$_3$ ($P4mmm$-supercell)						
Configuration	$\Gamma(0\ 0\ 0)$	Z $(0\ 0\ \frac{1}{2})$	M $(\frac{1}{2}\ \frac{1}{2}\ 0)$	A $(\frac{1}{2}\ \frac{1}{2}\ \frac{1}{2})$	R $(0\ \frac{1}{2}\ \frac{1}{2})$	X $(0\ \frac{1}{2}\ 0)$
layered [110]	274.18i	271.42i	65.17i	60.85i	259.90i	262.65i
columnar [001]	304.05i	90.60	301.88i	75.43	76.32	299.4i

Table 7.2: Lowest phonon frequencies (cm^{-1}) at the high symmetry points of the tetragonal $P4mmm$ Brillouin zone. As BaTi$_{0.5}$Zr$_{0.5}$O$_3$ has no instabilities within VCA, only results from supercells are reported.

	BaTi$_{0.50}$Zr$_{0.50}$O$_3$		
	$Fm\bar{3}m$-2x2x2 CELL		
	Atoms		Total
$B - B'$	Ti-Zr	($\parallel$)	-0.063
	d=4.075 Å	($\perp$)	+0.008
$A - B$	Ba-Ti	($\parallel$)	-0.027
	d=3.529 Å	($\perp$)	+0.013
	Ba-Zr	($\parallel$)	-0.030
	d=3.529 Å	($\perp$)	+0.013
$B - O$	Ti-O	($\parallel$)	-0.002
	d=1.978 Å	($\perp$)	-0.020
	Zr-O	($\parallel$)	-0.025
	d=2.097 Å	($\perp$)	-0.015
$A - O$	Ba-O	(xx')	+0.002
	d=2.882 Å	(yy')	-0.011
		(zz')	-0.005

Table 7.3: Interatomic force constants from supercell calculations for BaTi$_{0.50}$Zr$_{0.50}$O$_3$ in the cubic-$Fm\bar{3}m$ phase. Units are in (Ha/bohr^2). Directions ($\parallel$), (xx') and ($\perp$), (yy'), (zz') refer to the local coordinates system between different atomic coupling. Distances in (Å) between the selected atoms are also reported. Atomic labels refer to Fig. 7.4(b).

two instabilities appearing at the M and A points are associated to antiferrodistortive modes due to oxygen rotations, while all the other instabilities are related to the polar instability arising from Γ and mostly ascribed to the (Ti,O)-polar motion along the direction of preserved O-Ti-O-Ti-O chains. Zr displays the same dynamics as described for the BaTi$_{0.875}$Zr$_{0.125}$O$_3$ case. Within the columnar configuration, the instabilities appear only along the $\Gamma - X - M$ line and are linked to the polar distortion arising from the Γ-point with the same character as the former cases. In sharp contrast, no instability appears for the rocksalt configuration. In particular, the absence of O-Ti-O-Ti-O chain in any direction makes the cubic phase stable. As reported in Table 7.3, in fact, both the Ti-O and Zr-O interactions are dominated by the short-range forces and the slightly destabilizing interaction between Ba and O atoms is not enough to globally destabilize the system.

Since the Zr-doping directly affects the B-O interaction, the system clearly prefers to keep an isotropic surrounding environment in order to preserve the same kind of interaction in each direction, i.e. O-Zr-O-Ti-O chains like in the $Fm\bar{3}m$-structure. This arrangement prevents the original Ti-driven polar distortion of BaTiO$_3$. Therefore, the ground-state for the $y = 0.50$ composition is globally non-polar, as reported in Fig. 7.4(d).

7.3   VCA vs SUPERCELL approaches

By comparing the results reported in Sec. 7.1 and Sec. 7.2, it becomes clear that the VCA method is not suitable for describing the Ba(Ti,Zr)O$_3$ solid solutions. The decrease of polarization for increasing Zr-concentration is obtained in both cases. However, within VCA, neither the energetics nor the dynamical properties are well reproduced. In particular, VCA does not detect any instability in the cubic phase already for $y > 0.10$, whereas it is not the case as found out in BaTi$_{0.875}$Zr$_{0.125}$O$_3$-supercell as well as in the experiments introduced at the beginning of the present section. As already widely discussed, the reason behind such failure is that VCA does not allow to access distinct contributions to the dynamics arising from the different nature of the mixed cations as well as the effects due different atomic ordering. The latter is, in fact, the main variable controlling the dynamics in BTZ. Additionally, we know that the FE instability in BaTiO$_3$ is strongly sensitive to the O $2p$ - Ti $3d$ hybridization. Therefore, as Zr occupies $4d$ states, the changes in the electronic properties induced by the Zr-doping directly affect the dynamics of the system. As such, the way VCA combines the different electronic properties from the parents BaTiO$_3$ and BaZrO$_3$ is also determinant in the failure of the VCA approach for BTZ.

In Fig. 7.5 we compare the electronic density of states (DOS) within the two approaches. It appears that VCA acts in making an "horizontal" average of the DOS of the parent compounds. This is clearly visible in Fig. 7.5(a), where we have aligned the valence-band maximum of BaTiO$_3$, BaZrO$_3$ and the VCA compound. In fact, the DOS calculated by VCA is the one of BaTiO$_3$ horizontally shifted toward that of BaZrO$_3$ proportionally to the 12.5% composition of Zr since it is linearly interpolating between the $3d$ states of Ti and $4d$ states of Zr. In panel 7.5(b), we reproduce this average by adding up the density of peaks facing one with the other with the weight fixed by the chosen composition. The result, plotted on top of the VCA graph, reproduces nicely the calculated DOS (non-linear effects play a minor role in the creation of fictitious virtual atom).

The way supercell-based calculations combine properties from the parent compounds is significantly different [Fig. 7.5(c)]. It results to be a straightforward linear combination of the two DOS. In Fig. 7.5(d), we just added up $\frac{7}{8}DOS_{BTO} + \frac{1}{8}DOS_{BZO}$ and the plot perfectly overlaps the supercell calculated one.

This distinct way of averaging the electronic properties can be the reason why the two approaches reproduce different ground-state for the same composition. The incorrect average location of the d-states of the virtual atoms in VCA (i.e. at higher energy) prevents the correct p-d hybridization, which is at the basis of the ferroelectric distortion in BaTiO$_3$.
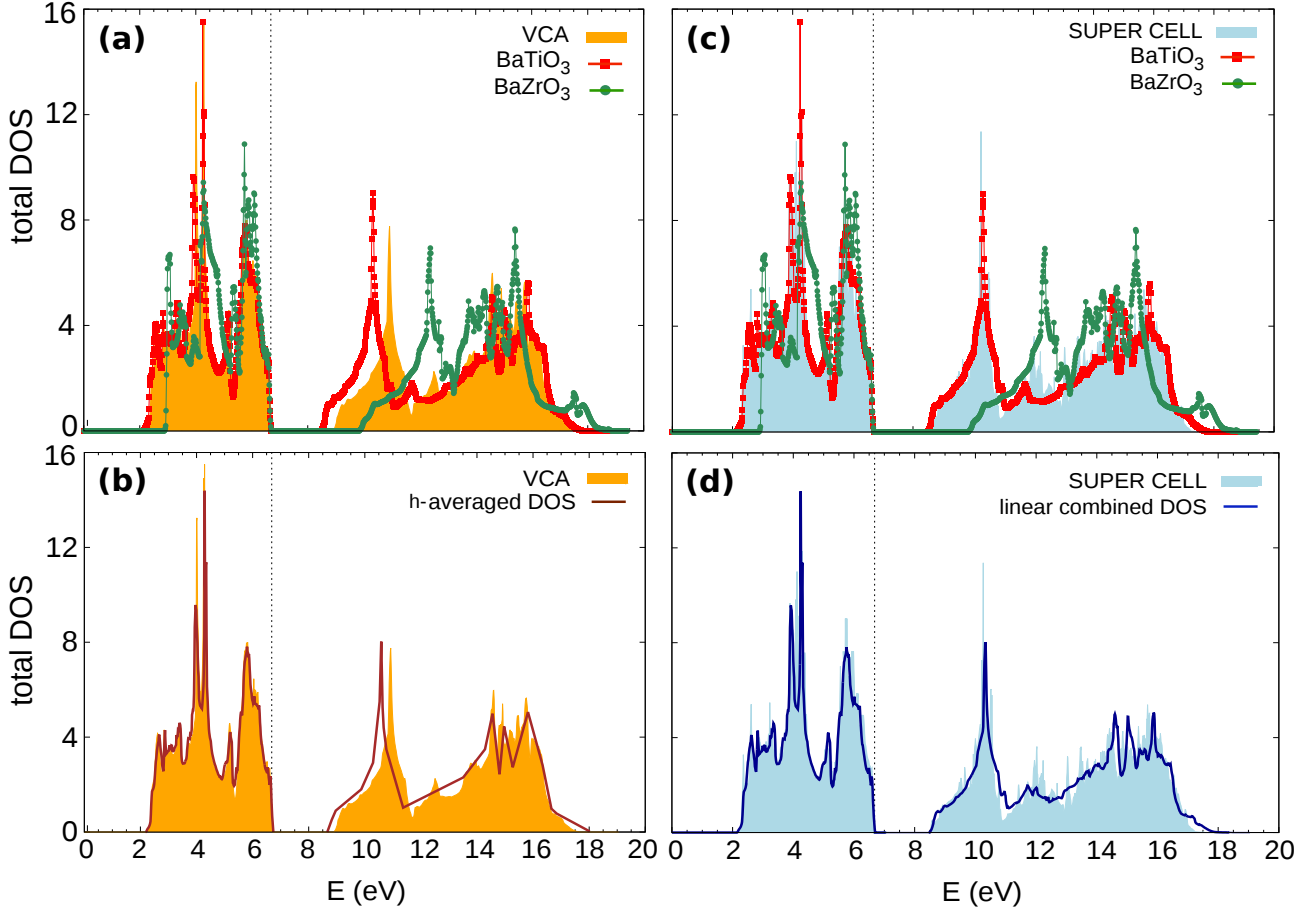
Figure 7.5: Calculated electronic density of states for $BaTiO_3$, $BaZrO_3$ and $BaTi_{0.875}Zr_{0.125}O_3$. Upper panels: DOS of the BTZ solid solution as obtained within VCA (left) and supercell calculation (right) in comparison with the parent compounds. Bottom panels: empirical reproduction of DOS as obtained from "horizontal" average to reproduce the VCA (left) and linear combination for the supercell case (right).

7.4   Role of cation arrangement

Since the dynamics in $Ba(Ti,Zr)O_3$ is strongly related to the geometrical and atomic ordering while the polar distortion in $BaTiO_3$ requires correlated displacements along (Ti,O)-chains, we find it interesting to explore more deeply different compositions and cations arrangements. Thus, we have performed additional calculations for idealized $BaZrO_3/BaTiO_3$ (BZO/BTO) supercells (Fig. 7.6) in order to clarify the role played by the geometrical environment and composition in getting ferroelectricity and homogeneous polarization in $Ba(Ti,Zr)O_3$ solid solutions.

At first, we considered a given structural ordering with different composition. We built $1 \times 1 \times L$ superlattices (BZO/mBTO) by adding up to six layers of $BaTiO_3$ to one unit cell thick layer of $BaZrO_3$, as represented in Fig. 7.6(a). This corresponds to decreasing concentrantion of zirconium from 50% for L=2, to 33% for L=3, 25% for L=4, 20% for L=5 and 17% for L=6. The total length in terms of unit cells is $L = m + 1$. Then, proceeding from the evolution with L of the energetics and polarization along the stacking direction, we tried to explain the
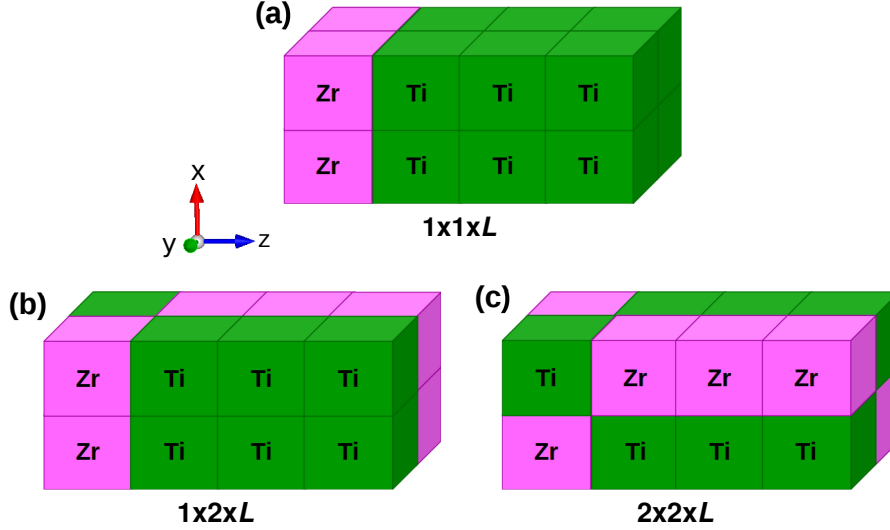
Figure 7.6: Scheme of the investigated BZO/mBTO-based supercells. (a) $1 \times 1 \times L$ superlattice based on one single chain of BaZrO₃-mBaTiO₃ with decreasing composition of zirconium. The smallest chain with L=2 corresponds to the layered 50%-composition. The represented chain is doubled along the x and y direction to help the visualization of the crystal periodicity. (b)-(c) $1 \times 2 \times L$ and $2 \times 2 \times L$ supercells based on alternating chains BaZrO₃-mBaTiO₃ and BaTiO₃-nBaZrO₃ to keep a 50% global composition. The smallest cells with L=2 correspond to the columnar and rocksalt 50%-composition, respectively. The represented $1 \times 2 \times L$-case is doubled along the x to help visualization.

appearance of ferroelectricity by a simple electrostatic model.

In detail, we started our study by investigating the appearance of polarization along the epitaxy direction of the $1 \times 1 \times L$ superlattice. For each length L, we fully relaxed the centrosymmetric $P4/mmm$ and the polar $P4mm$ structures, where the inversion symmetry breaking is due to the atomic displacements along the z direction. As expected, we found no polar distortions along the z direction for L=2. Because of the periodicity of the crystal, this configuration corresponds, in fact, to the layered structure described in Sec. 7.2.2, Fig. 4.2. Conversely, for $L \geq 3$ the polar structures have an energy gain with respect to the paraelectric one and values of polarization increase with the number m of BaTiO₃ layers. Values of P_s are reported in Table 7.4 and in Fig. 7.8. Then we described the atomic distortion from the paraelectric to the ferroelectric phase as a cooperative motion around the center of mass (CM) of the system, in order to better clarify the driving mechanism. This description has revealed the active role of Zr-atom in the polarization against the dynamical properties found out in bulk BaZrO₃ as well as in the investigated Ba(Ti,Zr)O₃ solid solutions (Sec. 5.1.4 and 7.2 respectively). For $m \geq 2$, BZO/mBTO superlattice behaves like BaTiO₃ with the opposite motion of the O-anions and (Ti,Zr)-cations. In terms of stiffness, the zirconium atom experiences a much smaller "on-site" force constant in the direction of the epitaxy, *i.e.* of the Ti-atoms, that allows for the Zr-polar motion. Moreover, the associated Born effective charge, of about $\simeq 7.2\ e$, is considerably anomalous along that direction and comparable to that of Ti.

For the sake of completeness, we also performed DFPT calculations in order to evaluate the d_{33} piezoelectric coefficient in the $P4mm$ phase. Results are reported in Table 7.4. Moreover,

	1x1xL			1x2xL			2x2xL		
L	ΔE	P	d_{33}	ΔE	P	d_{33}	ΔE	P	d_{33}
2	0.0	0.0	0.0	0.0	0.0	0.0	0.0	0.0	0.0
3	-1.0	17.0	77.3	-0.8	10.2	34.0	-1.3	11.1	28.0
4	-4.2	24.2	57.2	-5.6	15.9	–	-9.2	17.3	–
5	-6.7	27.2	52.3	-10.2	18.1	–	-16.3	19.7	–
6	-8.6	28.9	49.7	-13.8	19.3	–	-21.7	21.0	–

Table 7.4: Comparison of P (in $\mu C/cm^2$) and d_{33} (in pC/N) as a function of the length L in the three investigated atomic arrangements, as obtained by Berry-phase and DFPT calculations. For $1 \times 2 \times L$ and $2 \times 2 \times L$ supercells, DFPT calculations have been performed only for $L=3$. For comparison, in $P4mm$-BaTiO$_3$ we obtained $d_{33} \simeq 43.3\ pC/N$. Relative energy gain between the optimized ferroelectric and paraelectric phases [ΔE(FE-PE) in meV/f.u.] is also reported.

it results that this polar phase is not the ground-state. In fact, it still presents phonon polar instabilities (not shown) in the (x, y) plane, i.e. along the preserved Ti-O-Ti-O chains, with dynamical properties similar to the Ba(Ti,Zr)O$_3$ solid solutions described in Sec. 7.2.

In order to interpret the latter results, specifically the polar activation of Zr, here we adapt the simple model proposed in Ref. [92] describing the behavior of dielectric/ferroelectric multi-layers to our BZO/mBTO superlattice.

Neglecting interface corrections, the total energy of a $(1, m)$ superlattice can be written as

$$E(P_{BZO}, P_{BTO}; m) = U_{BZO}(P_{BZO}) + mU_{BTO}(P_{BTO})$$
$$+ C(m)(P_{BTO} - P_{BZO})^2 \tag{7.1}$$

Here P is the polarization arising from the displacement of the ions from their high-symmetry positions under the condition of zero electric field, U is the internal energy of bulk BaZrO$_3$ and BaTiO$_3$ at zero field as a function of P and $C(m)(P_{BTO} - P_{BZO})^2$ is macroscopic electrostatic energy, E_{elec}, resulting from the eventual presence of non-vanishing electric fields in the layer when P_{BZO} and P_{BTO} are different. This term typically acts as an energy penalty which tends to reduce the polarization mismatch in polarizing the dielectric layer and depolarizing the ferroelectric one. In practice, when the dielectric layer is sufficiently polarizable, this term forces the system to adopt a uniform polarization along the stacking direction (z direction in Fig. 7.6), i.e. $P_{BZO} = P_{BTO} = P$. In this case the model reduces to [204, 205, 206]

$$E(P; m) = U_{BZO}(P) + mU_{BTO}(P) \tag{7.2}$$

The energies $U_{BTO}(P)$ and $U_{BZO}(P)$ can be directly obtained from appropriate DFT calculations on pure bulk compounds. In the case of BaTiO$_3$, we built the adiabatic path from the paraelectric to the ferroelectric $P4mm$ phase (discussed in Sec. 5.2) by means of linear interpolation of the atomic displacements. During this interpolation the volume is fixed to the one

BaTiO₃			BaZrO₃			
α_T	β_T	γ_T	$\alpha_Z^{(a)}$	$\beta_Z^{(a)}$	$\alpha_Z^{(b)}$	$\beta_Z^{(b)}$
-0.054	1.8x10⁻⁵	3.4x10⁻⁹	0.048	1.37x10⁻⁵	0.073	2.26x10⁻⁵

Table 7.5: Values of the parameters used in the $U_{BTO}(P)$ and $U_{BZO}(P)$ expansion as resulted from a fitting procedure. For BaZrO₃, we reports the parameters for both the constructions: (a) from the minimization procedure at fixed P (blue curve in Fig. 7.7); (b) from the empirical approach (green curve in Fig. 7.7).

of the polar structure. For each intermediate configuration, we computed the internal energy and polarization. This results into a double-well energy profile that we fit with the standard polynomial expansion

$$U_{BTO}(P) \simeq \alpha_T P^2 + \beta_T P^4 + \gamma_T P^6$$

where α_T, β_T, γ_T are the fitting parameters [2]. We used a similar expansion for BaZrO₃. However, according to the paraelectric nature of this compound, the coefficient of the second order term is positive. Thus we restricted the expansion to the fourth order and we write

$$U_{BZO}(P) \simeq \alpha_Z P^2 + \beta_Z P^4.$$

In this case, as the system does not show any polar instability, the only way to follow the evolution of the internal energy $U_{BZO}(P)$ with the ferroelectric distortion is to freeze the pattern of the motion along the z direction. We defined the total distortion τ as a linear combination of the eigendisplacements associated to the polar modes, i.e. $\tau = a_1\eta_{TO1} + a_2\eta_{TO2} + a_3\eta_{TO3}$, with $\sum_i a_i^2 = 1$ and $\langle \eta_i | M | \eta_i \rangle = 1$. The first approach was to determine the coefficients of the expansion by minimizing $U_{BZO}(P)$ to equilibrium values of η_i with the constrain of fixed P, as proposed in Ref. [207]. From this minimization we obtained a_1=0.945, a_2=0.325 and a_3=0.044, that corresponds to a pattern dominated by the softest TO_1 mode of BaZrO₃ driven by the Ba motion (see Table 5.2). However, this result is not in full agreement with the pattern of distortion obtained from the atomic relaxation in the superlattice previously described. Therefore, we also built $U_{BZO}(P)$ from the relaxed pattern. In detail, we considered the distortion of the BaZrO₃ unit cell in the $1 \times 1 \times 3$ superlattice and we projected it on each TO_i mode in order to get the a_i coefficient to be compared with the previous procedure. We obtained a_1=0.595, a_2=0.802 and a_3=0.051, that clearly reveal the key role of zirconium. The $U_{BZO}(P)$ curves obtained via the two procedures are shown in Fig. 7.7.

Then, from the minimization of Eq. 7.2 with respect to P, we obtain that a spontaneous polarization is admitted if the condition $m > \frac{\alpha_Z}{|\alpha_T|}$ is satisfied, otherwise P is zero. The resulting

---

[2]The sixth order term is introduced to ensure a proper description of the physics of the system as it is close to a tricritical point, i.e. change of the order of the phase transition via a change in sign of the coefficient of the fourth order term.
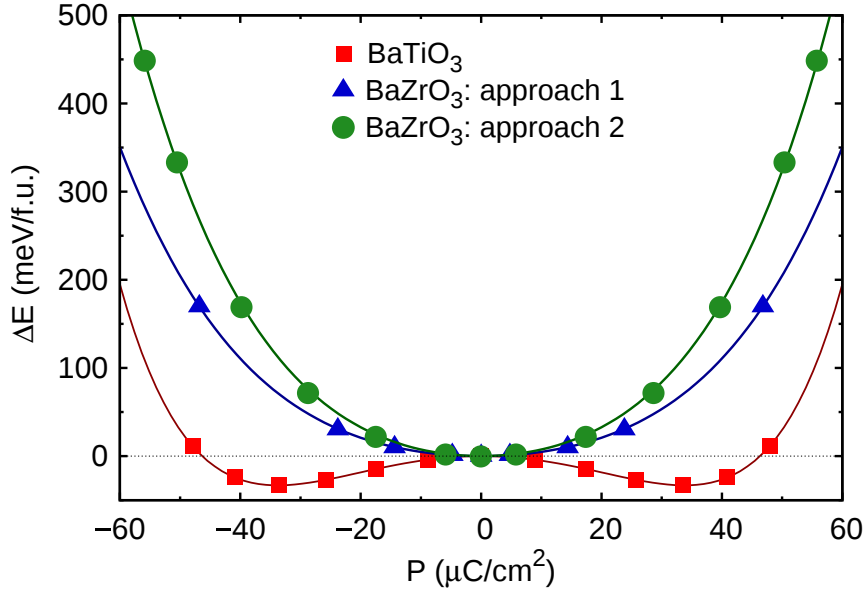
Figure 7.7: Variation of total energy (in meV/f.u.) as a function of the varying polarization (in $\mu C/cm^2$) from the centric to the polar configurations for distorted bulk $BaTiO_3$ (red squares) and $BaZrO_3$. For the latter, curves as obtained within the two approaches are reported: (blue triangles) from the minimization procedure at fixed P; (green circles) from the relaxed pattern of distortion of $1 \times 1 \times 3$ superlattice.

formula for the polarization and energy are

$$P^2(\alpha, \beta, m) \simeq -\frac{m\alpha_T + \alpha_Z}{2(m\beta_T + \beta_Z)}$$

$$E(\alpha, \beta, m) \simeq -\frac{(m\alpha_T + \alpha_Z)^2}{4(m\beta_T + \beta_Z)}$$

Coefficients are reported in Table 7.5. The evolution of P and E resulting from the electrostatic model within the two different approaches and from DFT calculations are reproduced in Fig. 7.8. The two models globally reproduce the same trend, however the second one built on the relaxed pattern is in better agreement with the calculations. In fact, from the parameters related to the first curve, with smaller curvature, a polar state is admitted for all m instead of the condition $m \geq 2$. On one hand, the quantitative inconsistencies between the two approaches, both in the distortion pattern and in ferroelectric properties of the superlattice, point out that a simple model only based on pure bulk quantities can fail in reproducing the dynamics of the system because of strong coupling between the two different B-cations at play. On the other hand, the perfect agreement obtained between the "second" model and first-principles calculations (Fig. 7.8) confirms the validity of the hypothesis of uniform P in the superlattice, i.e. electrostatic energy cost equal to zero, due to the fact that the polar distortion of Zr preserves the charge transfer along Zr-O-Ti-O-Ti-O chains. Moreover, P asymptotically approaches the value of $P4mm$-$BaTiO_3$, that is of about $\simeq 34 \ \mu C/cm^2$ as calculated via DFT.

These results, in particular the cooperative $BaTiO_3$-like atomic motion along the Zr-O-Ti-O-Ti-O chains, are the manifestation of the "chain-like" nature of the distortion. In fact, we
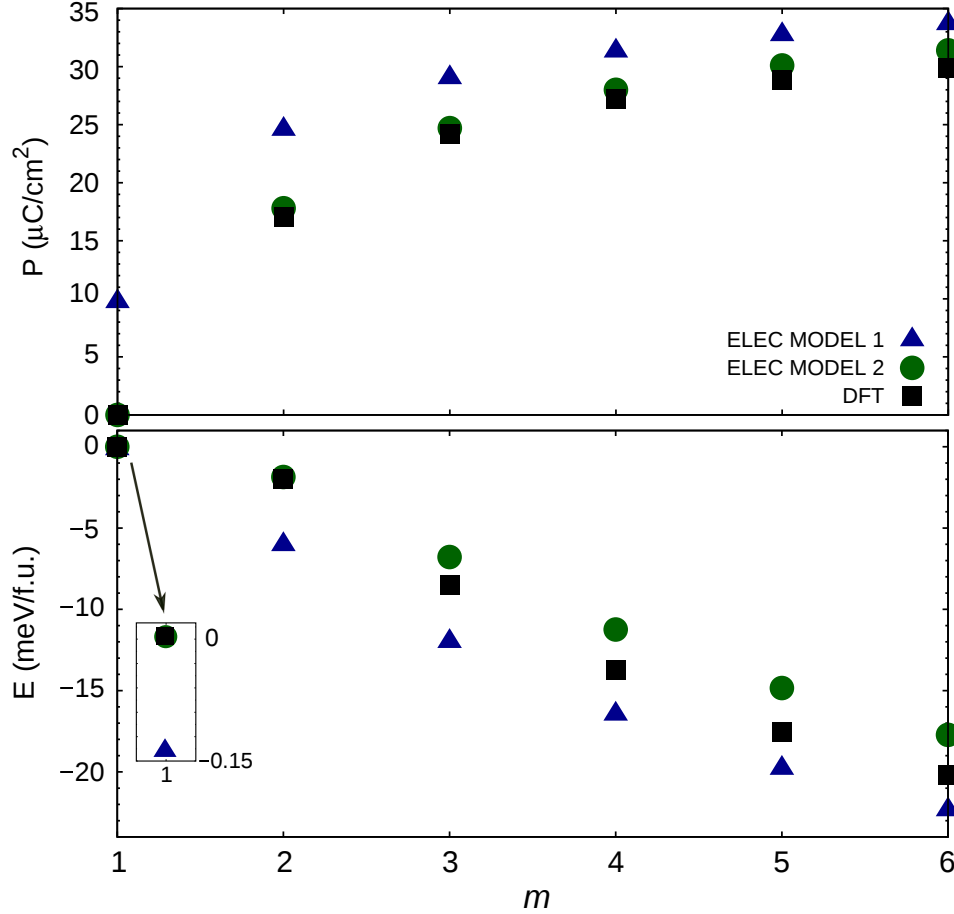
Figure 7.8: Evolution of the total polarization (in $\mu C/cm^2$) and energy (in meV/formula unit) as a function of increasing number m of BTO-layers. Values obtained from DFT calculations and from the electrostatic model are reported. We refer to results coming from the first approach based on the minimization at fixed P as model 1, while to those based on the relaxed pattern as model 2. The inset shows the different energies for $m = 1$. The E from DFT calculations refers to the relative energy gain between the optimized ferroelectric phase and the centro-symmetric reference with volume fixed to that of the polar structure.

already discussed in Sec. 7.2 how the break of correlated Ti-O chains introduced by the polar inactive Zr prevents the propagation of the original BaTiO₃ distortion in Ba(Ti,Zr)O₃ solid solutions. Nevertheless, when a minimum number of consecutive Ti atoms are preserved along those chains, the substitution of one atom of Ti with one of Zr does not suppress the polarization. On the contrary, the electrostatic coupling forces the system to sustain a homogeneous P by making Zr polar active.

Previous calculations and physical interpretation have been based on superlattices with decreasing Zr-concentration. Therefore, in order to further prove the crucial role played by the local "chain-like" correlation over the increasing BTO-concentration, we have better distinguished the effects arising from the composition and from the imposed atomic ordering. Thus we carried DFT calculations on $1 \times 2 \times L$ and $2 \times 2 \times L$ ordered supercells as we did for the $1 \times 1 \times L$ case. These two supercells, composed by alternating single chains of BZO/mBTO

and BTO/nBZO, allow to keep the total composition fixed to 50% of Zr and Ti and to preserve locally the imposed "chain-like" atomic ordering, as reproduced in Fig.7.6(b,c).

For both the arrangements, it is not surprising to get no polar phases for $L = 2$ from the inversion symmetry breaking along the z direction. In fact, by periodicity, these structures correspond to the columnar and rocksalt orders described in Sec. 7.2.2 (Fig. 4.2). Relevant results arise from $L \geq 3$, since a spontaneous polarization appears along the BZO/mBTO chains driven by the (Zr,Ti)-motion against the oxygens inside the global BaTi$_{0.50}$Zr$_{0.50}$O$_3$ matrix. As in the $1 \times 1 \times L$ superlattice, in fact, we described the atomic displacements as a cooperative motion around CM and we found out that most of the polar distortion comes from the B-cations stacked on the local BZO/mBTO chains. We also obtained sizeable d_{33} piezoelectric coefficient, but smaller than in the $1 \times 1 \times L$ and pure $P4mm$-BaTiO$_3$ cases, as reported in Table 7.4 (because of the high computational cost for these supercells, we performed DFPT calculations only for the case $L=3$). A simple explanation could be that the coexistence of the BZO/mBTO and BTO/nBZO chains, that behave differently since the cations in the latter one do not participate to the polarization, could globally prevent the variation of P. Noteworthy is that the polar $P4mm$ phase within the $2 \times 2 \times L$ structure is stable.

The main finding from the comparison of results coming from the three different structures is the polar activation of zirconium in Ba(Ti,Zr)O$_3$ system as a function of specific atomic ordering, that is local BZO/mBTO chains with $m \geq 2$, and independent of the total composition of the matrix. Therefore, the analysis and physical interpretation of the dynamics conducted through the previous electrostatic model remains valid also for the $1 \times 2 \times L$ and $2 \times 2 \times L$ cases: Zr atom is locally activated by a Zr-Ti coupling to avoid polarization gradients and electrostatic energy cost. But then, the gain of energy related to polarizing ferroelectric BaTiO$_3$ is decreased by the energy cost to polarize BaZrO$_3$.

From the $U(P)$ curves of the pure compounds in Fig. 7.7 and trends reported in Fig. 7.8, the maximum Zr-concentration to get a ferroelectric system seems to be around 30% in agreement with experimental observations. Beyond this concentration, the results are line with the observed relaxor behavior of BaTi$_{1-y}$Zr$_y$O$_3$ and existence of polar nanoregions associated to local fluctuation of y, that allows for correlated polar motions, as described in Refs. [209, 208, 210, 212]. Maiti *et al.*, in their experimental investigation of the correlation between structure and property in Ba(Ti,Zr)O$_3$ ceramics [208, 211], point out that a gradual incorporation of Ti^{4+} into the nonpolar BaZrO$_3$ lattice results in the evolution of relaxation behavior because of the increasing amount of ordering and density of nano-sized Ti^{4+}-rich polar regions in the Zr^{4+}-rich matrix. Moreover, C. Laulhé *et al.* suggest that the observation of such polar nanoregions consist in 1D-chains with correlated Ti displacements [210]. By means of Monte-Carlo simulations, Akbarzadeh *et al.* describe the Ti sites as nuclei acting to formation of polar clusters with rather small contribution from Zr sites [212].

Accordingly, by means of combined DFT calculations and phenomenological model, we have provided a complementary microscopic information. In particular, the behavior of the polar-clusters in a global paraelectric-matrix, like the case of the investigated BaTi$_{0.50}$Zr$_{0.50}$O$_3$ composition, may be due to the cooperative motion of Zr and Ti atoms and not only by isolated Ti-dipoles.

Chapter 8

Discussion & Conclusions

In this thesis, we have investigated the dynamical, structural, ferroelectric and related properties of chosen compositions of $(Ba,Ca)TiO_3$-$Ba(Ti,Zr)O_3$ solid solutions and related parent compounds by means of first-principles calculations based on Density Functional Theory, with the intent to identify some of the key microscopic mechanisms behind the enhanced piezoelectric properties of $(Ba,Ca)(Ti,Zr)O_3$. In particular, we have focused on the evolution of the properties in $(Ba,Ca)TiO_3$ and $Ba(Ti,Zr)O_3$ solid solutions (Chap. 6 and Chap. 7) and analyzed them in relationship with those of the pure $BaTiO_3$, $CaTiO_3$, $CaZrO_3$ and $BaZrO_3$ parent compounds (Chap. 5) in order to disentangle the role of individual atomic substitutions at the A- and B-sites. In fact, these two solid solutions result from the mixing of systems with very different dynamics. This turns out to be a crucial point regarding the suitableness of the *ab-initio* method employed, VCA vs direct supercell calculations.

When going from $BaTiO_3$ to $CaTiO_3$ in $(Ba,Ca)TiO_3$, the main feature is the mixing of the so called B-driven and A-driven ferroelectricity associated to the two parent compounds, respectively. Cubic $BaTiO_3$, in fact, exhibits strong and highly polar instabilities that expand over the entire Γ-X-M planes of the Brillouin zone, as shown in Fig. 5.1(a). They are determined by the destabilizing Ti-O interaction resulting in the relative motion of Ti atoms with respect to oxygens. Particularly, this polar distortion requires cooperative atomic displacements along Ti-O chains. From the electronic point of view, such instability is ascribed to the hybridization between the O $2p$ and Ti $3d$ states [187]. The sizeable stiffness of Ba determines its negligible contribution to the distortion instead. Related values of the "on-site" and interatomic force constants are reported in Tables 5.1 and 5.3. These mechanisms stabilize the rhombohedral $R3m$-phase, as reported in Fig. 5.2 and Fig. 6.5(a). On the contrary, $CaTiO_3$, in its cubic phase, hosts a strong polar instability confined at Γ and mostly related to a polar motion of Ca and O. In fact, we found that a strong destabilizing interaction occurs between these two atoms (Table 5.3). Such Ca driven instability is ascribed to steric effects as the smaller size and greater softness of Ca than Ba (Tables 4.1 and 5.1). In fact, same dynamical properties characterize $CaZrO_3$, for which the covalency between Zr and O is even further reduced [187]. Additionally, the reduced volume of cubic $CaTiO_3$ compared to $BaTiO_3$

shortens the Ti-O distances, making the Ti-O interaction mainly repulsive and Ti atoms much more stiffer (volume effect on Ti-O interaction is shown in Fig. 6.4). These mechanisms favor the tetragonal $P4mm$-phase over the $R3m$-one in CaTiO$_3$ [Fig. 5.2 and Fig. 6.5(c)]. However, the ground-state of CaTiO$_3$ is determined by the strong AFD instabilities present along the $M - R$ line [see Fig. 5.1(b) and Fig. 5.2]. Consequently, as obtained from supercell calculations for BaTiO$_3$-rich compositions, the mixing of the two A-cations in Ba$_{1-x}$Ca$_x$TiO$_3$ solid solutions does not make barium active in the polar distortion, but introduces a cooperative motion of Ca-atoms together with Ti-atoms against the oxygens-cage, i.e. interplay between A-site and B-site driven polar distortion [Fig. 6.5(h)]. A ferroelectric ground-state is then predicted up to $x = 0.50$. As it is expected from the dynamical properties and energetics of the two parent compounds, the increasing Ca-concentration favors $P4mm$-like polar phases over the $R3m$ one. In particular, in the Ba-rich region, the evolution from the B-type to the A-type ferroelectricity promoted by the partial atomic substitution of Ba with Ca arises from the interplay of two distinct mechanisms: the weakening of Ti-driven ferroelectricity via the modification of the Ti-O interactions and the emergence of Ca-driven ferroelectricity sustained by the Ca-O interactions. Such effects, then, reduce and eventually suppress the energy barrier between the different polar phases. This behavior yields to increasing piezoelectric response as the energy landscape in terms of polarization orientation becomes quasi-isotropic. Specifically, these properties are found in Ba$_{0.875}$Ca$_{0.125}$TiO$_3$, as obtained from the use of $2 \times 2 \times 2$ supercells [Figs. 6.5(b,e)]. Interesting and qualitatively compatible trends have been also achieved within the VCA approach. However, within VCA the distinction of the dynamics of Ba and Ca atoms is not accessible, because only a final average effect from the two cations at the same A-site is reproduced, as shown in Fig. 6.1(c). This method forces the change of character of the mechanisms at play without allowing distinction of the opposite nature of Ba and Ca. In fact, Ca is actually polar active for each composition x. Such a limitation is especially evident in the finding of the concentration where the inversion of polar phases takes place, and in the polarization trend, that is decreasing with Ca-concentration within VCA, while it is increasing within the supercells.

When going from BaTiO$_3$ to BaZrO$_3$ in Ba(Ti,Zr)O$_3$, the scenario is completely different. BaZrO$_3$, in fact, does not host any polar instability. Zr atom is quite stiff and the Zr-O interaction is strongly repulsive, as reported in Table 5.1 and Table 5.3. From the electronic point of view, this can be ascribed to the fact that Zr occupies $4d$ states less hybridized with the $2p$ states of O. Therefore, at first, low Zr-concentration indirectly further stabilizes the $R3m$-phase in BaTi$_{1-y}$Zr$_y$O$_3$ [Fig. 7.4(c)] because of the larger ionic radius of Zr than Ti, i.e. volume effect on the dynamics of BaTiO$_3$. However, the spontaneous polarization is slightly reduced. Then, for higher Zr-concentration, the system tends to globally reduce the polar distortion, thus suppressing the original ferroelectricity of BaTiO$_3$. In fact, the presence of Zr on the B-site introduces breaks along the correlated Ti-O-Ti-O chains, preventing the preservation of polarization. Such mechanisms are evident both for $y = 0.125$ and $y = 0.50$

supercells compositions. For instance, in $BaTi_{0.50}Zr_{0.50}O_3$, the energetically favored $Fm\bar{3}m$ nonpolar phase is stable. Nevertheless, polar nanoregions can be locally preserved in Ti-rich regions. Additionally, by building different supercell environments based on $BaZrO_3/mBaTiO_3$ chains (Fig. 7.6), we found that as soon as Zr experiences at least 2 subsequent Ti atoms, it becomes active in the polarization and a cooperative motion of the two B-cations is observed. The reason of such behavior, explained via a basic electrostatic model, is that Zr is locally activated in order to preserve homogeneous polarization along the Zr-O-Ti-O-Ti-O chain and to minimize the electrostatic energy cost. Such important role played by local structures on the Zr-Ti dynamics and differences in the electronic configuration of the two B-cations make VCA not suitable for the $Ba(Ti,Zr)O_3$ system. In fact, predictions achieved via supercell-based calculations concerning both the dynamics and energetics are not reproduced by VCA.

From a methodological point of view, in both $(Ba,Ca)TiO_3$ and $Ba(Ti,Zr)O_3$, we found that the two types of cations introduced at the A and B sites, respectively, behave very differently and, therefore, the mixing can hardly be described by averaged virtual atoms. Although providing some trends, VCA is therefore not suitable for reproducing and understanding the microscopic physics of $(Ba,Ca)(Ti,Zr)O_3$ solid solutions. By construction, in fact, this approximation fails in reproducing both specific local arrangements and same-site independent motion of the active atoms involved in the ferroelectric instabilities, oversimplifying the actual dynamical and electronic properties of the solid solutions. These are key features for the overall behavior of $BaTiO_3$-based solid solutions, which thus need to be addressed by means of direct supercell calculations. This also clarifies why recent attempts [213] to study BCTZ from a VCA-based effective Hamiltonian required to adjust by hands some of the parameters initially fitted from first-principles in order to reproduce experimental data.

In conclusion, we have seen that in $(Ba,Ca)TiO_3$ the competition between the B-type and the A-type ferroelectricity of the two parent compounds is the key mechanism behind the eventual competition between different polar phases. In fact, $BaTiO_3$ and $CaTiO_3$ have a reversed energy sequence of ferroelectric states so that a crossover between them is required to achieve the inversion. The achievement of such crossover manifests in quasi-degeneracy of the energy landscape and quasi-isotropic polarization, thus enhancing the piezoelectric response.

Different behaviors characterize $Ba(Ti,Zr)O_3$, where the appearance of ferroelectricity is strongly dependent on the local atomic arrangements and electrostatic. $BaZrO_3$, in fact, exhibits highly stable cubic phase. The increasing substitution of Ti by Zr thus acts to reduce the spontaneous polarization and progressively suppress the overall ferroelectricity. Nevertheless, polar nanoregions can be preserved in Ti-rich regions.

Moreover, we have provided a direct comparison between the virtual crystal approximation (VCA) and direct supercell calculations, showing that the specific microscopic physics of $(Ba,Ca)TiO_3$ and $Ba(Ti,Zr)O_3$ solid solutions imposes severe limitations to the applicability of VCA.

With respect to the experimentally observed enhanced piezoelectric response in BCTZ around the polymorphic phase boundary (PPB) at $0.135 \lesssim x \lesssim 0.15$ and $0.11 \lesssim y \lesssim 0.10$ concentrations of Ca and Zr respectively (i.e. low Ca- and Zr- concentrations) [44, 54, 106] (Fig. 1.2), our study reveals that a key microscopic factor is the interplay between weakened Ti-driven ferroelectricity and emerging Ca-driven ferroelectricity, both promoted by steric effects. On the one hand, small concentration of Zr does not drastically affect the original dynamics of BaTiO$_3$, preserving, indeed, the $R3m$ ferroelectric ground-state. However, it acts to contract the spontaneous polarization. On the other hand, the presence of Ca strongly change the dynamical properties of the full system. In particular, small Ca-concentration induces a competition between the Ti-driven ferroelectricity and the Ca-driven ferroelectricity, which would favor separately either a rhombohedral or a tetragonal phase. This thus provides the condition for minimal anisotropy with respect to directions of the polarization and manifests in the enhancement of the piezoelectric response.

Providing such a theoretical investigation on an atomic scale, we believe that our work significantly contributes to clarify the microscopic physics of BaTiO$_3$-based systems and provides a solid background to further investigations of the important family of BCTZ solid solutions via advanced large-scale and finite-temperature simulations. Moreover, the revealed complex mechanisms involved in the dynamics of such systems, might be exploited to develop advanced effective Hamiltonian approaches expanding the number of the key atomic degrees of freedom, going beyond the standard use of VCA. Furthermore, discussing the physics, it is of generic interest to both theorists and experimentalists and might be also relevant to the discussion of other families of solid solutions.

Most of the discussed results are published in D. Amoroso, A. Cano, and Ph. Ghosez, *Phys. Rev. B*, **97**, 174108 (2018).

Appendix A

Distorted phases of BaZrO$_3$

As introduced in Sec. 5.2, the condensation of the out-of-phase oxygen rotations (Table 5.5) associated to the tiny instability at the R point of the cubic Brillouin zone of BaZrO$_3$ [Fig. 5.1(c)], brings the system to lower energy antiferrodistortive structures. The energetics, angle of rotation and volume (per 5-atom cell) of the tetragonal-$I4/mcm$ (T), orthorhombic-$Imma$ (O) and rhombohedral-$R\bar{3}c$ (R) phases with respect to the cubic-$Pm\bar{3}m$ phase are reported in Fig. A.1.
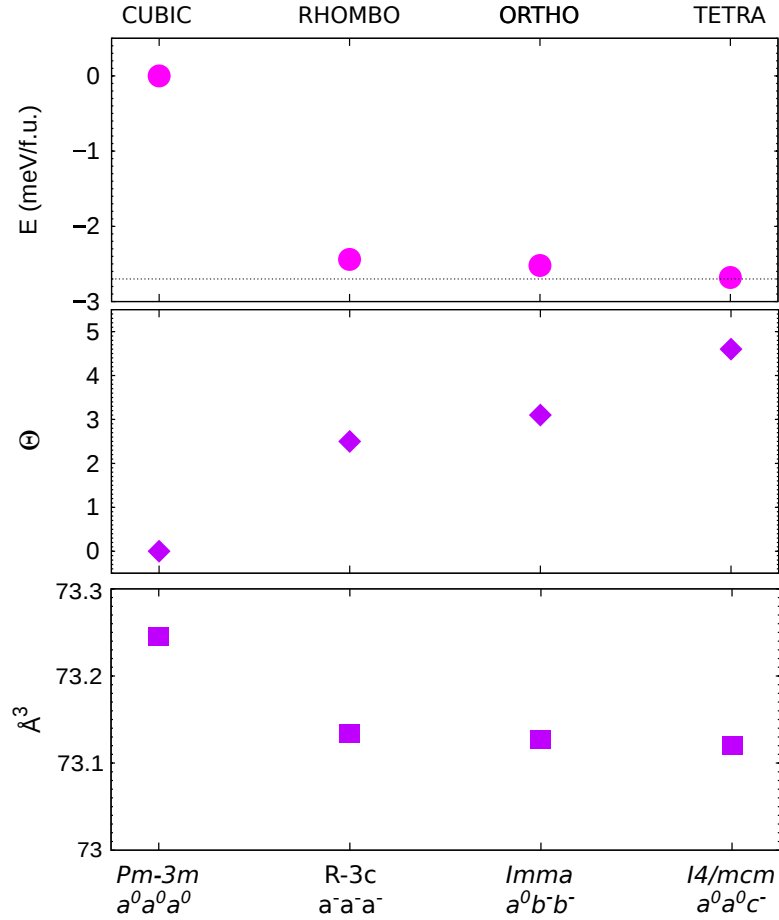

Figure A.1: Energy gain (in meV/f.u.), rotational angle Θ, and volume (in Å^3/f.u.) for T, O, and R antiferrodistortive phases of BaZrO$_3$ with respect to the cubic phase. Structures have been fully relaxed within GGA-WC functional.

In particular, these AFD phases result all stable, as shown by the phonon dispersion curves in Fig. A.2. Phonon calculations have been performed on the fully relaxed AFD structures, and structural details are reported in Table A.1.

Structure	Lattice parameters		Wyckoff positions	
$I4/mcm$	a=b= 5.907 Å	$\alpha = \beta = \gamma = 90°$	Ba 4 b	0.00000 0.50000 0.25000
	c= 8.382 Å		Zr 4 c	0.00000 0.00000 0.00000
			O_1 8 h	0.77000 0.27000 0.00000
			O_2 4 a	0.00000 0.00000 0.25000
$Imma$	a= 5.912 Å	$\alpha = \beta = \gamma = 90°$	Ba 4 e	0.00000 0.25000 0.50046
	b= 8.355 Å		Zr 4 a	0.00000 0.00000 0.00000
	c= 5.922 Å		O_1 4 e	0.00000 0.25000 0.02738
			O_2 8 g	0.25000 0.51389 0.25000
$R\bar{3}c$	a=b=c 5.911 Å	$\alpha = \beta = \gamma = 60°$	Ba 2 a	0.25000 0.25000 0.25000
			Zr 2 b	0.00000 0.00000 0.00000
			O 6 e	0.77200 0.72800 0.25000

Table A.1: Structural details for the $I4/mcm$, $Imma$, and $R\bar{3}c$ AFD optimized structures. Structural analysis has been done via FINDSYM tool [218].

In order to provide an insight into these distorted phases of BaZrO₃, we also provide here the analysis of the zone-center phonon modes. Such analysis can be useful for the interpretation of infrared and/or Raman spectra, being the low-temperature properties of BaZrO₃ still under discussion [214, 163, 215]. Therefore, the irreducible representations at Γ (0,0,0) for the three AFD phases in Mulliken's notation [216] are:

$$I4/mcm \begin{cases} \Gamma_{acoustic} = A_{2u} \oplus E_u \\ \Gamma_{optic} = A_{1g} \oplus A_{1u} \oplus 2A_{2g} \oplus 3A_{2u} \oplus B_{1g} \oplus B_{1u} \oplus 2B_{2g} \oplus 5E_u \oplus 3E_g \end{cases}$$

$$Imma \begin{cases} \Gamma_{acoustic} = B_{1u} \oplus B_{2u} \oplus B_{3u} \\ \Gamma_{optic} = 3A_g \oplus 2A_u \oplus 2B_{1g} \oplus 5B_{1u} \oplus 3B_{2g} \oplus 4B_{2u} \oplus 4B_{3g} \oplus 4B_{3u} \end{cases}$$

$$R\bar{3}c \begin{cases} \Gamma_{acoustic} = A_{2u} \oplus E_u \\ \Gamma_{optic} = A_{1g} \oplus 2A_{1u} \oplus 3A_{2g} \oplus 3A_{2u} \oplus 5E_u \oplus 4E_g \end{cases}$$

In Table A.2, we report the zone-center phonon frequencies and assignments of the associated modes for these distorted phases.
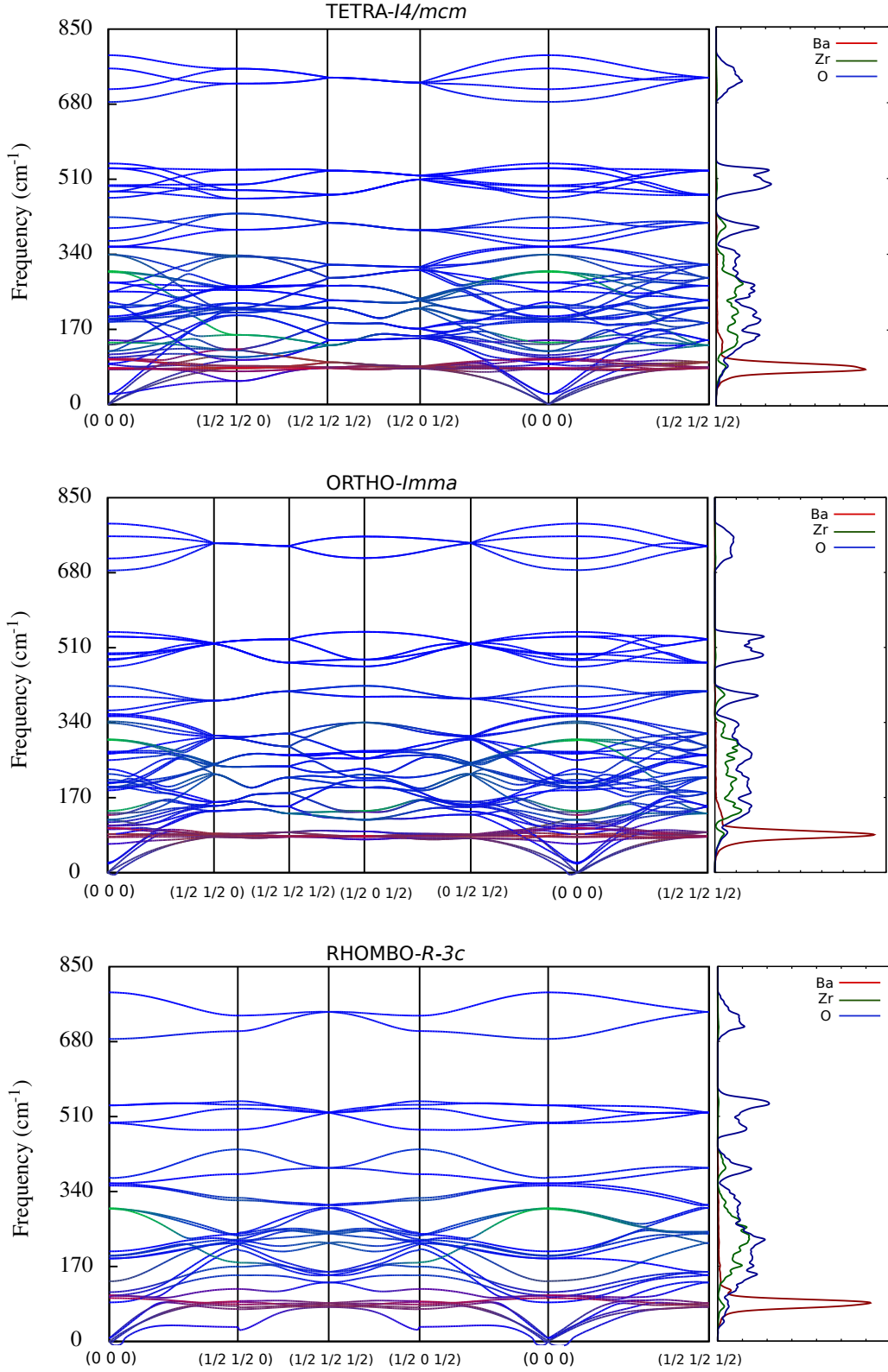
Figure A.2: Calculated phonon dispersion curves of $I4/mcm$, $Imma$ and $R\bar{3}c$ antiferrodistortive structures associated to out-of-phase oxygen rotations in $BaZrO_3$. Phonon density of states by atomic species are also reported on the right side of the phonon band structures. Different colors indicate the different atomic contributions in the corresponding eigenvectors as in Ref. [102] (red for the A atom, green for B atom and blue for O atoms). Small anomalies in the proximity of the high-symmetry Q-points in the phonon dispersion curves of the O and R structures are matter of accuracy in the interpolation procedure to extrapolate the curves [61]. Therefore, they do not have physical meaning and do not affect the provided analysis.

	$I4/mcm$-T				$Imma$-O				$R\bar{3}c$-R		
ω (cm^{-1})	mode	deg.	activity	ω (cm^{-1})	mode	deg.	activity	ω (cm^{-1})	mode	deg.	activity
23.49	E_g	2	Raman	20.01	B_{2g}	1	Raman	7.27	E_g	2	Raman
92.72	A_{1g}	1	Raman	23.02	B_{1g}	1	Raman	88.50	A_{1g}	1	Raman
101.82	E_g	2	Raman	87.07	A_g	1	Raman	98.24	A_{2g}	1	silent
104.36	B_{2g}	1	Raman	100.41	B_{2g}	1	Raman	99.34	A_{2u}	1	IR
106.52	E_u	2	IR	101.36	B_{3g}	1	Raman	104.43	E_g	2	Raman
113.38	A_{2u}	1	IR	103.75	B_{3u}	1	IR	111.66	E_u	2	IR
191.57	E_u	2	IR	106.71	B_{2u}	1	IR	187.82	E_u	2	IR
194.52	A_{2u}	1	IR	107.17	A_g	1	Raman	193.20	A_{2u}	1	IR
194.72	E_u	2	IR	114.24	B_{1u}	1	IR	194.91	E_u	2	IR
199.53	B_{1u}	1	silent	186.36	B_{3u}	1	IR	204.16	A_{1u}	1	silent
301.13	A_{1u}	1	silent	191.90	A_u	1	silent	300.89	A_{1u}	1	silent
302.03	E_u	2	IR	193.75	B_{2u}	1	IR	302.29	E_u	2	IR
356.41	E_g	2	Raman	193.85	B_{3u}	1	IR	353.29	A_{2g}	1	silent
358.05	B_{2g}	1	Raman	194.10	B_{1u}	1	IR	358.38	E_g	2	Raman
494.37	E_u	2	IR	204.40	B_{1u}	1	IR	494.27	A_{2u}	1	IR
496.48	A_{2u}	1	IR	300.73	A_u	1	silent	496.52	E_u	2	IR
534.22	A_{2g}	1	silent	302.11	B_{1u}	1	IR	535.38	E_g	2	Raman
535.33	B_{1g}	1	Raman	302.48	B_{2u}	1	IR	791.52	A_{2g}	1	silent
790.83	A_{2g}	1	silent	354.31	B_{2g}	1	Raman				
				356.37	B_{3g}	1	Raman				
				359.78	A_g	1	Raman				
				494.07	B_{3u}	1	IR				
				494.75	B_{2u}	1	IR				
				497.47	B_{1u}	1	IR				
				534.78	B_{1g}	1	Raman				
				535.53	B_{3g}	1	Raman				
				791.18	B_{3g}	1	Raman				

Table A.2: Calculated phonon frequencies ω (in cm^{-1}) at the Γ (0 0 0) point of the $I4/mcm$, $Imma$, and $R\bar{3}c$ Brillouin zone. The symmetry assignments in Mulliken's notation, degeneracy and activity in the infrared (IR) or Raman spectroscopy for each mode are also reported. The analysis relies on SAM [220] and SMODES [221] tools.

Bibliography

[1] J. Rödel, K. G. Webber, R. Dittmer, W. Jo, M. Kimura, and D. Damjanovic, *J. Eur. Ceram. Soc*, **35**, 1659 (2015).

[2] M. Acosta, N. Novak, V. Rojas, S. Patel, R. Vaish, J. Koruza, G. A. Rossetti, and J. Rödel, *Appl. Phys. Rev.*, **4**, 041305 (2017).

[3] K. Uchino, *The development of piezoelectric materials and the new perspective*, K. Uchino (ed): Chap. 1, pp $1-92$ in *Advanced Piezoelectric Materials: Science and Technology (First Edition)*, Woodhead Publishing 2010..

[4] Y. Saigusa, *Quartz-based piezoelectric materials*, K. Uchino (ed): Chap. 5, pp $171-203$ in *Advanced Piezoelectric Materials: Science and Technology (First Edition)*, Woodhead Publishing 2010..

[5] L. B. Kong, T. Li, H. H. Hng, F. Boey, T. Zhang, and S. Li, *Waste Energy Harvesting: Mechanical and Thermal Energies*, Springer-Verlag Berlin Heidelberg 2014.

[6] A.L. Kholkin, N.A. Pertsev, and A.V. Goltsev, *Piezoelectricity and Crystal Symmetry*, A. Safari, E.K. Akdogan (eds.): Chap. 2, *Piezoelectric and Acoustic Materials for Transducer Applications*, Springer Science+Business Media, LLC 2008.

[7] A. Stapleton, T. Souliman, and T. Syed, *Biochemical Society: the Biochemist*, **40**, 28 (2018).

[8] A. Fleming, *Proc. R Soc. B Biol. Sci.*, **93**, 306 (1922).

[9] A. Stapleton, M. R. Noor, T. Soulimane, and S. A. M. Tofail, *Physiological Role of Piezoelectricity in Biological Building Blocks*, in *Electrically Active Materials for Medical Devices* (World Scientific, 2016).

[10] A. Stapleton, M.R. Noor, J. Sweeney, V. Casey, A. L. Kholkin, C. Silien, A. A. Gandhi, T. Soulimane, and S. A. M. Tofail, *Appl. Phys. Lett.*, **111**, 142902 (2017).

[11] Y. Liu *et al.*, *Proc. Natl Acad. Sci. USA*, **111**, E2780 (2014).

[12] E. Fukada, and I. Yasuda, *Jpn. J. Appl. Phys.*, **3**, 117 (1964).

[13] D. Dennig *et al.*, *ACS Biomater. Sci. Eng.*, **3** 929 (2017).

[14] S. Guarin *et al.*, *Nat. Mater.*, **17**, 180 (2018).

[15] E. Fukada, and I. Yasuda, *J. Phys. Soc. Jpn.*, **12** 1157 (1957).

[16] J. Chang, M. Dommer, C. Chang, and L. Lin, *Nano Energy*, **1**, 356 (2012).

[17] M. Pohanka, *Materials*, **11**, 448 (2018).

[18] S. Waqar, L. Wang, and S. John, *Piezoelectric energy harvesting from intelligent textiles*, T. Dias (ed): Chap. 9, in *Electronic Textiles:Smart Fabrics and Wearable Technology*, 2015 Elsevier.

[19] R.S. Dahiya, M. Valle, *Robotic Tactile Sensing: Technologies and System*, Springer 2013.

[20] https://www.energy-floors.com/.

[21] A. Moure *et al.*, *Energy Convers. Manag.*, **112**, 246 (2016).

[22] H. Yang, *et al.*, *Int. J. Pavement Res. and Technol.*, **11**, 168 (2018).

[23] B. M. Vul, and L. F. Vereshtschagin, *Dokl. Akad. Nauk SSSR*, **48**, 662 (1945).

[24] S. Robert, *Phys. Rev.*, **71**, 890 (1947).

[25] A. F. Devonshire, *Philos. Mag.*, **40**, 1040 (1949); **42**, 1065 (1951); *Adv. Phys.*, **3**, 85 (1954).

[26] D. Berlincourt, and H. Jaffe, *Phys. Rev.*, **111**, 143 (1958).

[27] G. Shirane and A. Takeda, *J. Phys. Soc. Jpn.*, **7**, 5 (1952).

[28] G. Shirane and K. Suzuki, *J. Phys. Soc. Jpn.*, **7**, 333 (1952).

[29] E. Sawaguchi, *J. Phys. Soc. Jpn.*, **8**, 615 (1953).

[30] B. Jaffe, R. S. Roth, and S. Marzullo, *J. Appl. Phys.*, **25**, 809 (1954).

[31] M. McQuarrie and F. W. Behnke, *J. Am. Ceram. Soc.*, **37**, 539 (1954).

[32] L. Luo, X. Zhao, and H. Luo, *Single crystal PZN-PT, PMN-PT, PSN-PT and PIN-PT-based piezoelectric materials*, K. Uchino (ed): Chap. 7, pp 239 − 286 in *Advanced Piezoelectric Materials: Science and Technology (First Edition)*, Woodhead Publishing 2010.

[33] E. Fukada and S. Takashita, *Jpn. J. Appl. Phys.*, **8**, 960 (1969).

[34] H. Kawai, *Jpn. J. Appl. Phys.*, **8**, 975 (1969).

[35] A. J. Lovinger, *Science*, **220**, 1115 (1983).

[36] L. Persano *et al.*, *Nat. Commun.*, **4**, 1633 (2013).

[37] E. Nilsson *et al.*, *Sens. Actuators A Phys.*, **201**, 477 (2013).

[38] A. Lund *et al.*, *npj Flexible Electronics* **2**, 9 (2018).

[39] T. Kitayama and S. Sugawara, *Proc. Study Comm. Electronic Circuit Components & Mater.*, CPM72-17 (1972).

[40] Directive 2002/95/EC, *Official Journal of the European Union*, L 37/19 (2003); Directive 2011/65/EU, *ibid.* L 174/88 (2011).

[41] https://echa.europa.eu

[42] T. Takenata, K. Maruyama, and K. Sakata, *Jpn. J. Appl. Phys.*, **30**, 2236 (1991).

[43] Y. Saito *et al.*, *Nature*, **432**, 84 (2004).

[44] W. Liu, and X. Ren, *Phys. Rev. Lett.*, **103**, 257602 (2009).

[45] T. Takenaka, *Lead-free piezo-ceramics*, K. Uchino (ed): Chap. 4, pp $130-170$ in *Advanced Piezoelectric Materials: Science and Technology (First Edition)*, Woodhead Publishing 2010.

[46] F. Cordero, *Materials*, **8** 8195 (2015).

[47] T. T. A. Lummen *et al.*, *Nat. Commun.*, **5**, 3172 (2014).

[48] R. Guo, L. E. Cross, S-E. Park, B. Noheda, D. E. Cox, and G. Shirane, *Phys. Rev. Lett.* **84**, 5423 (1999).

[49] B. Noheda, J. A. Gonzalo, L. E. Cross, R. Guo, S.-E. Park, D. E. Cox, and G. Shirane, *Appl. Phys. Lett.* **74**, 2059 (1999).

[50] B. Noheda, J. A. Gonzalo, L. E. Cross, R. Guo, S.-E. Park, D. E. Cox and G. Shirane, *Phys. Rev. B*, **61**, 8687 (2000).

[51] D. S. Keeble, F. Benabdallah, P. A. Thomas, M. Maglione, and J. Kreisel, *Appl. Phys. Lett.* **102**, 092903 (2013).

[52] H. Fu, and R. E. Cohen, *Nature*, **403**, 281 (2000).

[53] B. Nohesa and D. E. Cox, *Phase Transitions*, **97**, 5 (2006).

[54] M. Acosta, N. Novak. W. Jo, and J. Rdel, *Acta Mater.*, **80**, 48 (2014).

[55] M. Yuan *et al.*, *Adv. Mater.*, **26**, 7432 (2014).

[56] L. Cheng *et al.*, *Nano Energy*, **15**, 598 (2015).

[57] N. R. Alluri, B. Saravanakumar, and S.-J. Kim, *ACS Appl. Mater. Interfaces*, **7**, 9831 (2015).

[58] N. D. Scarisoreanu *et al.*, *ACS Appl. Mater. Interfaces*, **9**, 266 (2017).

[59] E. Bousquet, *First-principles study of ferroelectric oxide nanostructures*, PhD thesis, Université de Liège (2008).

[60] R. Resta and, D. Vanderbilt *Theory of Polarization: A Modern Approach*, K. Rabe, C. H. Ahn and J.-M. Triscone (Eds): Physics of Ferrelectrics, *Topics Appl. Physics*, **105**, 117 (2007).

[61] Ph. Ghosez: *Microscopic properties of ferroelectric oxides from first principles: Selected topics* (Troisieme Cycle de la Physique en Suisse Romande, Lausanne 2002) 145 pages URL: http://www.phythema.ulg.ac.be/Books/Cours/Ferro.Ghosez.pdf

[62] W. Setyawan, and S. Curtarolo, *Computational Materials Science*, **49**, 299 (2010).

[63] Goldschmidt, *V.M. Naturwissenschaften*, **14**, 477 (1926).

[64] M. W. Lufaso and P. M. and Woodward, *Acta Cryst.*, **B57**, 725 (2001).

[65] L. D. Landau and, E. M. Lifshitz, *Statistical Physics* (Mir, 1968).

[66] P. Chandra and, P. B. Littlewood, *A Landau Primer for Ferroelectrics*, K. Rabe, C. H. Ahn and J.-M. Triscone (Eds): Physics of Ferrelectrics, *Topics Appl. Physics*, **105**, 117 (2007).

[67] B. A. Strukov and A. P. Levanyuk, *Ferroelectric Phenomena in Crystals: Physical Foundations*, Springer-Verlag Berlin Heidelberg 1998.

[68] F. Li, L. Jin, Z. Hu, and S. Zhang, *Appl. Phys. Rev.*, **1**, 011103 (2014).

[69] A. P. Levanyuk and D. G. Sannikov, *Usp. Fiz. Nauk.*, **112**, 561 (1974).

[70] J. Varignon and Ph. Ghosez, *Phys. Rev. B*, **87**, 140403(R) (2013).

[71] E. Bousquet *et al.*, *Nature*, **452**, 732 (2008).

[72] J. Holakovský, *Phys. Status Solidi B*, **56**, 615 (1973).

[73] K. M. Rabe and J. D. Joannopoulos, *Phys. Rev. Lett.*, **59**, 570 (1987).

[74] R. D. King-Smith and D. Vanderbilt, *Phys. Rev. B*, **49**, 5828 (1994).

[75] W. Zhong, D. Vanderbilt and K. M. Rabe, *Phys. Rev. B*, **52**, 6301 (1995).

[76] C. Ederer and, N. A. Spaldin, *Phys. Rev. Lett.*, **95**, 257601 (2005).

[77] P. Hermet, M. Goffinet, J. Kreisel, and Ph. Ghosez, *Phys. Rev. B*, **75**, 220102 (2007).

[78] I. A. Kornev, S. Lisenkov, R. Haumont, B. Dkhil, and L. Bellaiche, *Phys. Rev. Lett.*, **99**, 227602 (2007).

[79] A. M. Glazer, *Acta Crystallogr. B*, **28**, 3384 (1972).

[80] C. J. Howard, and H. T. Stokes, *Acta Cryst.*, **B54**, 782 (1998).

[81] N. A. Benedek, C. J. Fennie, *J. Phys. Chem. C*, **117**, 13339 (2013).

[82] M. Posternak, R. Resta, and A. Baldereschi, *Phys. Rev. B*, **50**, 8911(R) (1994).

[83] A. García, and D. Vanderbilt, *Phys. Rev. B*, **54**, 3817 (1996).

[84] R. E. Cohen, *J. Phys. Chem. Solids* , **61**, 139 (2000).

[85] D. I. Bilc, and D. J. Singh, *Phys. Rev. Lett.*, **96**, 147602 (2006).

[86] S. Amisi *et al*, *Phys. Rev. B*, **85**, 064112 (2012).

[87] N. Miao *et al.*, *J. Phys.: Condens. Matter*, **26**, 035401 (2014).

[88] V. L. Ginzburg, *Zh. Eksp. Teor. Fiz.*, **19**, 36 (1949).

[89] W. Cochran, *Phys. Rev. Lett.*, **3**, 412 (1959).

[90] W. Cochran, *Adv. Phys.*, **9**, 387 (1960).

[91] *American Mineralogist*, **82**, 213 (1997).

[92] Ph. Ghosez and J. Junquera, *Handbook of Theoretical and Computational Nanotechnology*, (American Scientific Publishers, Stevenson Ranch, CA, 2006).

[93] K. M. Rabe and Ph. Ghosez, *First-Principles Studies of Ferroelectric Oxide*, K. Rabe, C. H. Ahn and J.-M. Triscone (Eds): Physics of Ferrelectrics, *Topics Appl. Physics*, **105**, 117 (2007).

[94] P. A. Fleury, J. F. Scott, and J. M. Worlock, *Phys. Rev. Lett.*, **21**, 16 (1968).

[95] G. Shirane, J. D. Axe, J. Harada, and J. P. Remeika *Phys. Rev. B*, **2**, 155 (1970).

[96] J. F. Scott, *Rev. Mod. Phys.*, **46**, 83 (1974).

[97] M. T. Dove, *Structure and Dynamics: An Atomic View of Materials*, Oxford Master Series in Condensed Matter Physics (Oxford University Press, 2002).

[98] K. F. Garrity, K. M. Rabe, and D. Vanderbilt, *Phys. Rev. Lett.*, **112**, 127601 (2014).

[99] Ph. Ghosez, J.-P. Michenaud and X. Gonze, *Phys. Rev. B*, **58**, 6224 (1998).

[100] W. Zhong, R.D. King-Smith and D. Vanderbilt, *Phys. Rev. Lett.*, **72**, 3618 (1994).

[101] Ph. Ghosez, X. Gonze and J.-P. Michenaud, *Ferroelectrics*, **194**, 39 (1997).

[102] Ph. Ghosez, E. Cockayne, U. V. Waghmare and K. M. Rabe, *Phys. Rev. B*, **60**, 836 (1999).

[103] L. Bellaiche, *Curr. Opin. Solid State Mater. Sci.*, **6**, 19 (2002).

[104] G. Sághi-Szabó, R. E. Cohen and, H. Krakauer, *Phys. Rev. Lett.*, **80**, 4321 (1998).

[105] K. M. Rabe, M. Dawber, C. Lichtensteiger, Ch. H. Ahnand, and J.-M. Triscone *Modern Physics of Ferroelectrics: Essential Background*, K. Rabe, C. H. Ahn and J.-M. Triscone (Eds): Physics of Ferrelectrics, *Topics Appl. Physics*, **105**, 117 (2007).

[106] M. Acosta, N. Khakpash, T. Someya, N. Novak, W. Jo, H. Nagata, G. A. Rossetti, and J. Rödel *Phys. Rev. B*, **91**, 104108 (2015).

[107] G. Grosso, and G. P. Parravicini, *Solid State Physics*, Elsevier.

[108] P. Hohenberg, and W. Kohn, *Phys. Rev.*, **136**, B 864 (1964).

[109] W. Kohn, L. Sham, *Phys. Rev.*, **140**, A 1133 (1965).

[110] E. P. Wigner, *Trans. Faraday Soc.*, **34**, 678 (1938).

[111] L. Hedin, and B. Lundqvist, *J. Phys. C*, **4**, 2064 (1971).

[112] S. H. Vosko, L. Wilk, and M. Nusair, *Can. J. Phys.*, **58**, 1200 (1980).

[113] J. P. Perdew, A. Zunger, *Phys. Rev. B*, **23**, 5048 (1981).

[114] D.C. Langreth, and M. J. Mehl, *Phys. Rev. Lett.*, **47**, 446 (1981).

[115] D.C. Langreth, and M. J. Mehl, *Phys. Rev. B*, **28**, 1809 (1983).

[116] M. C. Payne, M. P. Teter, D. C. Allan, T. A. Arias, and J. D. Joannopoulos, *Rev. Mod. Phys.*, **64**, 1045 (1992).

[117] A. K. Rajagopal, J. Callaway, *Phys. Rev. B*, **7**, 1912 (1973).

[118] O. Gunnarsson, B. I. Lundqvist, *Phys. Rev. B*, **13**, 4274 (1976)

[119] S. Baroni, S. De Gironcoli, and A. Dal Corso, *Rev. Mod. Phys.*, **73**, 515 (2001).

[120] J. P. Perdew, M. Levy, *Phys. Rev. Lett.*, **51**, 1884 (1983).

[121] J. P. Perdew, J. Chevary, S. Vosko, K. Jackson, M. Pederson, D. Singh, C. Fiolhais, *Phys. Rev. B*, **46**, 6671, (1992).

[122] J. P. Perdew, K. Burke, M. Ernzerhof, *Phys. Rev. Lett.*, **77**, 3865, 1996.

[123] J. P. Perdew, and K. Burke, *Int. J. Quant. Chem*, **57**, 309, 1996.

[124] J. P. Perdew, J. Chevary, S. Vosko, K. Jackson, M. Pederson, D. Singh, C. Fiolhais, *Phys. Rev. B*, **69**, 075102 (2004).

[125] D. R. Hamann, *Phys. Rev. Lett.*, **76**, 660 (1996).

[126] C. Filippi, D. J. Singh, C. Umrigar, *Phys. Rev. B*, **50**, 14947 (1994).

[127] J. P. Perdew, K. Burke, Y. Wang, *Phys. Rev. B*, **54**, 16533 (1996).

[128] D. C. Langreth, J. P. Perdew, *Phys. Rev. B*, **21**, 5469 (1980).

[129] J. P. Perdew, S. Kurth, A. Zupan, and P. Blaha, *Phys. Rev. Lett.*, **82**, 2544 (1999).

[130] J. Tao, J. P. Perdew, V. N. Staroverov, and G. E. Scuseria, *Phys. Rev. Lett.*, **91**, 146401 (2003).

[131] V. N. Staroverov, G. E. Scuseria, J. Tao and John P. Perdew, *Phys. Rev. B*, **48**, 4978 (1993).

[132] Z. Wu, R. E. Cohen and D. J. Singh, *Phys. Rev. B*, **70**, 104112 (2004).

[133] Z. Wu and R. E. Cohen, *Phys. Rev. B*, **73**, 235116 (2006).

[134] D. J. Chadi, and M. L. Cohen, *Phys. Rev. B*, **8**, 5747 (1973).

[135] H. J. Monkhorst, and J. D. Pack, *Phys. Rev. B*, **13**, 5188 (1976).

[136] R. A. Evarestov, and V. P. Smirnov, *Phys. Status Solidi*, **119**, 9 (1983).

[137] D. R. Hamann, *Phys. Rev. B*, **88**, 085117 (2013).

[138] L. Bellaiche and D. Vanderbilt, *Phys. Rev. B*, **61**, 7877 (2000).

[139] Ph. Ghosez, D. Desquesnes, X. Gonze, and K. M. Rabe, *AIP Conference Proceedings* **535**, 102 (2000).

[140] N. J. Ramer, and A. M. Rappe, *J. Phys. Chem. Solids* **61**, 317 (2000).

[141] S. Baroni, P. Giannozzi, and A. Testa, *Phys. Rev. Lett.* **58**, 1861 (1987).

[142] X. Gonze, and C. Lee, *Phys. Rev. B*, **55**, 10355 (1997).

[143] X. Gonze *Phys. Rev. B*, **55**, 10337 (1997).

[144] S. Baroni, P. Giannozzi, and A. Testa, *Phys. Rev. Lett.*, **59**, 2662, (1987).

[145] S. de Gironcoli, S. Baroni, and R. Resta, *Phys. Rev. Lett.*, **62**, 2853, (1989).

[146] S. de Gironcoli, P. Giannozzi, and S. Baroni, *Phys. Rev. Lett.*, **66**, 2116, (1991).

[147] P. Giannozzi, S. de Gironcoli, P. Pavone, and S. Baroni, *Phys. Rev. B*, **43**, 7231, (1991).

[148] X. Gonze, and J.-P. Vigneron, *Phys. Rev. B*, **39**, 13120, (1989); *Phys. Rev. B*, **44**, 3494, (1991).

[149] X. Gonze, *Phys. Rev. A*, **52**, 1086, (1995).

[150] X. Gonze, *Phys. Rev. A*, **52**, 1096, (1995).

[151] M. J. Verstraete, and Z. Zanolli, *Density Functional Perturbation Theory*, 45th IFF Spring School "Computing Solids: Models, *ab-initio* methods and supercomputing" (Forschungszentrum Jülich, 2014).

[152] X. Gonze *et al.*, *Phys. Rev. B*, **50** 13035 (1994).

[153] R. Resta, *Ferroelectrics*, **136**, 51 (1992).

[154] R. Resta, *Rev. Mod. Phys.*, **66**, 899 (1994).

[155] Ph. Ghosez, and X. Gonze, *J. Phys.: Condens. Matter*, **12**, 9179 (2000).

[156] X. Gonze, J.-M. Beuken, R. Caracas, F. Detraux, M. Fuchs, G.-M. Rignanese, L. Sindic, M. Verstraete, G. Zerah, F. Jollet, M. Torrent, A. Roy, M. Mikami, Ph. Ghosez, J.-Y. Raty, and D.C. Allan, *Computational Materials Science*, **25**, 478 (2002).

[157] X. Gonze, G.-M. Rignanese, M. Verstraete, J.-M. Beuken, Y. Pouillon, R. Caracas, F. Jollet, M. Torrent, G. Zerah, M. Mikami, Ph. Ghosez, M. Veithen, J.-Y. Raty, V. Olevano, F. Bruneval, L. Reining, R. Godby, G. Onida, D.R. Hamann, and D.C. Allan, *Z. Kristallogr.* **220**, 558 (2005).

[158] X. Gonze, B. Amadon, P.-M. Anglade, J.-M. Beuken, F. Bottin, P. Boulanger, F. Bruneval, D. Caliste, R. Caracas, M. Cote, T. Deutsch, L. Genovese, Ph. Ghosez, M. Giantomassi, S. Goedecker, D.R. Hamann, P. Hermet, F. Jollet, G. Jomard, S. Leroux, M. Mancini, S. Mazevet, M.J.T. Oliveira, G. Onida, Y. Pouillon, T. Rangel, G.-M. Rignanese, D. Sangalli, R. Shaltaf, M. Torrent, M.J. Verstraete, G. Zerah, and J.W. Zwanziger, *Computer Phys. Comm.* **180**, 2582 (2009).

[159] www.abinit.org

[160] R. C. Kell, and N. J. Hellicar, *Acta Acustica united with Acustica*, **6**, 235 (1956).

[161] K. Brajesh, M. Abebe, and R. Ranjan, *Phys. Rev. B*, **94**, 104108 (2016).

[162] J. W. Edwards, R. Speiser, and H. L. Johnston, *J. Am. Chem. Soc*, **73**, 2934 (1951).

[163] A. R. Akbarzadeh, I. Kornev, C. Malibert, L. Bellaiche, and J. M. Kiat, *Phys. Rev. B*, **72**, 205104 (2005).

[164] R. Ali, and M. Yashima, *J. Solid State Chem.*, **178**, 2867 (2005).

[165] R. W. G. Wyckoff, *Crystal Structures*, **2**, 390 (1964).

[166] W. Cochran, *Adv. Phys.*, **9**, 387 (1960).

[167] W. Zhong, D. Vanderbilt, and K. M. Rabe, *Phys. Rev. B*, **52**, 6301 (1995).

[168] Ph. Ghosez, X. Gonze, and J.-P. Michenaud, *Ferroelectrics*, **206**, 205 (1998).

[169] Y. Qi, S. Liu, I. Grinberg, and A. M. Rappe, *Phys. Rev. B*, **94**, 134308 (2016).

[170] G. Shirane, H. Danner, and R. Pepinsky, *Phys. Rev.*, **105**, 856 (1957).

[171] A. W. Hewat, *Ferrelectrics*, **6**, 215 (1974).

[172] G. H. Kwei, A. C. Lawson, S. J. L. Billinge, and S. W. Cheong, *J. Phys. Chem.* **97**, 2368 (1993).

[173] W. Zhong, and D. Vanderbilt, *Phys. Rev. Lett.*, **74**, 2587 (1995).

[174] B. J. Kennedy, C. J. Howard, and B. C. Chakoumakos, *J. Phys.: Condens. Matter*, **11**, 1479 (1993).

[175] Y. Wang, and R. C. Liebermann, *Phys. Chem. Minerals*, **20**, 147 (1993).

[176] Z. F. Hou, *Physica B*, **403**, 2624 (2008).

[177] P. Stoch, J. Szczerba, J. Lis, D. Madej, and Z. Pedzich, *J. Eur. Ceram. Soc*, **32**, 665 (2012).

[178] Y. Du, Z.P. Jin, and P. Y. Huang, *J. Am. Ceram. Soc*, **75**, 3040 (1992).

[179] L. Bellaiche, and J. Íñiguez, *Phys. Rev. B*, **88**, 014104 (2013).

[180] K. M. Rabe and U. V. Waghmare, *Phil. Trans. R. Soc. Lond. A*, **354**, 2897 (1996).

[181] C. Ederer and, N. A. Spaldin, *Phys. Rev. Lett.*, **95**, 257601 (2005).

[182] A. J. Hatt, N. A. Spaldin and, C. Ederer, *Phys. Rev. B*, **81**, 054109 (2010).

[183] X. Cheng, and M. Shen, *Mater. Res. Bull.*, **42**, 1662 (2007).

[184] D. Fu, and M. Itoh, arXiv:1503.00406 [cond-mat.mtrl-sci] (2015).

[185] V. D. Araújo, F. V. Motta, A. P. A. Marques, C. A. Paskocimas, M. R. D. Bomio, E. Longo, and J. A. Varela, *J. Mater. Sci.*, **49**, 2875 (2014).

[186] R. D. Shannon, *Acta Cryst.*, **A 32**, 751 (1976).

[187] R. E. Cohen, and H. Krakauer, *Phys. Rev. B*, **42**, 6416 (1990).

[188] Ph. Ghosez, X. Gonze, and J.-P. Michenaud, *Europhys. Lett.*, **33**, 713 (1996).

[189] E. Bousquet, and Ph. Ghosez, *Phys. Rev. B*, **74**, 180101 (2006).

[190] J. W. Bennett, I. Grinberg, and A. M. Rappe, *Chem. Mater.*, bf 20, 5134 (2008).

[191] R. D. Smith, and D. Vanderbilt, *Phys. Rev. B*, **47**, 1651 (1993).

[192] J. W. Bennett, I. Grinberg, and A. M. Rappe, *Chem. Mater.*, **20**, 5134 (2008)

[193] I. Levin, V. Krayzman, and J. C. Woicik, *Appl. Phys. Lett.*, **102**, 162906 (2013).

[194] I. B. Ouni, D. Chapron, H. Aroui and M. D. Fontana, *J. Appl. Phys.*, **121**, 114102 (2017).

[195] D. Fu, M. Itoh, S.-ya Koshihara, T. Kosugi, and S. Tsuneyuki, *Phys. Rev. Lett.*, **100**, 227601 (2008).

[196] T. Mitsui, and W. B. Westphal, *Phys. Rev.*, **124**, 1354 (1961).

[197] D. E. Khmel'nitskii and V. L. Shneerson, *Sov. Phys. Solid State*, **13**, 687 (1971).

[198] A. Cano and A. P. Levanyuk, *Phys. Rev. B*, **70**, 064104 (2004).

[199] J. Ravez, and A. Simon, *Eur. J. Solid State Inorg. Chem.*, **34**, 1199 (1997).

[200] J. Savez, C. Broustera, and A. Simon, *J. Mater. Chem.*, **9**, 1609 (1999).

[201] A. Simon, J. Ravez, and M. Maglione, *J. Phys.: Condens. Matter*, **16**, 936 (2004).

[202] C. Laulhé, F. Hippert, J. Kreisel, M. Maglione, A. Simon, J. L. Hazemann, and V. Nassif , *Phys. Rev. B*, **74**, 014106 (2006).

[203] V. S. Puli, D. K. Pradhan, B. C. Riggs, D. B. Chrisey, and R. S. Katiyar, *Integrated Ferrolectrics*, **157**, 139 (2014).

[204] M. Dawber, C. Lichtensteiger, M. Cantoni, M. Veithen, Ph. Ghosez,K. Johnston, K. M. Rabe,and J.-M. Triscone, *Phys. Rev. Lett.*, **95**, 177601 (2005).

[205] M. Dawber, N. Stucki, C. Lichtensteiger, S. Gariglio, Ph. Ghosez, and J.-M. Triscone, *Adv. Mater.*, **19**, 4153 (2007).

[206] E. Bousquet, J. Junquera, and Ph. Ghosez, *Phys. Rev. B*, **82**, 045426 (2010).

[207] N. Sai, K. Rabe, and D. Vanderbilt, *Phys. Rev. B*, **66**, 104108 (2002).

[208] T. Maiti, R. Guo, and A.S. Bhalla, *J. Am. Ceram. Soc.*, **91**, 1769 (2008).

[209] J. Kreisel, P. Bouvier, M. Maglione, B. Dkhil, and A. Simon, *Phys. Rev. B*, **69**, 092104 (2004).

[210] C. Laulhé, F. Hippert, J. Kreisel, A. Pasturel, A. Simon, J.-L. Hazemann, R. Bellissent, and G.J. Cuello, *Phase Transition*, **84**, 438 (2011).

[211] N. K. Karan *et al.*, *J. Raman Spectrosc*, **40**, 370 (2009).

[212] A. R. Akbarzadeh, S. Prosandeev, Eric J. Walter, A. Al-Barakaty, and L. Bellaiche, *Phys. Rev. Lett.*, **108**, 257601 (2012).

[213] Y. Nahas, A. Akbarzadeh, S. Prokhorenko, S. Prosandeev, R. Walter, I. Kornev, J. Íñiguez, and L. Bellaiche, *Nat. Commun.*, **8**, 15944 (2017).

[214] C. Chemarin, N. Rosman, T. Pagnier, and G. Lucazeau, *Journal of Solid State Chemistry*, **149**, 298 (2000).

[215] Md Al Helal, T. Mori, and S. Kojima, *Ferroelectrics*, **499**, 107 (2016).

[216] R. S. Mulliken, *J. Chem. Phys.*, **23**, 1997 (1955).

[217] K.Momma, and F. Izumi, *J. Appl. Crystallogr.*, **44**, 1272 (2011).

[218] ISOTROPY Software Suite, iso.byu.edu., H. T. Stokes, D. M. Hatch, and Branton J. Campbell, *FINDSYM: Program for Identifying the Space Group Symmetry of a Crystal*, *J. Appl. Cryst.*, **38**, 237 (2005).

[219] K.Momma, and F. Izumi, *J. Appl. Crystallogr.*, **44**, 1272 (2011).

[220] Kroumova *et. al.*, *Phase Transitions*, **76**, 155 (2003).

[221] ISOTROPY Software Suite, iso.byu.edu., H. T. Stokes, D. M. Hatch, and Branton J. Campbell, *SMODES:Find the displacement modes in a crystal which brings the dynamical matrix to block-diagonal form, with the smallest possible blocks.*